THE ASTROPHYSICAL JOURNAL, 849:106 (28pp), 2017 November 10 https://doi.org/10.3847/1538-4357/aa9229

An Ultraviolet Survey of Low-redshift Partial Lyman-limit Systems with the *HST* Cosmic Origins Spectrograph

J. Michael Shull[1], Charles W. Danforth[1], Evan M. Tilton[1], Joshua Moloney[1], and Matthew L. Stevans[2]
[1] CASA, Department of Astrophysical & Planetary Sciences, University of Colorado, Boulder, CO 80309, USA; michael.shull@colorado.edu
[2] Dept. of Astronomy, University of Texas at Austin, Austin, TX 78712, USA; danforth@colorado.edu
Received 2016 July 19; revised 2017 September 18; accepted 2017 October 5; published 2017 November 7

Abstract

We present an ultraviolet spectroscopic survey of strong H I absorbers in the intergalactic medium, probing their evolution over the last 6–7 Gyr at redshifts $0.24 \leqslant z \leqslant 0.84$. We measure column densities $N_{\rm H\,I}$ (cm^{-2}) from the pattern of Lyman-series absorption lines and flux decrement at the Lyman limit (LL) when available. We analyzed 220 H I absorbers in ultraviolet spectra of 102 active galactic nuclei (AGNs) taken by the Cosmic Origins Spectrograph on board the *Hubble Space Telescope* with G130M/G160M gratings (1134–1795 Å). For 158 absorbers with log $N_{\rm H\,I} \geqslant 15$, the mean frequency is $d\mathcal{N}/dz = 4.95 \pm 0.39$ over path length $\Delta z = 31.94$ ($0.24 \leqslant z \leqslant 0.84$). We identify eight Lyman limit systems (LLS, log $N_{\rm H\,I} \geqslant 17.2$) and 54 partial systems (pLLS) with $16.0 \leqslant \log N_{\rm H\,I} < 17.2$. Toward 159 AGNs in the range $0.01 < z_{\rm abs} < 0.84$ with $\Delta z \approx 48$, we find four damped Lyα absorbers (DLA) with $(d\mathcal{N}/dz)_{\rm DLA} = 0.083^{+0.066}_{-0.040}$ at $\langle z \rangle = 0.18$. The mean LLS frequency in $z = 0.24$–0.48 is $(d\mathcal{N}/dz)_{\rm LLS} = 0.36^{+0.20}_{-0.13}$ fitted to $N(z) = (0.25^{+0.13}_{-0.09})(1+z)^{1.14}$. For 54 pLLSs, we find $(d\mathcal{N}/dz)_{\rm pLLS} = 1.69 \pm 0.23$ at $\langle z \rangle = 0.39$, a frequency consistent with gaseous halo sizes $R \approx 100\ h^{-1}$ kpc for (0.3–$3L^*$) galaxies. A maximum-likelihood analysis yields a distribution $f(N, z) = C_0 N^{-\beta}(1+z)^{\gamma}$ with $\beta = 1.48 \pm 0.05$ and $\gamma = 1.14^{+0.88}_{-0.89}$ for $15 \leqslant \log N_{\rm H\,I} \leqslant 17.5$. The far-UV opacity gradient is $d\tau_{\rm eff}/dz \approx (0.444)(1+z)^{1.14}$ over the range $15 \leqslant \log N_{\rm H\,I} \leqslant 17$, implying mean LyC optical depth $\tau_{\rm eff} \approx 0.3$–$0.5$ toward sources at $z = 1$–2.

Key words: cosmological parameters – cosmology: observations – intergalactic medium – quasars: absorption lines – ultraviolet: galaxies

1. Introduction

Over the past decade, astronomers have uncovered large reservoirs of gas in the outer portions of galaxy halos (Tumlinson et al. 2011a, 2013; Stocke et al. 2013, 2014) and in the intergalactic medium or IGM (Penton et al. 2004; Shull et al. 2012a), far from the gravitational influence of individual galaxies. These gaseous structures are detected by absorption-line spectra of quasars and other active galactic nuclei (AGNs) using resonance lines of neutral hydrogen (H I) and metal ions (e.g., C IV, O VI, Si III, C II) in the rest-frame far-ultraviolet. Shortward of the Lyα emission line at 1215.67 Å, numerous weak H I absorption lines blanket the AGN continuum in the "Lyα forest" with column densities that we have been able to measure reliably through *Hubble Space Telescope* (*HST*)/COS absorption-line spectra over the range $12.5 \leqslant \log N_{\rm H\,I}$ (cm^{-2}) $\leqslant 15.0$ (Danforth et al. 2016). Over the range $15 < \log N_{\rm H\,I} \lesssim 17$, the Lyman lines are highly saturated, and column densities are difficult to measure from Lyman series absorption alone. When log $N_{\rm H\,I} \geqslant 17.2$, photoelectric absorption in the Lyman continuum (LyC) produces an optical depth $\tau_{\rm LL} \geqslant 1$ at the Lyman limit (LL) at $\lambda_{\rm LL} = 911.753$ Å. These redshifted absorbers are called Lyman-limit systems (LLSs), while those with slightly lower column densities are termed "partial Lyman-limit systems" (pLLSs). In this paper, we use the term Lyman limit in reference to the redshifted wavelength (912 Å rest frame) and the types of absorbers (pLLS or LLS). The term Lyman decrement refers to the drop in transmitted flux at the LL, which is used to define the continuum optical depth ($\tau_{\rm LL}$).

Spanning a loosely defined range ($16 < \log N_{\rm H\,I} < 17.2$), the pLLSs are commonly associated with galaxies (Sargent et al. 1989; Steidel 1990; Simcoe et al. 2006) and their gaseous halos, now more fashionably called the circumgalactic medium (CGM). Although previous *HST* surveys (Storrie-Lombardi et al. 1994; Stengler-Larrea et al. 1995; Ribaudo et al. 2011a) focused primarily on true LLSs, we note that two recent surveys of "Lyman limit systems" (Ribaudo et al. 2011a; Lehner et al. 2013) also included many partial LLSs in their tables. The LLSs and pLLSs dominate the continuum opacity of the IGM (Shull et al. 1999; Haardt & Madau 2012; O'Meara et al. 2013) and probe the metallicities in the environment around galaxies (Ribaudo et al. 2011b; Tripp et al. 2011; Fox et al. 2013; Lehner et al. 2013). Even rarer are the damped Lyα (DLA) absorbers (Wolfe et al. 2005; Meiring et al. 2011; Turnshek et al. 2015), whose column densities, $N_{\rm H\,I} \geqslant 2 \times 10^{20}$ cm^{-2}, are sufficient to produce strong Lorentzian wings in their absorption profiles. These H I lines provide the dominant technique for measuring the baryon content of the IGM (Shull et al. 2012a), and the LLSs and pLLSs are a benchmark for determining the metallicity of the CGM (Tripp et al. 2011). Strong H I absorbers have been linked (Simcoe et al. 2006; Lehner et al. 2009; Ribaudo et al. 2011b) to the extended regions of galaxies. The semantic question of "where galaxies end" (Shull 2014) depends on their gravitational influence as well as dynamical effects of gaseous outflow and infall from the cosmic web (Tripp et al. 2011).

In our recent survey (Danforth et al. 2016) of low-redshift Lyα absorbers with the Cosmic Origins Spectrograph (COS) on the *HST*, we fitted the column densities to a power-law differential distribution, $f(N_{\rm H\,I}) \propto N_{\rm H\,I}^{-\beta}$, with $\beta = 1.65 \pm 0.02$ over the range $12.5 \leqslant \log N_{\rm H\,I} \leqslant 15.0$. Column densities determined from strong Lyα lines are uncertain owing to line saturation at log $N_{\rm H\,I} \geqslant 14$ for typical Doppler parameters $b \approx 20$–35 km s^{-1}. The distribution is also poorly constrained at log $N_{\rm H\,I} > 15$ because strong Lyα absorbers are rare. Some progress in defining their column densities has been made with

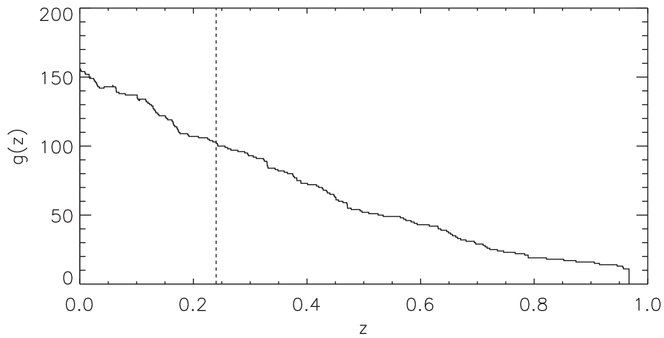

Figure 1. Distribution in redshift, $g(z)$, showing the number of AGNs that contribute a path length capable of detecting the redshifted LL of H I in the range $z = 0.003$–0.96. We consider only absorbers at $z \geqslant 0.24$ (dashed line) whose LL is redshifted into the COS/G130M band ($\lambda > 1130$ Å). These 102 AGN sight lines allow us to use the LL flux decrement, when available, and the curve of growth for Lyman absorption lines to determine H I column densities and assess systematic errors.

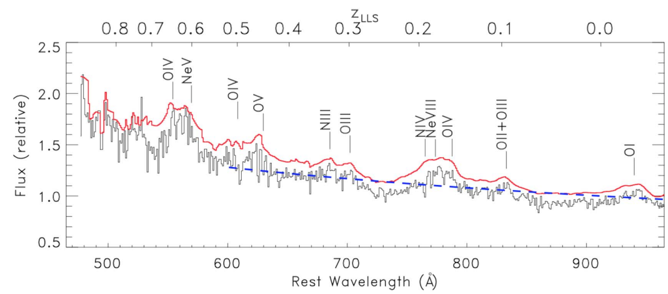

Figure 2. AGN composite spectrum based on Stevans et al. (2014) and annotated with prominent EUV broad emission lines of metal ions (O, N, Ne). The red spectrum shows the spline fit to the AGN flux passing above Lyα absorption lines (black). The AGN emission lines must be identified and fitted before placing the underlying EUV continuum (blue dotted line). Measuring the LL optical depth of absorbers requires careful attention to the continuum on either side of the LL. The true continuum can be contaminated by broad emission lines such as the Ne VIII λ 770, 780 doublet, O IV λ 788, and the 685 Å and 702 Å lines of N III and O III. Shorter-wavelength EUV lines of O IV, O V, and Ne V can affect the continuum around absorbers at $z_{\rm LLS} = 0.45$–0.70.

access to higher Lyman lines (Lyβ, Lyγ, Lyδ) from the *FUSE* satellite (Shull et al. 2000) and *HST* (Danforth & Shull 2008; Danforth et al. 2016). The higher Lyman lines become available to COS at modest redshifts ($z \geqslant 0.107$ for Lyβ, $z \geqslant 0.167$ for Lyγ), and they yield more accurate measurements of the curve of growth (CoG). The LL shifts into the COS/G130M window at $z_{\rm abs} \geqslant 0.24$. At $\log N_{\rm H\,I} \gtrsim 16.2$, in data with good signal-to-noise ratio (S/N $\gtrsim$ 10), we can use the flux decrement at the Lyman edge to confirm and supplement the CoG solutions.

In this paper, we explore the pLLS/LLS distribution in $N_{\rm H\,I}$ and redshift, employing a "Lyman comb" technique to find strong H I absorbers in the range $z_{\rm abs} = 0.24$–0.95 from their pattern of Lyman-series absorption lines and Lyman edge. An accurate determination of the Ly decrement depends on a reliable continuum placement longward and shortward of the LL at observed wavelength $\lambda_{\rm obs} = (911.753\ \text{Å})(1 + z_{\rm abs})$. We use high-S/N spectra of 102 AGNs at $z_{\rm AGN} \geqslant 0.24$ with the COS G130M/160M gratings. Figure 1 shows the redshift coverage of our survey, plotting the number of AGN sight lines sensitive to the LL (at the 912 Å rest frame). Our survey has much higher spectral resolution ($R \approx 17{,}000$) than earlier surveys with the low-resolution ($R \approx 1000$–1300) gratings on *HST*/FOS and *HST*/STIS. In well-exposed spectra with S/N $\gtrsim$ 10, we are able to resolve velocity components $\Delta v = 40$–400 km s^{-1} within absorbers and construct multicomponent CoGs when needed. For absorbers with $\log N_{\rm H\,I} > 16.2$, the continuum optical depth at the LL is usually detectable by *HST*/COS with optical depth $\tau_{\rm LL} = (6.304 \times 10^{-18}\ {\rm cm}^2)\ \ N_{\rm H\,I} > 0.1$. By combining the Lyman decrement with CoG fitting, we can confirm the H I column density and its range of uncertainty.

The continuum can be influenced by AGN emission lines in the UV and EUV, many of which are broad and blended features that produce bumps and undulations in the underlying power-law continuum. Fortunately, we have a good template for the location of these emission features (Figure 2) obtained from the composite rest frame UV/EUV spectrum of AGNs (Shull et al. 2012b; Stevans et al. 2014). We refer the reader to our papers on AGN composite spectra (Shull et al. 2012a, 2012b; Stevans et al. 2014), which describe our choice of line-free windows. Typical errors in continuum choice typically result in ± 0.02 errors in $\log N_{\rm H\,I}$. In the rest-frame far-UV, the most prominent emission lines are the O VI doublet (1032 and 1038 Å), C III (977 Å), and a blend of O I features (930–950 Å). The dominant emission lines in the rest-frame EUV (550 Å to 912 Å) are lines of O II and O III (833 Å and 834 Å), a broad complex (760–800 Å) consisting of the Ne VIII doublet (770 Å and 780 Å) and O IV 788 Å, the 700 Å blend of O III (702 Å) and N III (686 Å), and strong emission lines of O IV (608 Å, 554 Å) and O V (630 Å). A full list of EUV lines in the AGN composite spectrum is provided in Table 4 of Shull et al. (2012b).

The sample used in this survey began with 159 AGN targets chosen because their UV brightness allowed them to be observed by *HST*/COS with both the G130M and G160M gratings. Of these 159 AGNs, 102 had redshifts $z_{\rm AGN} \geqslant 0.24$, sufficient to shift the LL and higher Lyman-series lines into the G130M window. This sample includes many AGNs previously observed by the *International Ultraviolet Explorer* (*IUE*) and *HST* spectrographs. Many were used by the COS-GTO team (Danforth et al. 2016) and COS-Halos project (Tumlinson et al. 2013) for the purpose of studying the low-redshift IGM and galactic halo gas. Stevans et al. (2014) used 159 AGNs with redshifts $0.001 < z_{\rm AGN} \leqslant 1.476$ to produce a COS composite spectrum of AGNs in their rest-frame UV and EUV. The AGNs in the COS-Halos program were selected to avoid strong Mg II absorbers at $z > 0.4$, which would bias the survey against LLSs. Because our survey of LLSs and pLLSs used only AGNs with $z_{\rm abs} \geqslant 0.24$, it excludes nearby Seyfert galaxies whose sight lines might be biased against LLSs. Further discussion of potential sample biases for LLSs and DLAs is given in Section 3.3 and in Ribaudo et al. (2011a) and Neeleman et al. (2016).

Spectra taken with the COS G130M/G160M gratings (Green et al. 2012) provide moderate spectral resolution ($R = \lambda/\Delta\lambda \approx 17{,}000$), allowing us to resolve individual Lyman-series absorbers and fit the underlying AGN continuum. With the combined coverage from the G130M grating (1134 Å–1460 Å) and G160M grating (1390 Å–1795 Å), we can identify LLSs and pLLSs out to $z_{\rm abs} \approx 0.95$, using a template of Lyman-series absorption lines at the same redshift. Even at $\log N_{\rm H\,I} < 16.2$, when the LyC optical depth is weak ($\tau_{\rm LL} < 0.1$), we are able to identify the Lyman line pattern down to $\log N_{\rm H\,I} \approx 14.5$ in well-exposed spectra (S/N $\gtrsim$ 10). Figure 3 shows three AGN sight lines with H I absorbers in the range $\log N_{\rm H\,I} = 15.0$–15.25, found through higher Lyman-series absorption lines (Lyγ through Ly8). In Figure 4, we demonstrate the effectiveness of

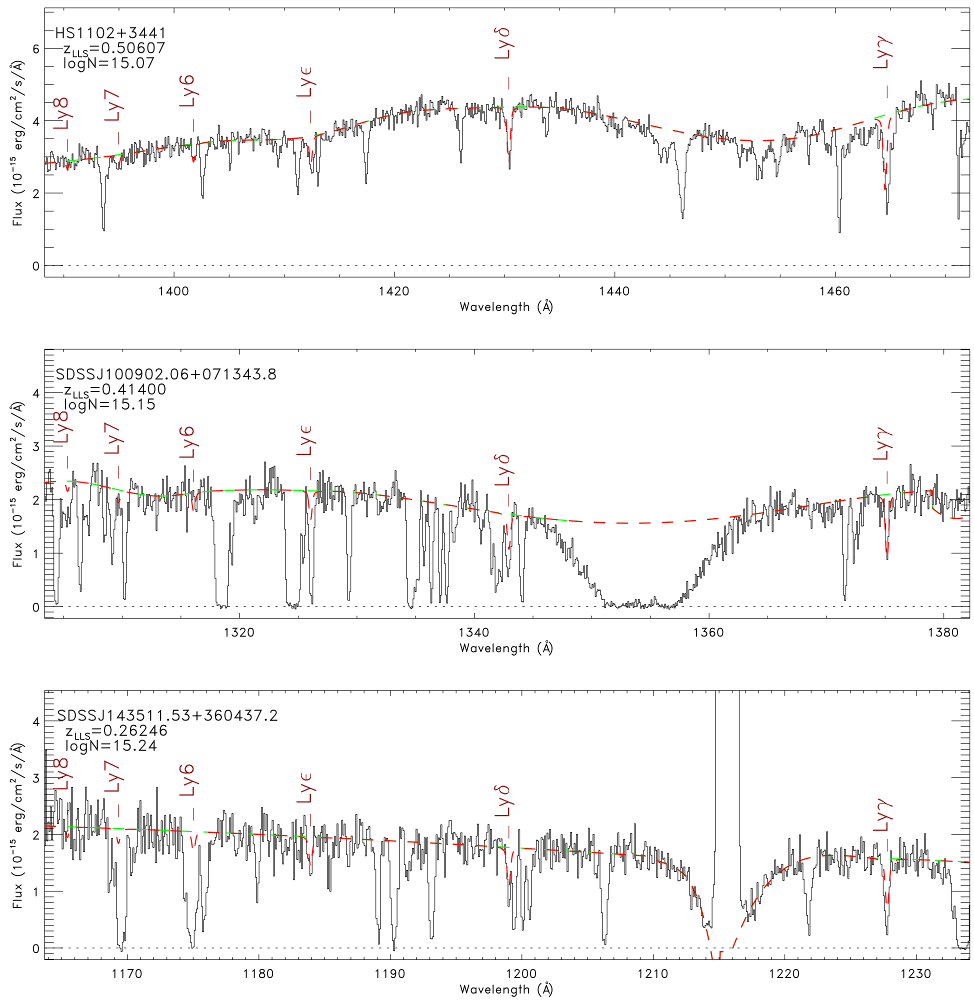

Figure 3. Three examples of COS/G130M detections of H I absorbers with log $N_{\rm H\,I} = 15.07 \pm 0.02$ (at $z = 0.5061$ toward HS 1102+3441), log $N_{\rm H\,I} = 15.15 \pm 0.02$ (at $z = 0.4140$ toward J1009+0713), and log $N_{\rm H\,I} = 15.24 \pm 0.02$ (at $z = 0.2625$ toward J1435+3604). Not shown are detections in Lyβ in all three systems and in Lyα for the bottom two systems, and Lyα shifts beyond the G160M window at $z > 0.47$. The panels show detections in the higher Lyman-series lines (Lyγ, Lyδ, Lyϵ, etc.). The middle panel includes a strong DLA at $z_a = 0.114$ (log $N_{\rm H\,I} = 20.68 \pm 0.10$) toward J1009+0713.

using the Lyman line pattern, compared to the injection of weak "mock absorbers" 300 km s^{-1} to the red of the actual absorber. This confirms our ability to detect systems below 50 mÅ equivalent width in data with S/N $\gtrsim$ 10.

Over the redshift range of H I absorbers in our full sample, $0.237 \leqslant z_{\rm abs} \leqslant 0.928$, we surveyed total absorption path length $\Delta z_{\rm eff} = 31.94$ and identified 211 absorbers: eight were LLSs with log $N_{\rm H\,I} \geqslant 17.2$, 54 were pLLSs in the range $16.0 <$ log $N_{\rm H\,I} < 17.2$, and the remainder lay in the range $14.0 < \log_{\rm H\,I} < 16.0$. Our COS survey contains the largest number of low-z LLSs and pLLSs to date, a distribution that we compare to absorbers in the *HST*/FOS Key Project surveys of LLSs at $0.4 < z < 1.4$ (Storrie-Lombardi et al. 1994; Stengler-Larrea et al. 1995) and the FOS/STIS survey of LLSs at $z < 2.6$ (Ribaudo et al. 2011a).

In Sections 2 and 3, we describe the data set of LLS and pLLS absorbers and our determination of their distribution, $f(N, z)$, in column density and redshift. We find a line frequency $d\mathcal{N}/dz = 4.95 \pm 0.39$ for $15.0 <$ log $N_{\rm H\,I} < 18.5$ averaged over $0.24 < z < 0.84$. We quantify the pLLS distribution in H I column density and redshift through maximum-likelihood fitting to the form $f(N, z) = C_0 \; N^{-\beta} \; (1 + z)^{\gamma}$, with best-fit parameters $\beta = 1.48 \pm 0.05$ and $\gamma = 1.14^{+0.88}_{-0.89}$. Although the evolutionary index $\gamma \approx 1.1$ is uncertain, owing to the limited redshift coverage and statistics, it is consistent with cosmological expectations for a population of nonevolving pLLS absorbers with constant space density and absorption cross section. By integrating the distribution of absorbers, $f(N_{\rm H\,I}, z)$, over column density, we compute the redshift gradient in LyC opacity, $d\tau_{\rm eff}/dz$, for absorbers in the range $12.5 \leqslant$ log $N_{\rm H\,I} \leqslant 17.2$. We estimate a far-UV (1130 Å) continuum opacity, $\tau_{\rm eff} \approx 0.4$–$0.5$, toward AGNs at $z \approx 1.5$–2.0 and discuss the possible effects on AGN source selection and their rest-frame EUV spectra. In Section 4, we summarize our results and their implications for IGM photoelectric opacity in the UV, QSO UV survey selection, and the spatial association of pLLSs with galaxy halos. Appendix A gives narratives of our analysis of 73 strong H I absorbers, 23 of which were studied in previous surveys. Appendix B describes our statistical analysis and the maximum-likelihood approach to obtaining distribution parameters.

2. Survey Techniques

Our survey of strong H I absorbers comes as a natural by-product of the UV composite spectra of AGNs constructed from moderate-resolution *HST*/COS data (Stevans et al. 2014). To find the underlying AGN continuum, we used G130M/G160M spectra to identify the numerous Lyα forest lines, as well as the

Table 1
Detectability Ranges for H I Lyman Absorption[a]

Feature	λ_0 (Å)	f	log $N_{\rm H\,I}$ $N_{\rm H\,I}$ ($\rm cm^{-2}$)	($z_{\rm min} - z_{\rm max}$) (G130M)	($z_{\rm min} - z_{\rm max}$) (G160M)
Lyα	1215.67	0.4164	12.96	0.002–0.200	0.152–0.477
Lyβ	1025.72	0.07912	13.83	0.107–0.422	0.365–0.750
Lyγ	972.54	0.02900	14.31	0.167–0.500	0.440–0.846
Lyδ	949.74	0.01394	14.65	0.195–0.536	0.474–0.890
Lyϵ	937.80	0.007804	14.92	0.210–0.556	0.493–0.914
Lyζ	930.75	0.004816	15.13	0.219–0.568	0.504–0.929
Lyη	926.23	0.003813	15.32	0.225–0.575	0.512–0.938
Lyθ	923.15	0.002216	15.48	0.229–0.581	0.517–0.944
LL	911.75	⋯	16.20	0.245–0.600	0.536–0.969

Note.
[a] Detectability ranges in redshift ($z_{\rm min}$ and $z_{\rm max}$) for the first eight Lyman lines (and Lyman limit) of H I. Columns 2 and 3 show the absorption oscillator strengths (f) and wavelengths (λ). Column 3 gives the H I column density detectable in Lyman-series absorption at 50 mÅ equivalent width, $N_{\rm H\,I} = (5.65 \times 10^{18}\ \rm cm^{-2})\ [f\lambda(Å)]^{-2}$, or in a 10% flux decrement at the Lyman edge. The last two columns show redshift coverage for *HST*/COS observations in gratings G130M (1134–1459 Å) and G160M (1400–1795 Å). Because we usually detect an absorber pattern from Lyα through Lyϵ, our survey should be complete for log $N_{\rm H\,I} \geqslant 15$. However, most LL decrements would be undetected at log $N_{\rm H\,I} < 16.2$.

less frequent but stronger (LLS and pLLS) absorbers. We did *not* consider absorbers associated with the host galaxy of the AGN. Owing to the high resolution of COS, we are able to distinguish individual absorption lines and resolve the true continuum level between them (Figures 3 and 4). As discussed in our AGN composite paper (Stevans et al. 2014), we corrected the AGN continuum for H I photoelectric absorption by pLLS and LLS absorbers. These corrections are important for establishing the underlying continuum longward and shortward of the H I absorption features. The LyC optical depth is related to H I column density by $\tau_\lambda \approx (6.304 \times 10^{-18}\ \rm cm^2)\ (\lambda/\lambda_{LL})^3 N_{\rm H\,I}$ for $\lambda \leqslant \lambda_{\rm LL}$. After determining $N_{\rm H\,I}$ from the flux decrement, we multiply the observed flux shortward of the LL by $\exp(\tau_\lambda)$ to restore the true AGN continuum.

The LLS and pLLS absorption systems are identified by a "Lyman comb" technique (Stevans et al. 2014) in which we search for a pattern of lines in the H I Lyman series together with the corresponding Lyman decrement when detectable. Table 1 lists the wavelengths, redshift bands, and column densities for which the first eight Lyman lines and decrement are easily detectable (greater than 50 mÅ equivalent width). To implement the method, we inspect the spectra for flux decrements at the LL, employing a computer script that scans for correlated down-pixels at the locations of higher-order Lyman lines of strong absorbers. When a system is confirmed, we measure the equivalent widths of up to the first 12 Lyman lines and fit them to a CoG to determine the column density and Doppler parameter (b in $\rm km\ s^{-1}$). Our technique depends primarily on identifying the pattern of Lyman lines and less on detecting the Lyman decrement. For the standard wavelength coverage in the COS/G130M grating (1134–1459 Å), the LL becomes detectable[3] at $z_{\rm LL} > 0.244$ and shifts out of the G130M band at $z_{\rm LL} > 0.60$. By including wavelength coverage with the G160M grating (1400–1795 Å), we can observe the far-UV range with access to the LL out to $z_{\rm LL} \approx 0.95$ and to various Lyman lines (Lyα–Lyζ) over the redshift ranges shown in Table 1. Figure 3 illustrates our method for the higher Lyman lines of three H I absorbers with log $N_{\rm H\,I} = 15.07$–15.24 at redshifts $z_{\rm abs} = 0.2625$, 0.4140, and 0.5061. All three systems were easily detected in Lyβ, and two of them have Lyα (for the absorber at $z = 0.5061$, Lyα has shifted beyond the G160M window). From the expected detection limits (Table 1) in COS spectra like those shown in Figure 3, our survey is able to identify strong absorbers down to log $N_{\rm H\,I} \approx 15$. In some AGN sight lines with low S/N (∼5), particularly those at redshifts ($z > 0.75$) where we lose Lyβ, we may miss some absorbers at log $N_{\rm H\,I} = 15.0$–15.5.

We began with the 221 strong absorption systems identified in the 159 AGN sight lines studied by Stevans et al. (2014). Because the LL shifts into the G130M band at $z \geqslant 0.24$, we only searched for strong absorbers toward those 102 quasars with redshifts $z_{\rm AGN} \geqslant 0.24$. For our statistical sample, we dropped a weak absorber at low column density (log $N_{\rm H\,I} = 13.5$). One LLS had a redshift ($z = 0.2374$) just below our cutoff at $z = 0.24$. We carefully reanalyzed all systems with log $N_{\rm H\,I} \geqslant 15.75$, combining a multicomponent CoG with measurements of the Ly decrement, when detectable. To derive $\tau_{\rm LL}$, we examined the AGN spectrum for broad emission-line contamination of the continuum on either side of the LL. In our reanalysis, we found an additional strong absorber omitted in Stevans et al. (2014), a DLA at $z_{\rm abs} = 0.3221$. Over redshifts $0.237 \leqslant z_{\rm abs} \leqslant 0.928$, we found eight true LLSs (log $N_{\rm H\,I} \geqslant 17.2$), one DLA (log $N_{\rm H\,I} = 20.34 \pm 0.12$), and 54 pLLSs ($16.0 \leqslant$ log $N_{\rm H\,I} < 17.2$). Including the lower-redshift portions of the spectrum ($z < 0.24$), we found a total of four DLAs toward all 159 surveyed AGNs, at redshifts $z_{\rm DLA} = 0.0963$, 0.1140, 0.185, and 0.3211. Appendix A presents a narrative discussion of 73 systems with log $N_{\rm H\,I} \geqslant 15.75$, many of which exhibit multiple velocity components separated by $\Delta v \approx 40$–$400\ \rm km\ s^{-1}$.

2.1. Measuring $N_{H\,I}$ from Lyman Lines and Lyman Edge

In an *HST*/COS survey of H I column densities in the low-redshift IGM along 82 AGN sight lines, Danforth et al. (2016) found 2577 distinct H I absorption systems, some of them single-line (Lyα) systems. For statistical analysis, they defined a "uniform sample" of 2256 systems in which $N_{\rm H\,I}$ was found by multiline CoG analysis, using either (Lyα + Lyβ) or (Lyβ + Lyγ) at a minimum for log $N_{\rm H\,I} \geqslant 13.5$, and Ly$\alpha$ alone for well-measured weaker lines. Of these 2256 absorbers, 65 had column densities $N_{\rm H\,I} \geqslant 10^{15}\ \rm cm^{-2}$. These column densities were determined by a traditional CoG, which works best for absorption lines that are unsaturated or mildly saturated. At $N_{\rm H\,I} < 10^{13.5}\ \rm cm^{-2}$, IGM surveys typically rely on Lyα absorbers, since Lyβ is too weak to detect at typical COS sensitivity (15–20 mÅ equivalent widths). When higher Lyman lines become available at higher z and greater $N_{\rm H\,I}$, the CoG yields reliable parameters (N, b). Once the Lyman lines become strongly saturated, with equivalent widths on the "flat portion" of the CoG, the inferred column densities are more uncertain. The onset of saturation is gauged by the line-center optical depth, $\tau_0 = (\pi e^2/m_e c)\ (N f \lambda/\pi^{1/2} b)$, where $b = (25\ \rm km\ s^{-1})\ b_{25}$ is a typical Doppler parameter. For the first four Lyman

[3] In some cases, the G130M spectra extend down to 1130 Å, allowing detection of the LL at $z \geqslant 0.24$. Because our Lyman-comb method relies on finding pLLSs through a pattern of Lyman lines, we could also detect Lyman lines from pLLSs at lower redshifts: $z > 0.107$ for Lyβ, $z > 0.167$ for Lyγ, and $z > 0.195$ for Lyδ. See Figure 3 for examples. In this survey we only report on systems at $z \geqslant 0.24$.

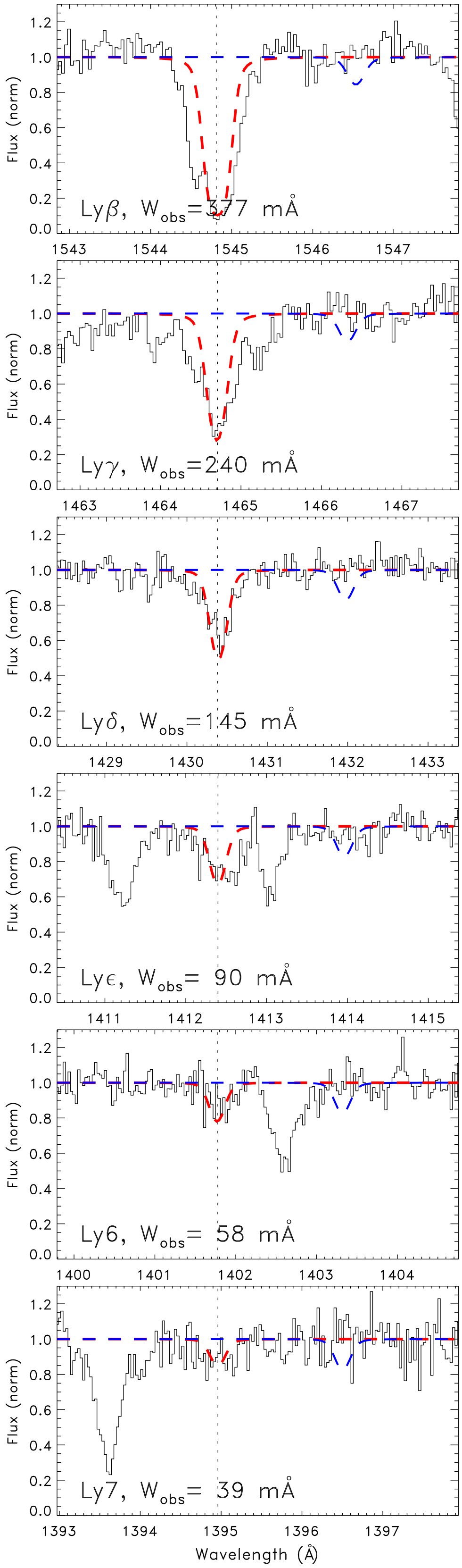

Figure 4. Six Lyman-series absorption lines toward HS 1102+3441 detected at the same redshift ($z_{\rm abs} = 0.50607$) and aligned in all panels. Observed-frame equivalent widths (EWs) range from 377 mÅ (Lyβ) to 39 mÅ (Ly7) and are fitted (red dashed lines) to a CoG with log $N_{\rm H\,I} = 15.07 \pm 0.02$ and $b = 25$ km s^{-1}. Mock absorbers with observed-frame EWs of 50 mÅ (blue-dashed lines) are inserted 300 km s^{-1} redward of each Lyman line. This simple example illustrates our ability to find such absorbers in data with S/N $\gtrsim 10$.

lines, these optical depths are

$$\tau_0({\rm Ly}\alpha) = (30.3) N_{15}\, b_{25}^{-1} \quad \tau_0({\rm Ly}\beta) = (4.86) N_{15}\, b_{25}^{-1}$$
$$\tau_0({\rm Ly}\gamma) = (1.69) N_{15}\, b_{25}^{-1} \quad \tau_0({\rm Ly}\delta) = (0.793) N_{15}\, b_{25}^{-1}, \quad (1)$$

for $N_{\rm H\,I}$ scaled to $(10^{15}\,{\rm cm}^{-2})N_{15}$. As long as some Lyman lines remain near the linear portion of the CoG, this method works well. For $b \approx 25$ km s^{-1}, the Lyα line begins to saturate ($\tau_0 > 1$ at log $N_{\rm H\,I} > 13.5$), producing large uncertainties at $14.5 <$ log $N_{\rm H\,I} < 16.5$.

In this paper, we focus on the stronger H I absorbers, using their Lyman decrements to derive accurate column densities over the range $16.2 \leqslant$ log $N_{\rm H\,I} \leqslant 17.85$. With our Lyman-comb technique and S/N $\geqslant 10$, we can detect the Lyman decrement at optical depths $\tau_{\rm LL} \geqslant 0.1$ corresponding to log $N_{\rm H\,I} \geqslant 16.2$. Once log $N_{\rm H\,I} \geqslant 17.85$ ($\tau_{\rm LL} > 4.46$), it becomes difficult to detect transmitted flux in the Lyman continuum. In a few cases with high S/N ($\gtrsim$20), we detected or limited the residual flux transmission equivalent to $\tau_{\rm LL} \geqslant 5.0$ (log $N_{\rm H\,I} \geqslant 17.9$). For high column density systems, we can constrain $N_{\rm H\,I}$ from damping wings in the Lyα line, when present (Lyα shifts out of the COS/G160M band at $z \gtrsim 0.47$). By combining the Lyman decrement (for log $N_{\rm H\,I} > 16.2$) with CoG methods on higher Lyman lines, typically up to Ly12 and occasionally to Ly15, we obtain more accurate column densities than with CoG alone.

The CoG fitting uses a series of Voigt profiles convolved with an appropriate COS line spread function.[4] Widely separated velocity components are identified semiautomatically (see Danforth et al. 2016), but closely blended components require interactive identification and fitting. We compare the models to the observed spectrum in normalized flux space via a χ^2 minimization package MPFIT (Markwardt 2009) with equivalent widths fitted to line profiles of each component (not to the observed flux). Moderately saturated lines with a simple component structure are well constrained by this method, and the CoG gives much better (N, b) solutions for H I than a single-line profile fit. Figures 5–8 illustrate our technique for Lyman-series and Lyman-decrement absorption for two LLSs with log $N = 17.85 \pm 0.02$ and log $N = 17.67 \pm 0.10$ and two pLLS absorbers with log $N_{\rm H\,I} = 16.41 \pm 0.03$ and 17.01 ± 0.05. The presence of a Lyman decrement typically yields a log $N_{\rm H\,I}$ accurate to ± 0.05 or better. Figure 9 shows spectra of the other eight strong H I absorbers with log $N_{\rm H\,I} > 17.0$.

Strong H I absorbers are often composed of multiple blended components. Lower-order Lyman lines are typically too strong to see blended components, but higher-order lines can reveal their presence. Absorbers where the minimized χ^2 solution fails to match the data may harbor an unresolved component structure. For example, in the strong absorber toward SBS 1108+560 (Figure 5), a weaker component is seen in the blue wing of Lyϵ and higher lines. When blended components are present, we fit a CoG to each component, using only lines in which they are unambiguously separable, eliminating lines contaminated with airglow emission or unrelated absorption. Line profiles and total column densities for the combined solution (e.g., N_1, b_1, z_1 and N_2, b_2, z_2) are then calculated and compared qualitatively to the stronger, lower-order Lyman lines. In several cases, the CoG solution does not reproduce the observed line profiles, or it differs from the Lyman decrement. The CoG is determined from the

[4] www.stsci.edu/hst/cos/performance/spectral_resolution

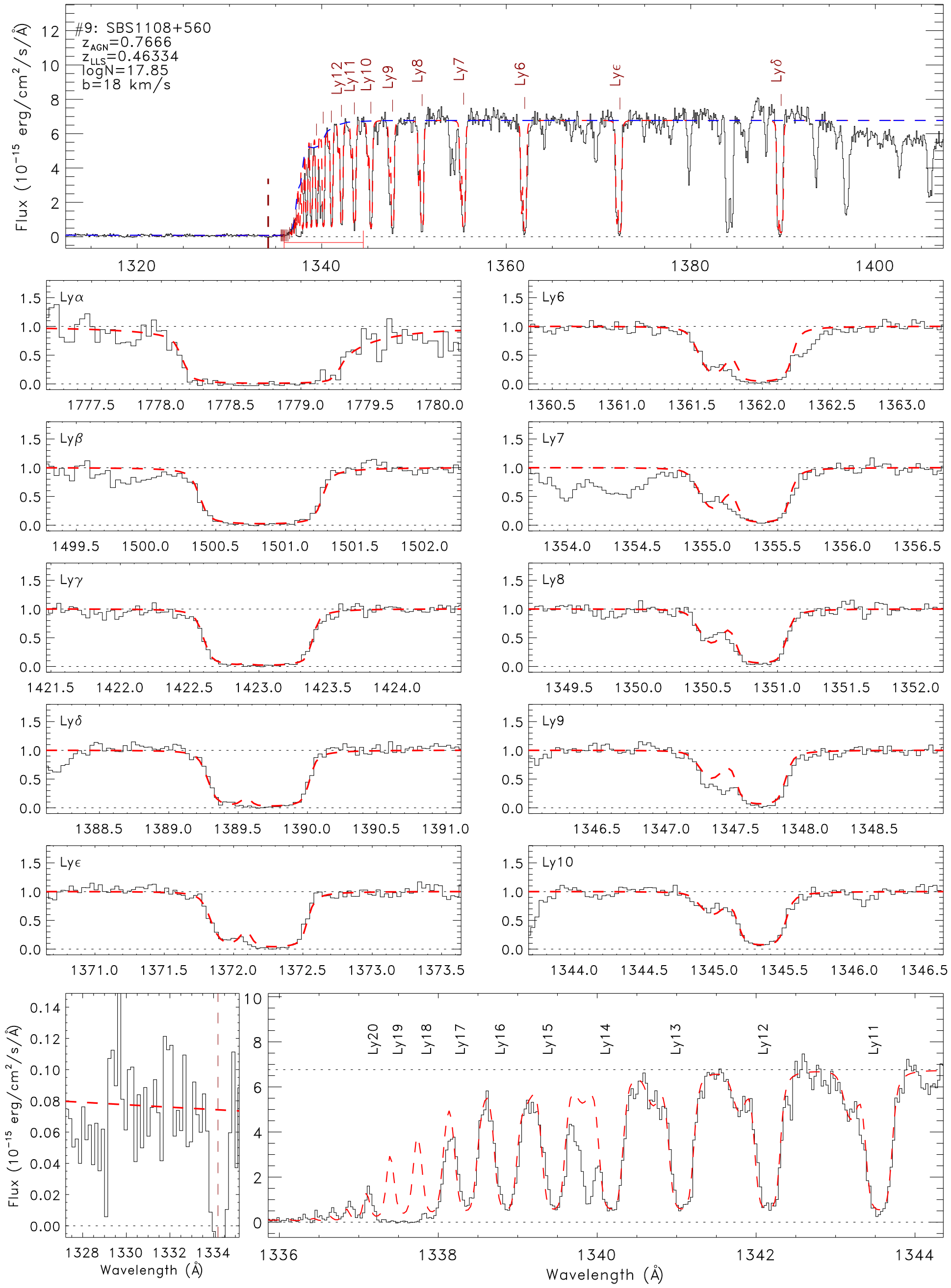

Figure 5. Top: normalized COS/G130M spectrum of SBS 1108+560 showing lines of system #9 at $z_{abs} = 0.46334$, an LLS with Lyman lines (Ly6–Ly12) converging on LL at 1334.2 Å (vertical red dashed line). Red dashed lines in the spectrum show the model with column density log $N_{\rm H\,I} = 17.85 \pm 0.02$ and Doppler parameter $b = 18 \pm 2$ km s^{-1}, not fits to individual lines. Middle panels: line profiles of Lyman lines (Lyα–Ly10). Bottom: higher Lyman lines (Ly11–Ly20) and transmitted flux in LyC. Note the C II λ1334.53 interstellar absorption in the LyC (bottom left panel).

measured equivalent widths of the lines. Sometimes a solution with a smaller b and larger N (or vice versa) is required to match the observed line profiles or decrement.

2.2. Lyman Line Overlap and Velocity Components

The CoG techniques generally give accurate results with the availability of higher Lyman lines. However, line overlap sets in at Ly15 ($\lambda = 915.329$ Å) or Ly16 ($\lambda = 914.919$ Å) as the higher Lyman series converges on the Lyman limit at $\lambda_{\rm LL} = 911.753$ Å. Line crowding and uncertain continuum placement make measurements of equivalent widths difficult when the wavelength separation, $\Delta\lambda_{n,n+1}$, between sequential Lyman lines is comparable to their line width. Table 2 shows line separations and line-center optical depths for Ly12–Ly24, scaled to the ratio, N_{17}/b_{25}, for column densities $N_{\rm H\,I} = (10^{17}\ {\rm cm}^{-2})\ N_{17}$. The lines are distinguishable up to Ly15, where $\Delta\lambda_{n,n+1} \approx 0.5$ Å. For Gaussian line profiles, the full width at half maximum is $\Delta\lambda_{\rm FWHM} = 2(\ln 2)^{1/2}(\Delta\lambda_D) \approx (0.127$ Å$)\ b_{25}\lambda_{914}$, where λ_{914} is a typical (L15–Ly20) wavelength in units of 914 Å and $\Delta\lambda_D = \lambda_0\ (b/c)$ is the Doppler width. Severe overlap sets in above Ly20, where separations become less than 0.2 Å. At this point, higher Lyman lines overlap in their wings, 10% below the continuum, defined by

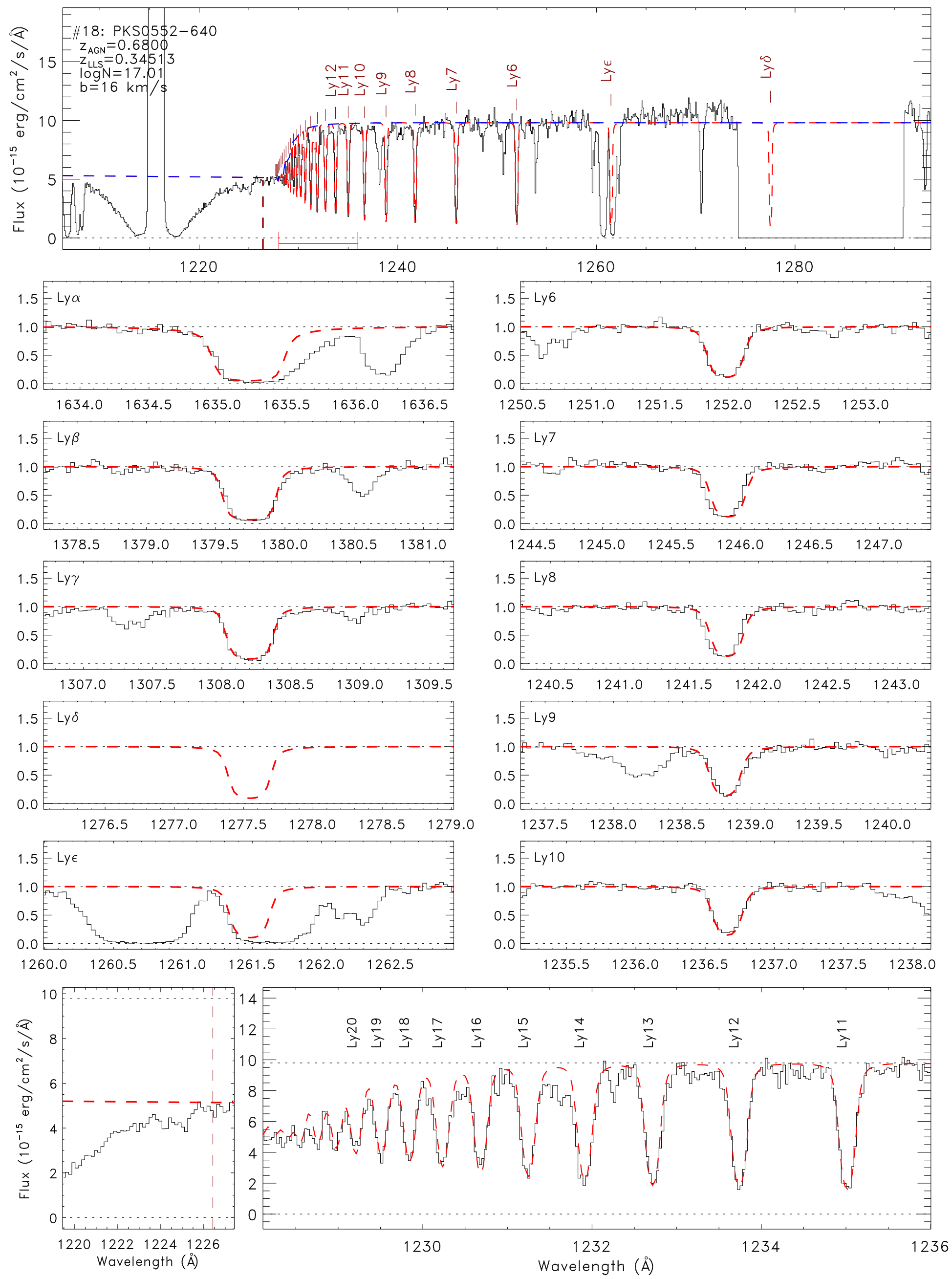

Figure 6. Same as Figure 5 for pLLS toward PKS 0552-640 (system #18 at $z_{\mathrm{abs}} = 0.34513$) with LL at 1226.4 Å. The redward wing of Galactic Lyα absorption extends from 1216 to 1226 Å. Red dashed lines in the spectrum show profiles of Lyman lines (Lyα–Ly10) for the model with log $N_{\mathrm{H\,I}} = 17.01 \pm 0.05$ and $b = 16 \pm 2$ km s^{-1}. Bottom: higher Lyman-series lines (Ly11–Ly20) and transmitted flux in LyC above the Galactic DLA.

width $\Delta\lambda_{10\%} = 2\ (\ln\ 10)^{1/2}\ (\Delta\lambda_D) \approx (0.231\ \text{Å})\ b_{25}\lambda_{914}$. A few absorbers have $b = 40$–50 km s^{-1}, with wing overlap affecting Ly14–Ly17 at line separations of 0.4–0.5 Å.

Overlap creates difficulties in measuring equivalent widths, with offsetting effects of shared line absorption and continuum placement. Multiple velocity components complicate the problem further, and a proper treatment requires multiline radiative transfer. Therefore, we do not include lines above Ly15 in our analysis, as illustrated in Figure 10 for the absorber toward PKS 0552–640. The standard CoG up to Ly15 gives log $N_{\mathrm{H\,I}} = 17.01 \pm 0.05$, whereas including additional (overlapping) lines from Ly16 to Ly24 gives an erroneous fit with log $N_{\mathrm{H\,I}} = 16.81 \pm 0.02$. In this case, the observed Lyman decrement provides an accurate column density, log $N_{\mathrm{H\,I}} = 17.01 \pm 0.03$, verifying the CoG solution up to Ly15.

Appendix A provides a narrative discussion for our analysis of 73 strong H I absorbers with log $N_{\mathrm{H\,I}} > 15.75$. For several absorbers with log $N_{\mathrm{H\,I}} > 16.25$, our combination of CoG fits and Ly decrement measurements uncovered a few discrepancies with previous values in the literature (Fox et al. 2013; Lehner et al. 2013; Stevans et al. 2014). For four systems with well-resolved

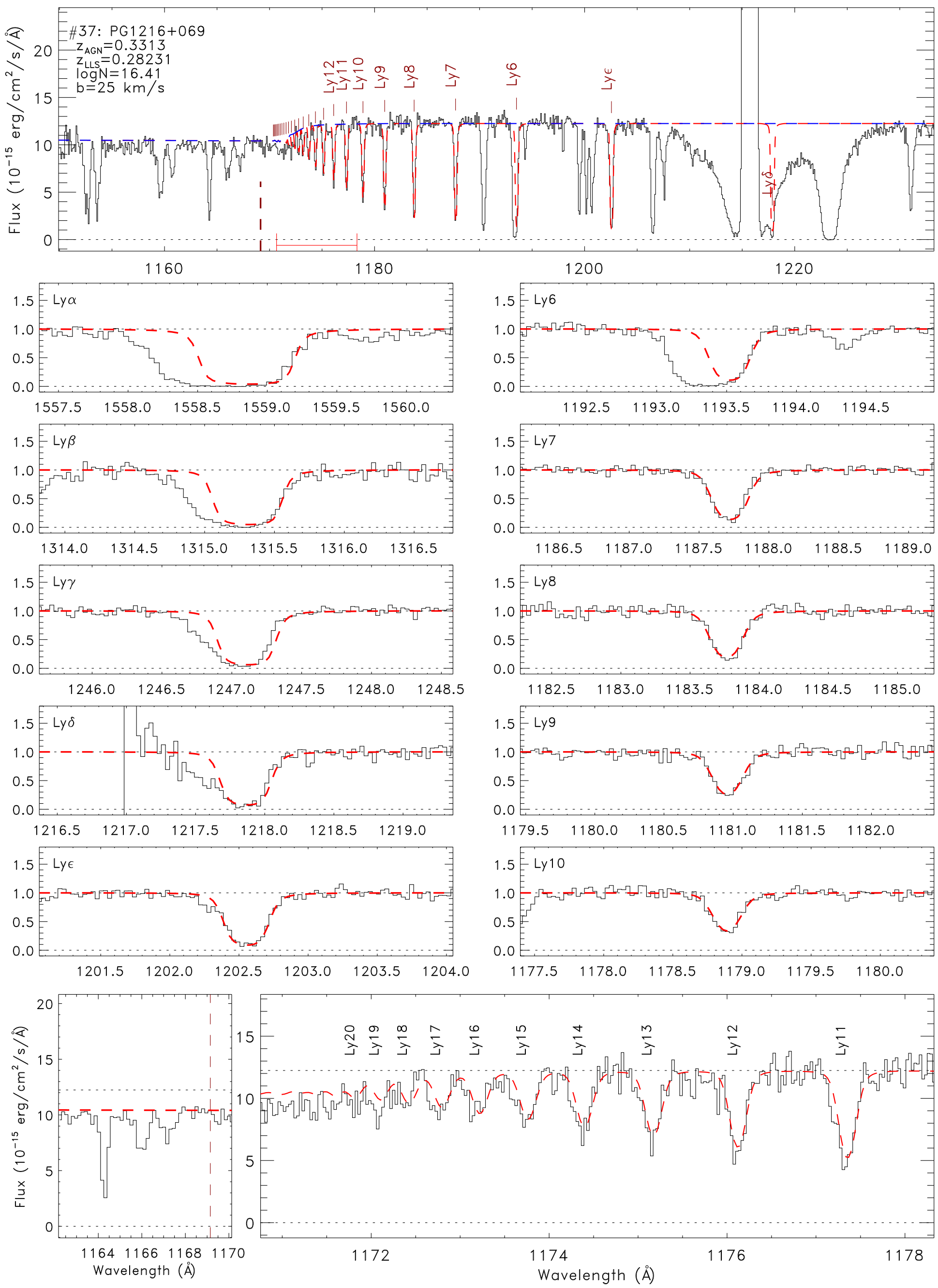

Figure 7. Same as Figure 5 for pLLS toward PG 1216+069 (system #37 at $z_{\rm abs} = 0.28231$). Absorption lines converge on LL at 1161.15 Å. Red dashed lines (Lyϵ–Ly10) show the strongest component fitted to CoG with log $N_{\rm H\,I} = 16.41 \pm 0.03$ and $b = 25 \pm 5$ km s^{-1}. The Lyman decrement gives $\tau_{\rm LL} = 0.16 \pm 0.02$ or log $N_{\rm H\,I} = 16.40 \pm 0.06$. Bottom: higher Lyman lines (Ly11–Ly20) and transmitted flux in LyC.

velocity components separated by 150–200 km s^{-1} or greater, we treated the components as separate absorbers: systems #24abc, #47abc, #59ab, and #60ab.

3. Results

To analyze the bivariate distribution, $f(N, z)$, of H I absorbers, we group them into a binned array, $F(i, j)$, shown in Table 3, with redshift indices (i = 1–15) and column density indices (j = 1–15). The 15 redshift bins have equal width $\Delta z = 0.04$ for z = 0.24–0.84. The first 12 column-density bins have width Δ (log $N_{\rm H\,I}$) = 0.25 spanning 14 < log $N_{\rm H\,I} \leqslant 17$. The last three bins ($j$ = 13, 14, 15) are wider and cover the 10 strongest absorbers with log $N_{\rm H\,I}$ = 17.0–20.5. As shown in Table 1 (column 4), the higher Lyman lines (Lyγ, Lyδ, Lyϵ) are easily detectable, at 50 mÅ equivalent width, for column densities log $N_{\rm H\,I} \geqslant$ 14.3–14.9. Because the best COS data have S/N > 20, we have regularly detected the first three Lyman lines (Lyα, Lyβ, Lyδ) and often even higher Lyman lines (Figure 3). This allows us to identify absorbers with log $N_{\rm H\,I}$ = 14–15, even though the Lyman edge is undetectable at these column densities. The LLS and stronger pLLS absorbers with log $N_{\rm H\,I}$ > 16.5 are typically observed in higher Lyman lines up to Ly12 and often beyond (see Figures 5–9), and they yield precise H I column densities via the CoG. At higher redshifts, the two strongest Lyman lines move out of the

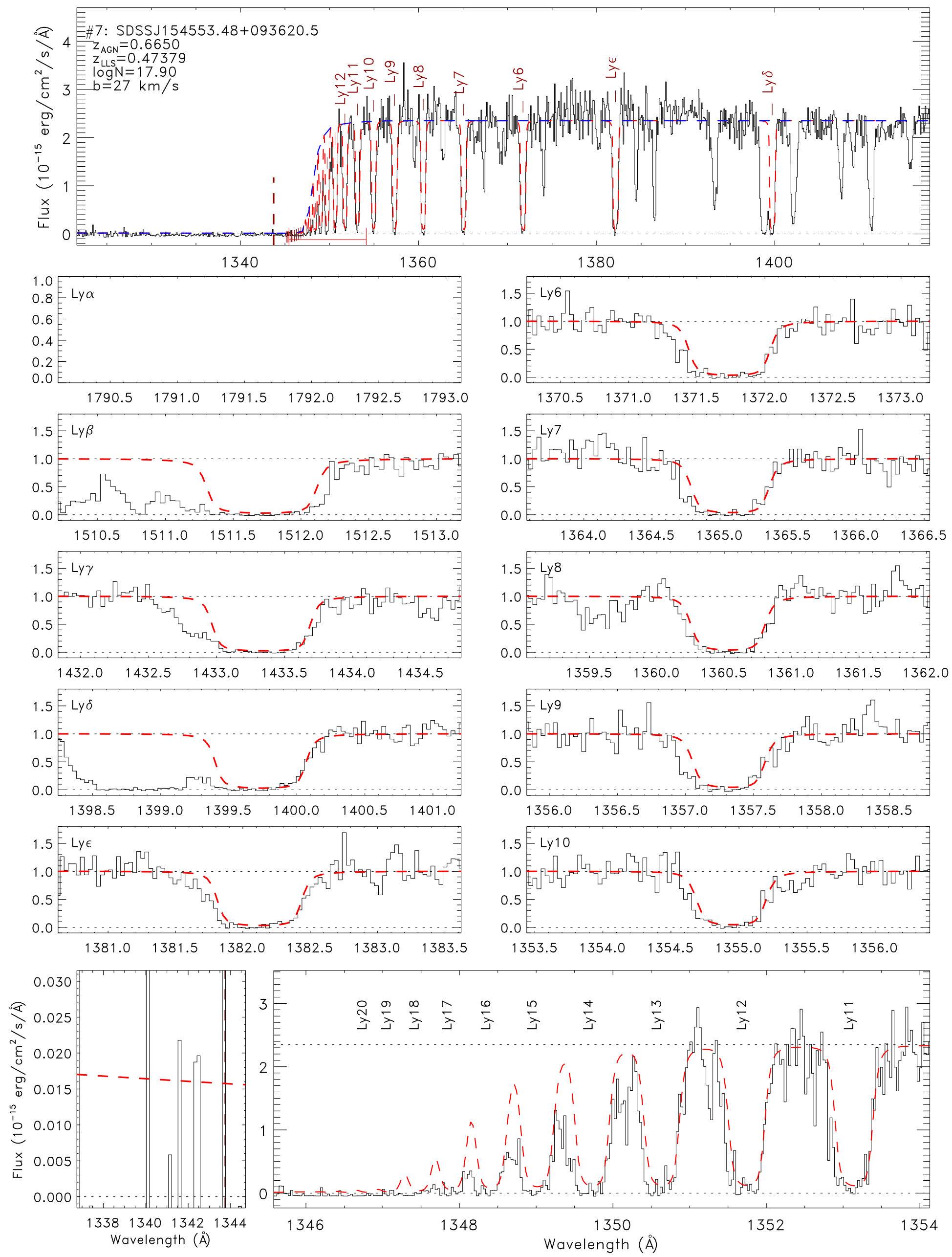

Figure 8. Same as Figure 5 for LLS toward SDSS J154553.48+093620.5 (system #7 at $z_{\rm abs} = 0.47379$). Absorption lines of Ly6–Ly12 converge on LL at 1343.7 Å. Red dashed lines (Lyβ–Ly10) show the strongest component fitted to the CoG with log $N_{\rm H\,I} = 17.67 \pm 0.15$ and $b = 35 \pm 1$ km s^{-1}. This column density would give $\tau_{\rm LL} = 2.95$ and a transmitted flux of 5.25%, inconsistent with observations of flux below the LL (bottom panels), which imply log $N_{\rm H\,I} \geqslant 17.9$.

G160M window (Lyα at $z > 0.47$ and Lyβ at $z > 0.75$). Because our higher-redshift H I detections rely on Lyγ and higher lines, we could miss a few absorbers with log $N_{\rm H\,I} = 15.0$–15.5. Column densities for strong absorbers can sometimes be influenced by velocity components. In well-exposed COS spectra, we can identify components with $\Delta v = 40$–400 km s^{-1}, all of which contribute to the Lyman decrement. We derive individual column densities with multi-component CoGs, which could affect absorber counts for the bins with log $N_{\rm H\,I} = 14.75$–16.00. We have taken a conservative approach, only splitting the velocity components in four well-separated systems with $\Delta v \geqslant 150$–200 km s^{-1}.

The observed distribution in column density (Table 3) exhibits the expected falloff in numbers at high column densities owing to their scarcity. We believe the decrease in absorber numbers in bins j = 1–4 (log $N_{\rm H\,I}$ = 14–15) arises primarily from the lower detection sensitivity of weak Lyman lines at higher redshift. Because the LL is not detectable at log $N_{\rm H\,I} < 16.2$, we rely on finding a pattern of higher Lyman lines (Lyγ, Lyδ, Lyϵ) whose detection in the G160M window requires log $N_{\rm H\,I} \geqslant 14.3$–14.9 (Table 1). These higher Lyman lines are easily detected in G130M (see Figure 3), but at $z > 0.5$ we rely on G160M and higher (weaker) lines in the Lyman series. For this reason, we focus our attention on pLLS and LLS absorbers with log $N_{\rm H\,I} \geqslant 16.0$. Our statistical analysis in Appendix B restricts the H I absorber sample to the ranges $0.24 \leqslant z_{\rm abs} \leqslant 0.84$ and $15 \leqslant \log N_{\rm H\,I} \leqslant 20$, where we feel confident in detecting most systems in AGN sight lines

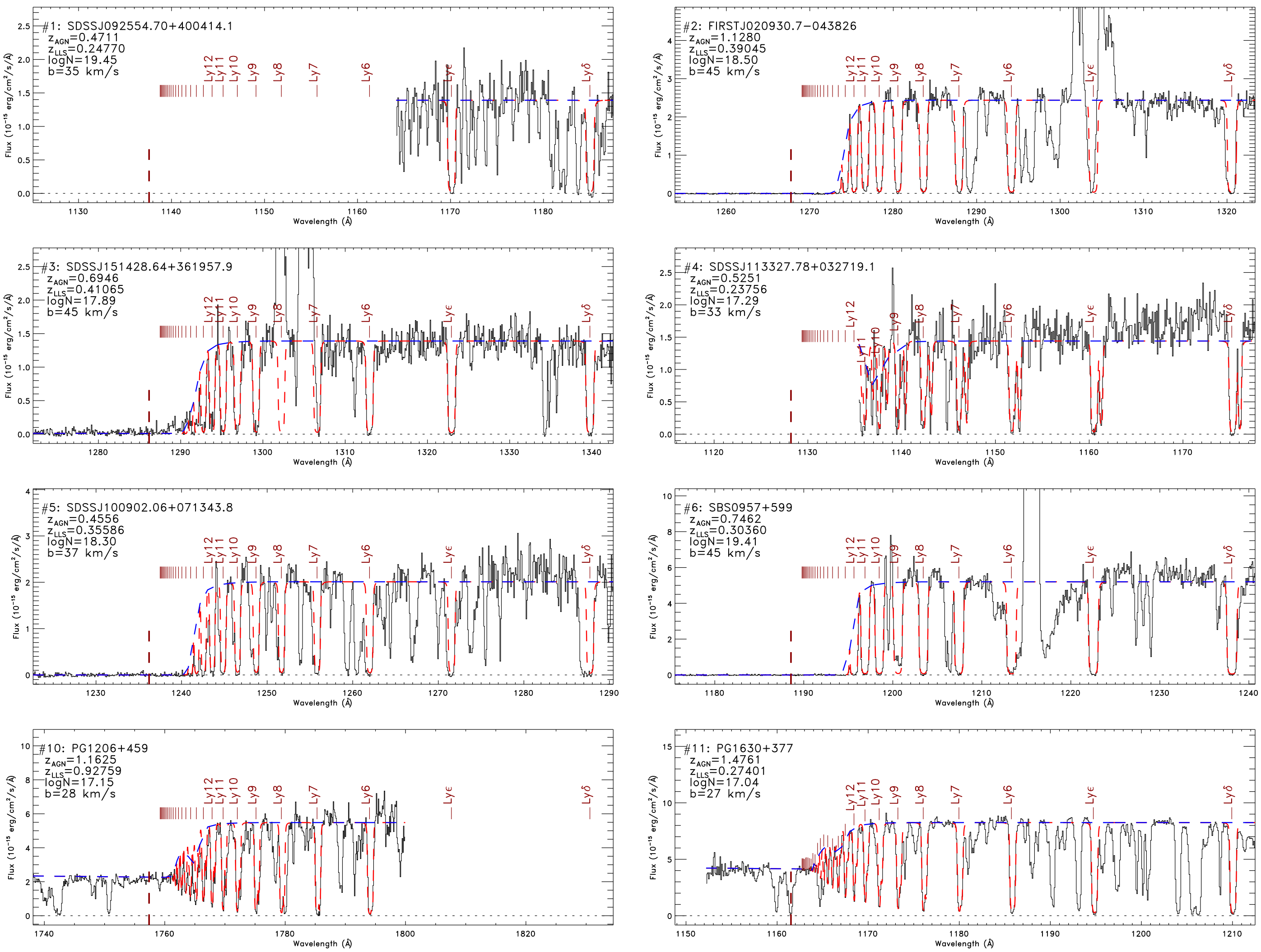

Figure 9. COS spectra of eight strong H I absorbers ($\log N_{\rm H\,I} > 17.0$), listed in Appendix A as systems #1–6, #10, and #11 (see labels in top left corner). These include six LLSs and two pLLSs ($\log N_{\rm H\,I} = 17.15$ and 17.04). Other strong absorbers were shown in Figures 4, 5, and 7. Spectra for systems #1 and #10 are limited by cutoffs of the settings of the G130M and G160M gratings. Additional Lyman lines beyond those shown were available in many cases.

with well-exposed COS spectra (S/N > 10). Our LLS sample is restricted to $0.24 \leqslant z \leqslant 0.48$, as described in Section 3.3. This technique differs from that in our recent IGM survey (Danforth et al. 2016), which detected primarily weak H I absorbers through Lyα lines.

3.1. Redshift Coverage per Bin

The total (effective) redshift path length, $\Delta z_{\rm eff}^{\rm (tot)}$, is found from the spectral coverage of the AGNs in our survey. We chose redshift bins of width $\Delta z = 0.04$, starting at bin 1 ($0.24 < z < 0.28$), where the Lyman edge at wavelength $\lambda_{\rm LL} = (911.753\,\text{Å})(1+z)$ first falls within the range of most COS/G130M data (1134–1459 Å). Table 4 shows the number of AGNs with sensitivity to detecting an LL in each redshift bin. Each AGN with redshift above the bin contributes a path length $\Delta z = 0.04$, plus partial redshift coverage for a few AGNs whose redshifts fall within the bin. The redshift-bin path lengths, $\Delta z_{\rm eff}^{(i)}$, are shown in column 5 of Table 4. To determine this redshift path, we subtracted a few spectral regions blocked by strong absorbers ($\log N_{\rm H\,I} > 17$) along 10 AGN sight lines shown in Table 5. In practice, only a few of the strongest LLS absorbers, with $\log N_{\rm H\,I} > 17.5$, produce significant blockage. Strong foreground absorption by the Galactic interstellar H I (Lyα) does not impact $\Delta z_{\rm eff}$ or the Lyman comb, since it usually blocks only one of the Lyman lines.

With the far-UV spectral coverage between 1134 Å and 1795 Å and the availability of many lines in the Lyman series, we were able to detect strong H I systems in $z_{\rm abs} = 0.237$–0.928. Because of the reduced spectral coverage of higher-redshift AGNs, we limited our analysis to 15 redshift bins in $z = 0.24$–0.84. Sensitivity to higher Lyman lines declines at $z > 0.846$ as Lyγ shifts out of the COS/G160M band. The total path length in this sample (Table 4) is $\Delta z_{\rm eff}^{\rm (tot)} = 31.94$. For individual bins, the path length decreases from $\Delta z_{\rm eff}^{(i)} = 3.83$ for bin 1 ($\bar{z} = 0.26$ and $\lambda_{\rm LL} = 1149$ Å) to $\Delta z_{\rm eff}^{(i)} = 2.80$ for bin 5 ($\bar{z} = 0.42$ and $\lambda_{\rm LL} = 1295$ Å). Although bin 5 covers the redshift ($z = 0.423$) at which Lyβ shifts out of G130M, spectral overlap with G160M (1400–1459 Å) allows Lyβ to be continuously observed to $z = 0.75$. The Lyman edge shifts out of G130M beyond bin 9 ($0.56 < z < 0.60$), and the AGN path length drops to $\Delta z_{\rm eff}^{(i)} \approx 0.74 - 0.96$ in bins 13–15. With G160M, we have detected pLLSs out to $z = 0.928$. Wavelength overlap between the G130M and G160M gratings (1400–1459 Å) slightly enhances our ability to discover Lyα

Table 2
Line Overlap Parameters (Higher Lyman Lines)[a]

Lyman (n)	λ_0 (Å)	$\Delta\lambda_{n,\,n+1}$	f_n (in 10^{-4})	$\tau_0^{(n)}$ ($\times N_{17}/b_{25}$)
Ly12	917.1805	0.949 Å	7.231	3.97
Ly13	916.4291	0.751 Å	5.777	3.17
Ly14	915.8238	0.605 Å	4.689	2.57
Ly15	915.3289	0.495 Å	3.858	2.12
Ly16	914.9192	0.410 Å	3.212	1.76
Ly17	914.5762	0.343 Å	2.703	1.48
Ly18	914.2861	0.290 Å	2.297	1.26
Ly19	914.0385	0.248 Å	1.968	1.08
Ly20	913.8256	0.213 Å	1.699	0.930
Ly21	913.6411	0.185 Å	1.477	0.808
Ly22	913.4803	0.161 Å	1.293	0.707
Ly23	913.3391	0.141 Å	1.137	0.622
Ly24	913.2146	0.125 Å	1.006	0.550

Notes.
[a] Wavelength separations ($\Delta\lambda_{n,n+1}$) between Lyman transitions, λ_n and λ_{n+1}, and optical depths, $\tau_0^{(n)}$. Here, Ly n denotes the transition $(n+1)p \rightarrow 1s$ and line-center optical depth $\tau_0^{(n)} = (0.5474)\, N_{17}\, b_{25}^{-1} f_{-4}\, \lambda_{914}$, with $N_{\rm H\,I} = (10^{17}\ {\rm cm^{-2}})N_{17}$ and Doppler parameter scaled to $b = 25$ km s^{-1}. Oscillator strengths f_n (in units of 10^{-4}) and wavelengths (λ_0 scaled to 914 Å) are from Morton (2003).

absorbers at $z = 0.15$–0.20, Lyβ absorbers at $z = 0.36$–0.42, and Lyγ absorbers at $z = 0.44$–0.50. However, this effect is minor. Because pLLS identification requires finding a pattern of several Lyman lines, our survey is most sensitive in the range $z \approx 0.24$–0.84.

Selection biases arise toward several high-z AGNs that are less likely to contain strong LLSs and DLAs (see Sections 3.3 and 3.4). Our sample of 159 AGNs (Stevans et al. 2014) contains 29 targets at $z > 0.70$ and 43 at $z > 0.60$, many of them observed previously by *IUE*, *HST*, and *FUSE*. To be detected in the G130M/G160M gratings, these AGN were "UV-qualified" for sufficient far-UV flux, usually by *GALEX* or *IUE*. A number of these AGNs came from the COS-Halos project (Tumlinson et al. 2013), whose QSOs were selected to have high fluxes in the *GALEX* far-UV band and avoid strong Mg II absorbers at $z_{\rm abs} > 0.4$.

3.2. Bivariate Distribution in log N and z

Table 6 lists 41 strong H I absorbers with log $N_{\rm H\,I} \geqslant 16.0$, classified as LLSs or pLLSs (systems #1–40 and #73 from Appendix A). The last columns compare our column densities to previous measurements from Lehner et al. (2013) and estimates from Stevans et al. (2014). The Lehner values are the same as those reported by Fox et al. (2013). Those from Stevans et al. (2014) were estimates, many of which were revised in this paper after careful analysis of CoGs and Lyman decrements. For 158 absorbers above our expected detection limit (log $N_{\rm H\,I} \geqslant 15.0$), the absorber frequency per redshift is $d\mathcal{N}/dz \approx 4.95 \pm 0.39$ averaged over $0.24 < z < 0.84$. We see some indication of an increase in frequency with redshift. Figure 11 shows the distribution in column density for our pLLS data, together with the Lyα forest distribution from Danforth et al. (2016). Some offset is expected, as the COS Lyα forest survey covers $z < 0.47$ with median redshift $z_{\rm abs} = 0.14$, whereas our pLLS survey spans $0.24 < z < 0.93$ with median $z_{\rm abs} = 0.43$. The eight detected LLSs range from

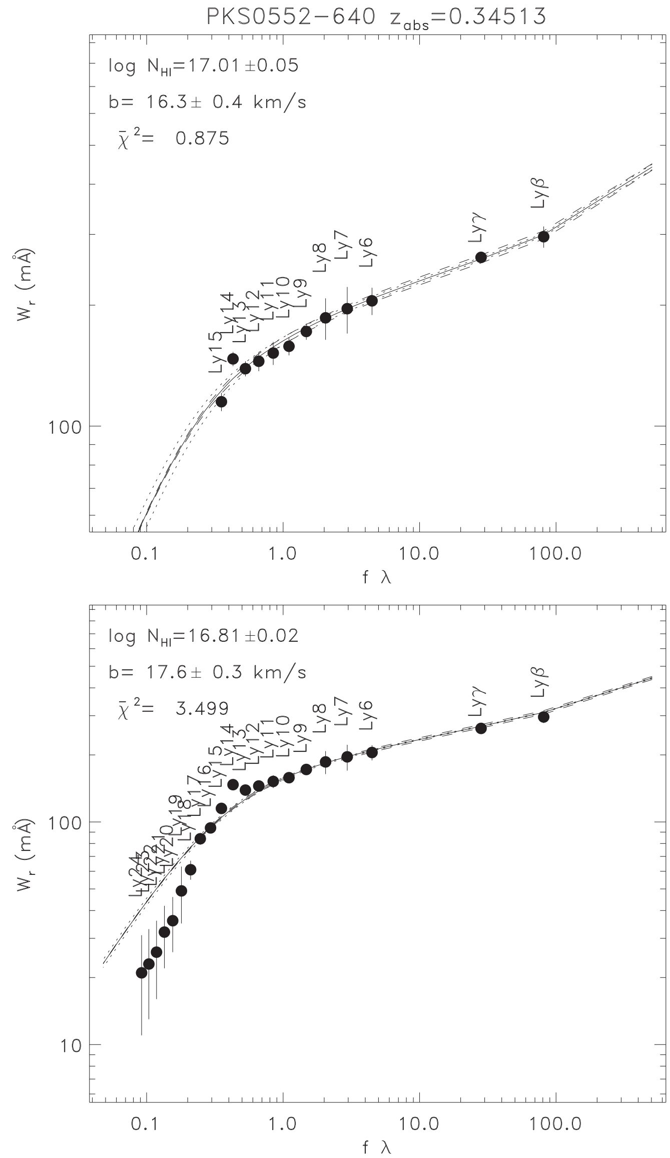

Figure 10. Top: curve of growth of the Lyman series (Lyβ through Ly15) for pLLS toward PKS 0552-640 at $z_{\rm abs} = 0.34513$ (see Figure 6). Equivalent widths (W_λ in mÅ) are plotted versus line strengths, $f\,\lambda$, with oscillator strengths f and wavelengths λ(Å) from Morton (2003). The best fit gives log $N_{\rm H\,I} = 17.01 \pm 0.05$ with $b = 16.3 \pm 0.4$ km s^{-1} (reduced χ^2 noted in header). Bottom: CoG including lines of Ly16–Ly24. Line overlap and crowding result in reduced equivalent widths and an erroneous fit with log $N_{\rm H\,I} = 16.81 \pm 0.02$ and $b = 17.6 \pm 0.3$ km s^{-1}.

$z = 0.237$ to 0.474, with median redshift $z_{\rm abs} = 0.39$. The absence of LLSs at $z > 0.48$ is surprising statistically, as we expected to detect $3.6^{+3.1}_{-1.8}$ LLSs in the range $0.48 < z < 0.84$ based on the derived redshift evolution (Section 3.3). This may be evidence for a bias toward AGNs with high far-UV fluxes, unblocked by LLSs at $z > 0.5$. We do not see this effect for the stronger pLLSs with log $N_{\rm H\,I} = 16.5$–17.0. For pLLS statistics, we use the full redshift range ($0.24 \leqslant z \leqslant 0.84$) but restrict the LLS sample to bins 1–6 ($0.24 \leqslant z \leqslant 0.48$).

The Lyα forest and pLLS distributions match fairly well at log $N_{\rm H\,I} \geqslant 16$. A possible turnover in the pLLS distribution appears at log $N_{\rm H\,I} < 15.5$, which could mark the onset of survey incompleteness. Because of the small number of absorbers, one expects fluctuations in the range log $N_{\rm H\,I} = 15.0$–16.0 (bins $j = 5$–8 in Table 3). The two surveys agree for

Table 3
Absorber Distribution in Redshift and Column Density[a]

z-bin	1	2	3	4	5	6	7	8	9	10	11	12	13	14	15	$N_{\rm tot}$	Redshifts
($i = 1$)	2	0	4	5	5	3	2	1	2	2	0	0	1	0	1	[28]	0.24–0.28
($i = 2$)	0	5	1	5	2	4	1	0	3	2	0	0	0	0	1	[24]	0.28–0.32
($i = 3$)	1	1	1	1	2	4	3	0	5	2	0	0	1	0	2	[23]	0.32–0.36
($i = 4$)	0	1	3	5	5	0	1	0	1	0	0	2	0	0	1	[19]	0.36–0.40
($i = 5$)	0	0	3	8	3	1	6	1	1	1	2	1	0	1	0	[28]	0.40–0.44
($i = 6$)	0	1	1	0	1	4	2	2	0	1	0	1	0	1	1	[15]	0.44–0.48
($i = 7$)	0	0	1	0	3	0	3	0	0	2	1	0	0	0	0	[10]	0.48–0.52
($i = 8$)	1	0	0	0	2	1	2	2	3	2	0	1	0	0	0	[14]	0.52–0.56
($i = 9$)	0	0	1	0	3	2	3	0	1	0	0	0	0	0	0	[11]	0.56–0.60
($i = 10$)	0	0	1	1	1	2	3	2	1	1	1	0	0	0	0	[12]	0.60–0.64
($i = 11$)	0	0	0	0	2	0	1	2	1	0	0	0	0	0	0	[6]	0.64–0.68
($i = 12$)	0	0	0	0	0	2	3	0	0	2	2	0	0	0	0	[9]	0.68–0.72
($i = 13$)	0	0	0	0	0	2	0	0	1	0	1	1	0	0	0	[5]	0.72–0.76
($i = 14$)	0	0	0	1	0	0	1	0	0	0	0	0	0	0	0	[2]	0.76–0.80
($i = 15$)	0	0	0	0	2	0	3	0	3	0	1	0	0	0	0	[9]	0.80–0.84
Total	4	8	16	26	31	25	34	10	22	15	8	6	2	2	6	[215]	0.24–0.84

Note.
[a] Array $F(i, j)$ shows the number of H I absorbers per bin, with total numbers summed across rows and columns. In total, this table lists 211 absorbers: 158 (log $N_{\rm H\,I} \geqslant 15.0$), 60 (log $N_{\rm H\,I} \geqslant 16.0$), and 10 (log $N_{\rm H\,I} \geqslant 17.0$). Labels (i, j) denote redshift bins (i = 1–15) of width $\Delta z = 0.04$ from $0.24 \leqslant z \leqslant 0.84$ and column-density bins (j = 1–15) of width $\Delta \log N_{\rm H\,I} = 0.25$ except for bins 13, 14, and 15. Column density ranges of bins are as follows: (1) log $N_{\rm H\,I}$ = 14.00–14.25, (2) 14.25–14.50, (3) 14.50–14.75, (4) 14.75–15.00, (5) 15.00–15.25, (6) 15.25–15.50, (7) 15.50–15.75, (8) 15.75–16.00, (9) 16.00–16.25, (10) 16.25–16.50, (11) 16.50–16.75, (12) 16.75–17.00, (13) 17.00–17.50, (14) 17.50–18.00, (15) log $N_{\rm H\,I} \geqslant 18.00$. Five absorbers (systems #4, 10, 50, 70, and 72 in Appendix A) lie at redshifts outside the range of this table. Although they do not appear in the numbers above, they are included in the MCMC analysis of Appendix B.

bin 7 (15.50–15.75) and bin 9 (16.00–16.25), whereas bin 8 (15.75–16.00) has a low number of absorbers that may arise from the finite spacings in our survey grid, $\Delta z = 0.04$, Δ (log $N_{\rm H\,I}$) = 0.25. As noted above and in Table 1, we should be able to identify most absorbers in the range $15.0 < \log N_{\rm H\,I} < 15.5$. However, a small decrease in detection efficiency of weak absorbers could occur at $z > 0.47$, when Lyα shifts out of the G160M window. The absorber numbers in bins 6–9 could also be affected by velocity components within strong systems, which separate into distinct absorbers. The distinction between "systems" and "components" is a subtle one that we have not pursued beyond the obvious cases in systems #24abc, #47abc, #59ab, and #60ab (see Appendix A).

To analyze the bivariate differential distribution of absorbers in H I column density and frequency, we have applied a maximum-likelihood analysis (Appendix B) to the parameterized form $f(N, z) \equiv d^2\mathcal{N}/dz\, dN_{\rm H\,I} = C_0 N_{\rm H\,I}^{-\beta}(1+z)^{\gamma}$. We fitted all absorbers in the ranges $0.24 \leqslant z \leqslant 0.84$ and $15 \leqslant \log N_{\rm H\,I} \leqslant 20$, using Markov chain Monte Carlo (MCMC) simulations to derive values $\beta = 1.48 \pm 0.05$ and $\gamma = 1.14^{+0.88}_{-0.89}$. Figure 12 shows the 2D joint probability distributions in power-law parameters and their 1σ error bars. Both distributions are close to Gaussian, although the column-density distribution is much better constrained (3.4% error in β) than the redshift evolution index, γ. The uncertainty in γ is illustrated in Figure 13 with a histogram of the redshift distribution from z = 0.24–0.84. This evolution index is similar to those determined in our Lyα survey (Danforth et al. 2016). Over redshifts $0 < z < 0.47$, we found $\gamma_{\rm all} = 1.24 \pm 0.04$ for all absorbers with $\log N_{\rm H\,I} > 13$. Refitting the distribution of 65 absorbers at $\log N_{\rm H\,I} \geqslant 15.0$, we find $\gamma = 1.43 \pm 0.34$.

The normalization (C_0) of our MCMC distribution follows from integrating over observed (and fitted) ranges in redshift ($z_1 < z < z_2$) and column density ($N_1 < N_{\rm H\,I} < N_2$):

$$N_{\rm tot} = C_0 \int_{z_1}^{z_2} (1+z)^{\gamma}\, \Delta z_{\rm eff}(z)\, dz \times \int_{N_1}^{N_2} N_{\rm H\,I}^{-\beta}\, dN_{\rm H\,I} = (4.11 \times 10^{-6})\, C_0. \qquad (2)$$

In evaluating the integral over column density, we take $N_1 = 10^{15}\ {\rm cm^{-2}}$, $N_2 = 10^{20}\ {\rm cm^{-2}}$, and $\beta = 1.48$ to give 1.31×10^{-7}. The redshift integral gives 0.983, for $z_1 = 0.24$, $z_2 = 0.84$, $\gamma = 1.14$, and assuming $\Delta z_{\rm eff}(z)$ to be constant across the full redshift range with path length $\Delta z_{\rm eff}^{\rm (tot)} = 31.94$. Thus, we find $C_0 = 3.87 \times 10^7$ for $N_{\rm tot} = 159$ absorbers. If we weight $f(N, z)$ by the effective path lengths, $\Delta z_{\rm eff}(z_i)$, of the 15 individual redshift bins (Table 4), we find a slightly larger normalization, $C_0 = 4.12 \times 10^7$. We adopt $C_0 = 4 \times 10^7$ for $N({\rm cm^{-2}})$.

3.3. True Lyman-limit Systems

By convention, true LLSs are defined as absorbers with $\tau_{\rm LL} \geqslant 1$ or $\log N_{\rm H\,I} \geqslant 17.2$. Although most surveys follow this definition, several recent papers included pLLS absorbers with lower column densities in their lists. Because of the scarcity of low-redshift LLSs, extending the definition of LLS into the pLLS range creates samples with better statistics. In our survey, we retain standard definitions of LLS and pLLS ($16.0 < \log N_{\rm H\,I} < 17.2$) and analyze a total of 158 H I absorbers with $\log N_{\rm H\,I} \geqslant 15.0$ in the range z = 0.237–0.928. Of these, eight are true LLSs, one is a DLA ($\log N_{\rm H\,I} = 20.34 \pm 0.12$), and 54 are pLLSs. This *HST*/COS survey is one of the largest samples of strong H I absorbers at low redshift (full range of $0.237 \leqslant z \leqslant 0.928$). The eight LLSs are detected through their Lyman

Table 4
Redshift Distribution of H I Absorbers

Bin (i)	Redshift Range	$(N_{\rm AGN})$[a]	$(N_{\rm abs})$[b]	$(\Delta z_{\rm eff})^{(i)}$[a]	$(d\mathcal{N}/dz)$[b]
1	0.24–0.28	102	17 (28)	3.83	4.44(+1.36, −1.07)
2	0.28–0.32	96	13 (24)	3.74	3.48(+1.26, −0.95)
3	0.32–0.36	91	19 (22)	3.39	5.60(+1.60, −1.27)
4	0.36–0.40	81	10 (19)	3.08	3.25(+1.39, −1.01)
5	0.40–0.44	73	17 (28)	2.80	6.07(+1.86, −1.46)
6	0.44–0.48	66	13 (15)	2.40	5.42(+1.96, −1.48)
7	0.48–0.52	54	9 (10)	2.10	4.29(+1.96, −1.46)
8	0.52–0.56	51	14 (15)	1.98	7.07(+2.44, −1.87)
9	0.56–0.60	49	10 (11)	1.83	4.92(+2.25, −1.61)
10	0.60–0.64	43	10 (12)	1.67	5.99(+2.56, −1.86)
11	0.64–0.68	39	5 (6)	1.40	3.57(+2.42, −1.54)
12	0.68–0.72	31	9 (9)	1.17	7.69(+3.51, −2.52)
13	0.72–0.76	24	5 (5)	0.963	5.19(+3.51, −2.24)
14	0.76–0.80	23	1 (2)	0.849	1.18(+2.71, −0.97)
15	0.80–0.84	19	9 (9)	0.738	12.2(+5.6, −4.0)

Note.
[a] Number ($N_{\rm AGN}$) of AGN sight lines providing full or partial spectral coverage of the H I Lyman edge (912 Å) over redshift bins (i = 1–15). The effective redshift, $\Delta z_{\rm eff}$, is based on $N_{\rm AGN}$ subtracting partial coverage of bins and portions of spectra blocked by strong absorbers.
[b] Distribution ($N_{\rm abs}$) of 158 H I absorbers with $\log N_{\rm H\,I} \geqslant 15$ for the 15 redshift bins (from $0.24 \leqslant z \leqslant 0.84$). Values in parentheses are the number of absorbers with $\log N_{\rm H\,I} \geqslant 14$ (211 in all). The last column shows the frequency of absorbers per unit redshift, $d\mathcal{N}/dz \equiv N_{\rm abs}/\Delta z_{\rm eff}$, for $\log N_{\rm H\,I} \geqslant 15$. We compute ($1\sigma$) error bars for one-sided Poisson statistics (Gehrels 1986) on $N_{\rm abs}$. Over the total path length $\Delta z_{\rm eff} = 31.94$, the average absorber frequency is $d\mathcal{N}/dz \approx 4.95 \pm 0.39$. A full statistical analysis (MCMC) of the bivariate distribution, $f(N, z) \equiv (d^2\,\mathcal{N}_{\rm abs}/dz\;dN)$, is given in Appendix B.

decrements and in multiple Lyman lines using the COS G130M/160M gratings with resolution $R \approx 17{,}000$. The eight LLSs in our COS survey are distinct from those in the FOS study, and they are in the range $z_{\rm abs} = 0.2374$–0.4738 with median redshift $z_{\rm abs} = 0.39$. Extrapolating the pLLS distribution (Section 3.2) into the LLS regime, we expect a frequency

$$\left(\frac{d\mathcal{N}}{dz}\right)_{\rm LLS} = C_0(1+z)^{\gamma}\int_{N_1}^{N_2} N^{-\beta}\,dN \approx 0.44\,(1+z)^{\gamma} \quad (3)$$

for $C_0 = 4 \times 10^7$ and $\beta = 1.48$. For $\gamma = 1.14$, the predicted number of LLSs over the full survey, with $\Delta z_{\rm eff} = 31.94$ for $0.24 \leqslant z \leqslant 0.84$, would be $N_{\rm LLS} = 13.8^{+4.8}_{-3.8}$, larger than the observed seven (or eight) LLSs. We found no LLSs in redshift bins 7–15 ($0.48 \leqslant z \leqslant 0.84$), whereas we would expect statistically to observe $N_{\rm LLS} = 3.6^{+3.1}_{-1.8}$. For the restricted LLS range ($0.24 \leqslant z \leqslant 0.64$) in which the Lyman edge falls at $\lambda < 1495$ Å, the observed path length $\Delta z_{\rm eff} = 26.82$ over bins 1–10. We would then expect to observe $N_{\rm LLS} = 7.2^{+3.8}_{-2.8}$, in agreement with our survey numbers. This deficit suggests that some of the "high-redshift" ($z > 0.5$) AGN sight lines in our sample are biased *against* finding strong LLSs and DLAs that block their far-UV flux in the most sensitive portion (1420–1650 Å) of the *GALEX* far-UV band often used in QSO target selection. Many of these AGNs have been studied with previous UV spectrographs (*IUE*, *FUSE*, *HST*) based on their far-UV brightness. Although we found no LLSs in the range $0.48 \leqslant z \leqslant 0.84$, these AGN sight lines do contain strong pLLS absorbers ($16.5 \leqslant \log N_{\rm H\,I} \leqslant 17.2$) in the expected numbers. Thus, the AGN bias may only affect the statistics for stronger LLSs with $\tau_{\rm LL} > 2$.

To guard against potential LLS bias at $z > 0.5$, we restrict our LLS sample to $z \leqslant 0.48$ and analyze the seven LLSs in bins 1–6 over the surveyed path length $\Delta z_{\rm eff} = 19.24$. This leads to an LLS frequency $d\mathcal{N}/dz = 0.36^{+0.20}_{-0.13}$ at the median $z_{\rm LLS} = 0.39$. Translated to the standard form, $d\mathcal{N}/dz = N_0(1+z)^{\gamma}$, this frequency corresponds to $N_0 = 0.25^{+0.13}_{-0.09}$, after dividing by $(1+z)^{\gamma} \approx 1.46$ at the median redshift with $\gamma = 1.14$. This LLS frequency is in agreement with previous studies (see Table 7 for a summary). We begin with the *HST*/FOS Key Project survey of QSO absorption lines at $0.4 < z < 1.4$ (Bahcall et al. 1993). The LLSs in that sample were analyzed in two papers that parameterized the redshift evolution. Storrie-Lombardi et al. (1994) found $d\mathcal{N}/dz = (0.27^{+0.20}_{-0.13})(1+z)^{1.55\pm0.45}$ based on seven LLSs observed by FOS at $0.456 < z < 1.036$ with median redshift $z_{\rm abs} = 0.649$. Using the same seven LLSs, Stengler-Larrea et al. (1995) found $d\mathcal{N}/dz = (0.25^{+0.17}_{-0.10})(1+z)^{1.50\pm0.39}$. In a recent survey of strong absorbers at $z < 2.6$, Ribaudo et al. (2011a) analyzed 206 LLS and pLLS absorbers with low-resolution gratings ($R \approx 1000$) on STIS (G140L, G230L) and FOS (G140L). Most of the H I absorbers in that survey were at $z > 1$; Table 4 in their paper lists five absorbers at $z < 0.5$ (three true LLSs) and 22 absorbers at $z < 0.84$ (17 LLSs). From their LLS sample with $\tau_{\rm LLS} \geqslant 1$, they fitted the evolution to $d\mathcal{N}/dz = (0.28)(1+z)^{1.19\pm0.56}$ over $0.25 < z < 2.59$. In general, the number of low-redshift ($z < 1$) LLSs reported in the literature is small, with just seven LLSs in the *HST*/FOS Key Project and eight in our *HST*/COS survey (these eight are distinct from those seen with FOS). We are also aware of three LLSs at $z < 0.24$, found by the *FUSE* satellite in the far-UV:

PHL 1811 ($z_{\rm abs} = 0.080923$), $\log N_{\rm H\,I} = 17.98 \pm 0.05$ (Jenkins et al. 2005);

PKS 1302-102 ($z_{\rm abs} = 0.09487$), $\log N_{\rm H\,I} = 17.2 \pm 0.2$ (Cooksey et al. 2008);

and PKS 0312-77 ($z_{\rm abs} = 0.2028$), $\log N_{\rm H\,I} = 18.22^{+0.19}_{-0.25}$ (Lehner et al. 2009).

Table 5
Strong Absorbers and Wavelength Blockage[a]

QSO[b]	$z_{\rm abs}$	log $N_{\rm H\,I}$	$z_{\rm QSO}$	Affected	Wavelength Blockage
1	0.24770	19.45 ± 0.10	0.47114	Bin 1	opaque below 1137.6 Å
2	0.39043	18.1 ± 0.1	1.131	Bins 1–4	opaque below 1267.7 Å
3	0.41065	17.80 ± 0.05	0.694596	Bins 1–5	opaque below 1286.2 Å
4	0.23740	17.29 ± 0.11	0.5251	...	opaque below 1128.2 Å
5	0.35586	18.3 ± 0.2	0.4556	Bins 1–3	opaque below 1236.2 Å
6	0.30360	19.41 ± 0.12	0.7462	Bins 1–2	opaque below 1188.6 Å
7	0.47379	18.3 ± 0.2	0.665	Bins 1–6	opaque below 1343.7 Å
8	0.41924	16.80 ± 0.05	0.4632	Bins 1–5	minor influence below 1294.0 Å
9	0.46334	17.85 ± 0.02	0.7666	Bins 1–6	opaque below 1334.2 Å
10	0.92772	17.15 ± 0.05	1.1625	Bins 1–14	minor influence below 1757.6 Å

Notes.
[a] Potential spectrum blockage by 10 strong absorbers listed with redshifts $z_{\rm abs}$ and fitted column densities, log $N_{\rm H\,I}$. Absorber column densities and redshifts are revised from values in Stevans et al. (2014), based on analysis of the Lyman limit flux decrement and new fits to CoGs for high-order Lyman lines. See Appendix B for details. In eight cases, strong LyC absorption produces flux decrements at wavelengths $\lambda \leqslant (911.753\ \text{Å})(1 + z_{\rm abs})$ listed in the comments. Potentially affected bins are noted. However, our survey can still find pLLSs by detecting higher Lyman lines longward of the Lyman edge.
[b] QSO targets: (1) SDSS J092554.70+400414.1; (2) FIRST J020930.7-043826; (3) SDSS J151428.64+361957.9; (4) SDSS J113327.78+032719.1; (5) SDSS J100902.06+071343.8; (6) SDSS J100102.55+594414.3; (7) SDSS J154553.48+093620.5; (8) SDSS J091029.75+101413.6; (9) SBS 1108+560; (10) PG 1206+459.

We return to the observed deficit of LLSs at $z > 0.48$, below the expected numbers given the fitted line frequency. The COS-Halos survey (Tumlinson et al. 2013) selected 39 UV-bright QSOs (*GALEX* far-UV magnitudes <18.5) with median redshift $z_{\rm AGN} = 0.525$. They avoided QSOs with strong (equivalent width >1 Å) Mg II absorbers at $z > 0.4$ and advise that their QSOs at $z > 0.4$ are not expected to provide an unbiased sample of LLSs. Our sample of 102 AGNs with $z_{\rm AGN} \geqslant 0.24$ includes 37 targets from the COS-Halos sample: 20 at $z_{\rm AGN} > 0.5$, 14 at $z_{\rm AGN} > 0.6$, and nine with $z_{\rm AGN} = 0.713$–0.887. We also have seven UV-bright (Palomar-Green) quasars observed with *IUE* (Tripp et al. 1994): PG 1407+265 ($z = 0.946$), PG 1148+549 ($z = 0.975$), PG 1206+459 ($z = 1.1625$), PG 1338+416 ($z = 1.21422$), PG 1522+101 ($z = 1.32785$), Q 0232-042 ($z = 1.437$), and PG 1630+377 ($z = 1.476$). Our sample includes several UV-bright AGNs (e.g., SBS 1108+560 at $z = 0.766619$, SBS 1122+594 at $z = 0.8514$) from the *HST* GTO Program and Guest Investigator Programs 11248, 11264, 11585, 11598, and 11741, with diverse scientific goals including intergalactic absorbers (Danforth et al. 2016), high-redshift absorbers (Ribaudo et al. 2011b; Tripp et al. 2011), galaxy–quasar pairs (Keeney et al. 2006; Crighton et al. 2010; Meiring et al. 2011; Stocke et al. 2013; Tumlinson et al. 2013; Bordoloi et al. 2014), and interstellar high-velocity clouds (Shull et al. 2009). Several of these high-z AGNs were selected to study intervening Ne VIII absorbers and the hot phase of the IGM (Narayanan et al. 2011; Savage et al. 2011; Tripp et al. 2011; Meiring et al. 2013; Hussain et al. 2015).

Our derived LLS coefficient, $N_0 = 0.25^{+0.13}_{-0.09}$, is consistent with previous values (Table 7) from low-resolution *HST* surveys with FOS and STIS. Our fit to pLLS redshift evolution over $0.24 < z < 0.84$ gives $\gamma_{\rm pLLS} = 1.14^{+0.88}_{-0.89}$, consistent with estimates noted above (Storrie-Lombardi et al. 1994; Stengler-Larrea et al. 1995; Ribaudo et al. 2011a). However, the *HST* surveys are all based on small numbers of LLSs with different redshift coverages. The median LLS redshifts are $z = 0.65$ for the seven FOS Key Project absorbers and $z = 0.39$ for the eight LLSs studied by COS. The Ribaudo et al. (2011a) survey was dominated by systems at $z > 1$, with only three LLSs at $z \leqslant 0.5$. Thus, the redshift evolution of LLSs and pLLSs remains uncertain. Our best fit, $\gamma_{\rm pLLS} = 1.14$, is similar to the value $\gamma_{\rm LF} = 1.24 \pm 0.06$ (Danforth et al. 2016) for weak Lyα forest absorbers and also to that, $\gamma_{\rm LLS} = 1.19 \pm 0.56$ (Ribaudo et al. 2011a), fitted to the LLS ($\tau_{\rm LLS} \geqslant 1$) absorbers at $z < 2.6$ in low-resolution FOS and STIS spectra. Differences in N_0 inferred from extrapolating $f(N, z)$ could be used to detect a turnover in the power-law slope (β) at log $N > 17$. However, the number of low-z LLS absorbers is currently too small to provide reliable statistics. Obviously, larger UV surveys of LLSs and pLLSs that cover a wider range of redshifts would have greater leverage for determining the evolution index γ.

Accurate values of pLLS/LLS evolution out to $z \approx 2$ are also important for assessing the far-UV opacity to intermediate-redshift AGNs, as we discuss in Section 3.5. The scarcity of strong absorbers (log $N_{\rm H\,I} > 16.5$) results in large fluctuations about these mean optical depths. However, the accumulated far-UV absorption from pLLSs could decrease F_λ and flatten the spectral energy distribution in the far-UV. There may also be bias in the selection of the intermediate-redshift quasars ($1.0 < z < 2.2$) used to construct rest-frame LyC composite spectra (Telfer et al. 2002; Shull et al. 2012b; Stevans et al. 2014; Tilton et al. 2016). To be selected, these AGNs needed to have detectable fluxes in the *GALEX* far-UV channel covering 1344–1786 Å (Morrissey et al. 2005). Thus, the observed AGN sight lines generally avoided encountering LLSs at $z_{\rm LLS} \approx 0.5$–1.0 with log $N_{\rm H\,I} > 17.5$ that block the far-UV absorption. How strongly this selection bias affects the intrinsic AGN composite spectrum is still unknown.

3.4. Damped Lyα Absorbers

Although we have focused primarily on pLLS and LLS absorbers, we also include a discussion of the four DLAs detected along the sight lines to all 159 AGNs in our sample. We provide these low-redshift statistics with only moderate

Table 6
Strong Absorbers (LLS and pLLS)[a]

No.	QSO Name	z_{abs}	z_{AGN}	log $N_{H\,I}$ Lehner+ 13	log $N_{H\,I}$ Stevans+ 14	log $N_{H\,I}$ This Paper
1	J092554.70+400414.1	0.2477	0.471139	19.55 ± 0.15	19.26 ± 0.06	19.45 ± 0.10
2	J020930.7–043826	0.39035	1.131	⋯	18.00 ± 0.2	18.5 ± 0.4
3	J151428.64+361957.9	0.41065	0.694596	⋯	17.93 ± 0.2	17.89 ± 0.06
4	J113327.78+032719.1	0.23756	0.525073	⋯	17.53 ± 0.10	17.29 ± 0.11
5	J100902.06+071343.8	0.35586	0.455631	18.40 ± 0.20	17.41 ± 0.04	18.3 ± 0.2
6	J100102.55+594414.3	0.30360	0.746236	⋯	17.27 ± 0.04	19.41 ± 0.12
7	J154553.48+093620.5	0.47379	0.665	⋯	17.25 ± 0.2	18.3 ± 0.2
8	J091029.75+101413.6	0.41924	0.463194	⋯	17.14 ± 0.8	$16.89^{+0.04}_{-0.11}$
9	SBS 1108+560	0.46334	0.76619	⋯	17.06 ± 0.1	17.85 ± 0.02
10	PG 1206+459	0.92772	1.16254	17.00 ± 0.10	17.03 ± 0.08	17.10 ± 0.10
11	PG 1630+377	0.27395	1.47607	16.98 ± 0.05	16.92 ± 0.04	17.04 ± 0.05
12	J100535.24+013445.7	0.41853	1.0809	⋯	16.37 ± 0.02	16.73 ± 0.10
13	J143511.53+360437.2	0.37292	0.428593	16.65 ± 0.07	16.72 ± 0.06	16.84 ± 0.06
14	J091029.75+101413.6	0.2634	0.463914	⋯	16.86 ± 0.5	16.21 ± 0.07
15	J161916.54+334238.4	0.47091	0.470946	⋯	16.84 ± 0.1	16.83 ± 0.10
16	J155048.29+400144.9	0.31257	0.496843	⋯	16.62 ± 0.06	16.3 ± 0.1
17	J155048.29+400144.9	0.4919	0.496843	⋯	16.57 ± 0.02	16.60 ± 0.05
18	PKS 0552–640	0.34513	0.680	16.90 ± 0.08	16.71 ± 0.03	17.01 ± 0.05
19	J124511.25+335610.1	0.55670	0.717	⋯	16.50 ± 0.2	16.28 ± 0.10
20	J124511.25+335610.1	0.68927	0.717	⋯	16.68 ± 0.2	16.70 ± 0.11
21	J100102.55+594414.3	0.41595	0.746236	⋯	16.61 ± 0.02	16.66 ± 0.08
22	HB89−0107−25	0.39913	0.956	⋯	16.59 ± 0.02	16.89 ± 0.06
23	J084349.49+411741.6	0.53255	0.989986	⋯	16.67 ± 0.05	16.85 ± 0.04
24	J100535.24+013445.7	0.83708	1.0809	⋯	16.81 ± 0.01	16.96 ± 0.08
25	PG 1522+101	0.72865	1.32785	16.66 ± 0.05	16.60 ± 0.09	16.62 ± 0.05
26	Q0232–042	0.73888	1.43737	16.72 ± 0.03	16.64 ± 0.08	16.76 ± 0.05
27	PG 1522+101	0.51839	1.32785	16.22 ± 0.02	16.32 ± 0.2	16.28 ± 0.05
28	PG 1338+416	0.68610	1.21422	16.45 ± 0.05	16.49 ± 0.04	16.49 ± 0.05
29	PG 1338+416	0.34885	1.2142	16.30 ± 0.13	16.37 ± 0.06	16.34 ± 0.10
30	PKS 0637–752	0.46850	0.653	16.48 ± 0.04	16.08 ± 0.03	16.48 ± 0.05
31	J141910.20+420746.9	0.28895	0.873501	16.40 ± 0.07	16.17 ± 0.03	16.17 ± 0.05
32	J141910.20+420746.9	0.42555	0.873501	16.17 ± 0.06	16.02 ± 0.02	16.24 ± 0.10
33	J141910.20+420746.9	0.53460	0.873501	16.34 ± 0.17	16.06 ± 0.07	16.15 ± 0.10
34	J143511.53+360437.2	0.38766	0.428593	16.18 ± 0.05	16.15 ± 0.02	16.17 ± 0.05
35	J094331.61+053131.4	0.35455	0.564336	16.11 ± 0.09	16.12 ± 0.09	16.12 ± 0.05
36	PG 1407+265	0.68270	0.946	16.38 ± 0.02	16.39 ± 0.03	16.38 ± 0.05
37	PG 1216+069	0.28231	0.3313	16.40 ± 0.05	16.29 ± 0.01	16.41 ± 0.03
38	J161916.54+334238.4	0.26938	0.470496	16.48 ± 0.05	16.40 ± 0.03	16.40 ± 0.08
39	SBS 1122+594	0.55810	0.852	16.24 ± 0.03	16.42 ± 0.02	16.45 ± 0.06
40	HE 0439–5254	0.61512	1.053	16.28 ± 0.04	16.25 ± 0.04	16.42 ± 0.10
73	J161649.42+415416.3	0.3211	0.440417	...	...	20.34 ± 0.12

Note.
[a] Strong absorbers estimated (Stevans et al. 2014) with log $N_{H\,I} \geqslant 16.5$ (systems #1–26) and log $N_{H\,I} = 16.0$–16.5 (systems #27–40). System #73 is a new DLA. Some were reported previously (Battisti et al. 2012; Fox et al. 2013; Lehner et al. 2013). Columns 3 and 4 list redshifts of absorber (z_{abs}) and AGN (z_{AGN}). Our column densities (this paper) are from the new CoG fits to Lyman-series approaching LL. Appendix A discusses CoGs and Ly decrements.

astronomical interpretation, because of the small numbers and the accompanying uncertainties in deriving effective path lengths. We compare our values with several previous DLA surveys that used UV data at $z < 1.65$ (Rao et al. 2006; Meiring et al. 2011; Battisti et al. 2012; Turnshek et al. 2015; Neeleman et al. 2016). Table 8 lists these four DLAs, together with six sub-DLAs (log $N_{H\,I} = 19.0$–20.3) and two strong absorbers (log $N_{H\,I} \approx 18.5 \pm 0.5$) whose large error bars place them near the sub-DLA range. As with our LLS statistics, we only consider redshifts $z_{abs} < 0.48$. Indeed, all four DLAs in our sample are at low redshifts ($z < 0.4$). Three were found serendipitously toward AGNs in the COS-Halos survey, which excluded QSOs with strong Mg II absorbers at $z > 0.4$. The fourth DLA ($z_{abs} = 0.185$) is toward B0120-28, a UV-bright QSO used to probe the Magellanic Stream. Because of the small numbers of low-redshift DLAs and the range of QSO targeting strategies, the statistics that follow are uncertain, as are those in other low-redshift surveys.

In our COS survey of 102 QSOs at $z \geqslant 0.24$, we had an effective path length $\Delta z = 19.24$ sensitive to detecting LLSs and DLAs in the range $0.24 < z < 0.48$. We include the extra path length ($\Delta z = 29.26$) at the redshifts in $0.01 < z < 0.24$ available to all 159 AGNs, and we subtract a small amount ($\Delta z = 0.282$) of LLS-blocked spectra. Thus, we have total redshift coverage $\Delta z \approx 48$ sensitive to DLAs. Our statistics for DLA frequency are therefore based on four low-redshift DLAs: J1619+3342 ($z_a = 0.0963$) with log $N_{H\,I} = 20.55 \pm 0.10$, J1009–0713 ($z_a = 0.1140$) with log $N_{H\,I} = 20.68 \pm 0.10$, B0120-28 ($z_a = 0.185$) with log $N_{H\,I} = 20.50 \pm 0.10$, and J1616+4153 ($z_a = 0.3211$) with log $N_{H\,I} = 20.60 \pm 0.20$.

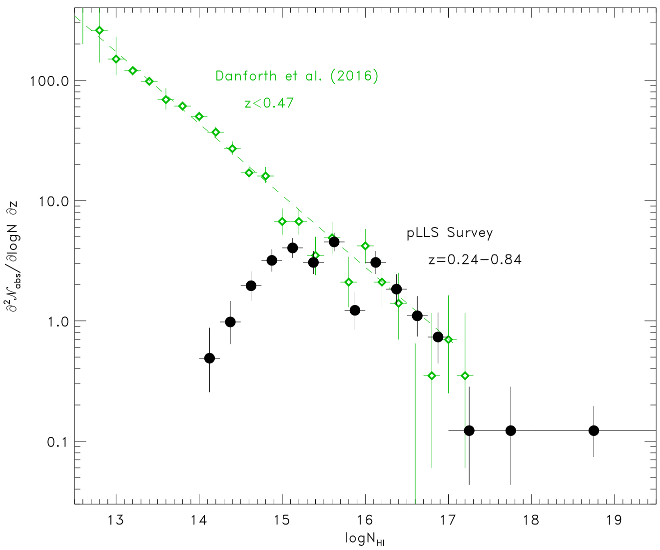

Figure 11. Distribution of H I absorbers in column density (per log $N_{\rm H\,I}$) over total redshift path length $\Delta z_{\rm eff} = 31.94$ in the range $0.24 \leqslant z \leqslant 0.84$. Solid diamonds (green) are from the *HST*/COS survey (Danforth et al. 2016) of the Lyα forest at $0 < z < 0.47$, and solid circles (black) show the current survey of pLLSs and LLSs at $0.24 < z < 0.84$. The green dotted line is a least-squares fit to the differential distribution, $f(N, z) \propto N^{-\beta}$, with $\beta = 1.60 \pm 0.02$.

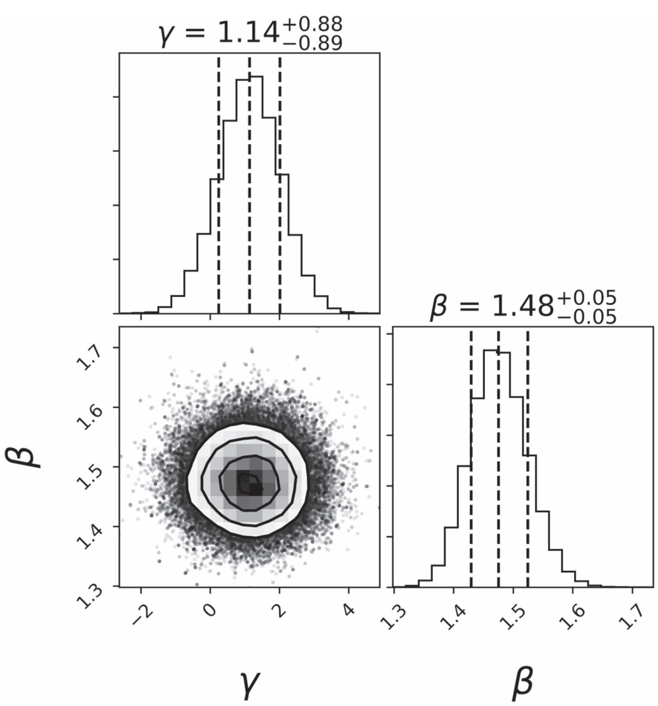

Figure 12. Parameterized evolution of the distribution of H I absorbers in column density and redshift, $f(N, z) = C_0 N^{-\beta}(1+z)^{\gamma}$, from MCMC samples for power-law parameters. The lower left panel plots the 2D joint probability of γ and β, and other panels show the marginalized distributions with median and 1σ bounds marked by dashed lines.

Over path length $\Delta z = 48$, these four DLAs correspond to a line frequency

$$\left(\frac{d\mathcal{N}}{dz}\right)_{\rm DLA} = 0.083^{+0.066}_{-0.040} \quad (4)$$

at mean redshift $\langle z \rangle = 0.18$. We now compare this DLA frequency to those inferred from other surveys at $z < 1.65$.

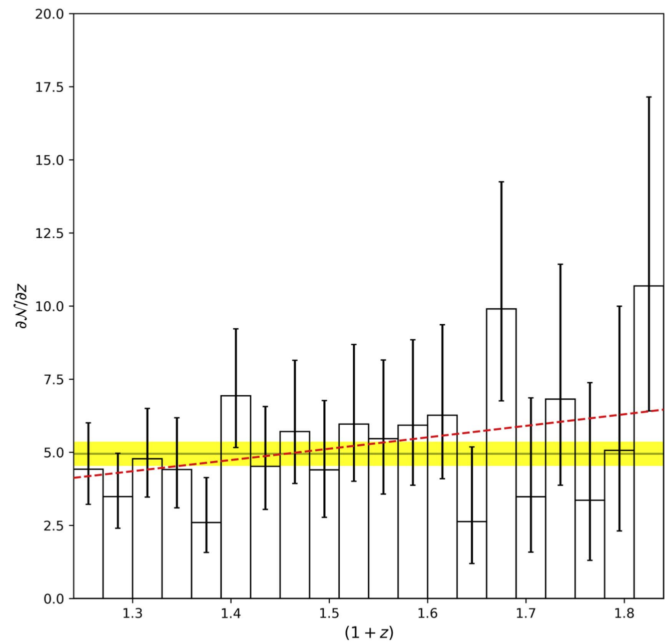

Figure 13. Parameterized evolution of the number of H I absorbers per unit redshift, $d\mathcal{N}/dz$, for $z = 0.24$–0.84, integrating $f(N, z) = C_0\, N^{-\beta}\quad(1+z)^{\gamma}$ over $15 \leqslant \log N_{\rm H\,I} \leqslant 20$. The MCMC realizations yield a fit with considerable uncertainty in index $\gamma = 1.14^{+0.88}_{-0.89}$. The horizontal (yellow) band shows the average line frequency, $\langle d\mathcal{N}/dz\rangle = 4.95 \pm 0.39$, and the red dashed line is the MCMC fit with $\gamma = 1.14$. The histogram shows the measured number of absorbers per unit redshift in 20 equal bins with error bars determined according to Poisson statistics. A noninteger number of absorbers may contribute to bin values because uncertainty in $N_{\rm H\,I}$ measurements can place a portion of an absorber's probability density outside the range used in the fit.

Owing to the small numbers of low-z DLAs, these surveys also have large uncertainties, ranging from $d\mathcal{N}/dz = 0.033^{+0.026}_{-0.015}$ (Neeleman et al. 2016) to $0.25^{+0.24}_{-0.14}$ (Meiring et al. 2011). Most of the DLAs in those surveys are at higher redshifts ($z > 1$) compared to the four DLAs in our COS survey ($z = 0.096$, 0.114, 0.185, and 0.321). As we now discuss, our value is generally consistent with these prior estimates.

Rao et al. (2006) used UV spectra from *HST*/STIS, identifying DLAs from a Mg II and Fe II selected sample. They found $d\mathcal{N}/dz = 0.079 \pm 0.019$ for DLAs at $z < 1.65$ based on 18 DLAs found in 108 Mg II systems at ($0.11 < z < 0.9$) with median redshift $z = 0.609$. Their fit to DLA evolution over all redshifts gave $n(z) = n_0(1+z)^{\gamma}$ with $n_0 = 0.044 \pm 0.005$ and $\gamma = 1.27 \pm 0.11$. Meiring et al. (2011) found $d\mathcal{N}/dz = 0.25^{+0.24}_{-0.14}$ from three DLAs along a COS-surveyed path with $\Delta z = 11.94$. These three DLAs were also identified in our survey: J1616+4153 ($z_a = 0.3211$), J1619+3342 ($z_a = 0.0963$), and J1009–0713 ($z_a = 0.1140$). Their much higher LLS absorber frequency was based on a smaller redshift path length, only 22% of that in our survey. Neeleman et al. (2016) conducted a large UV survey of 463 quasars at $z < 1.6$ over a significant path length ($\Delta z = 123.3$). They found a line frequency $d\mathcal{N}/dz = 0.033^{+0.026}_{-0.015}$ at median redshift $z = 0.623$. However, these statistics were based on just four DLAs with data from FOS, STIS, and COS. They originally had a total of 47 DLAs in their sample, but they excluded most of them in their statistics because they were found through Mg II targeting or because of a galaxy close to the QSO sight line.

Table 7
Summary of LLS Frequency Fitting[a]

Survey	Instrument	Redshift Range	N_0	γ	$N_{\rm LLS}$
This Paper	COS	0.24–0.48	$0.25^{+0.13}_{-0.09}$	1.14 ± 0.89	8
Storrie-Lombardi et al. 1994	FOS	0.40–4.69	$0.27^{+0.20}_{-0.13}$	1.55 ± 0.45	7
Stengler-Larrea et al. 1995	FOS	0.40–4.69	$0.25^{+0.17}_{-0.10}$	1.50 ± 0.39	7
Ribaudo et al. 2011a	FOS/STIS	0.25–2.59	0.28 ± 0.05	1.19 ± 0.56	17

Note.
[a] Redshift evolution of low-redshift LLSs (log $N_{\rm H\,I} \geqslant 17.2$) studied with UV spectra and fitted to $(d\mathcal{N}/dz) = N_0(1+z)^{\gamma}$. We include the current COS survey, two *HST* low-resolution surveys with FOS/G140L (Storrie-Lombardi et al. 1994; Stengler-Larrea et al. 1995), and a low-resolution survey with FOS/G140L and STIS/G140L/G230L (Ribaudo et al. 2011a). The last column gives the number $N_{\rm LLS}$ of low redshift ($z < 0.84$ LLSs in the COS survey, $z < 1.04$ in the FOS Key Project, and $z < 0.84$ in Ribaudo et al. 2011a). These surveys contain many more pLLSs, which are used in the fits.

In the most recent survey, Rao et al. (2017) examined the statistical properties of DLAs at $0.11 < z < 1.65$ using UV measurements (*HST*/ACS, *GALEX*, and *HST*/COS). Over a wide range of redshifts ($z = 0$–5), they fit $d\mathcal{N}/dz = (0.027 \pm 0.007)(1+z)^{1.682\pm0.200}$. This fit corresponds to $d\mathcal{N}/dz = 0.036$ at the mean redshift ($z = 0.18$) of our survey. They find no bias with Mg II-selected samples of DLAs. Their COS sample turned up no true DLAs (all had log $N_{\rm H\,I} \leqslant 20.0$), but two of them were sub-DLAs, also found in our survey (systems #1 and #6 in Appendix A).

3.5. Opacity of the Low-z IGM

After the epoch of reionization of neutral hydrogen at $z \approx 7$, the IGM becomes mostly ionized. However, the UV continuum of intermediate-redshift AGNs is still blanketed by Lyα absorbers that produce photoelectric opacity in their Lyman continua. This LyC opacity determines the mean free path of ionizing photons in the IGM, attenuates the ionizing photons from galaxies and quasars, and determines the metagalactic EUV background radiation (Fardal et al. 1998; Miralda-Escudé 2003; Haardt & Madau 2012; O'Meara et al. 2013). This continuum opacity is also relevant to measuring the composite spectrum of quasars in their rest-frame LyC. Our recent studies of AGNs at intermediate redshifts ($z \approx 1.5$–2.2) exhibit frequent pLLS absorption (Shull et al. 2012b; Stevans et al. 2014; Tilton et al. 2016) whose LyC optical depth and recovery at shorter wavelengths is used to restore the underlying AGN continuum.

The primary observable of our survey is the bivariate distribution of H I absorbers in redshift and column density. For a Poisson-distributed ensemble of H I absorbers (Paresce et al. 1984), one can compute the *average* photoelectric continuum opacity in the low-redshift IGM by integrating over the relevant range of column densities. We find the gradient of optical depth with redshift:

$$\frac{d\tau_{\rm eff}}{dz} = \int \left(\frac{d^2\mathcal{N}_{\rm abs}}{dz\ dN}\right) [1 - \exp\{-N\sigma(z)\}]\ dN\ . \qquad (5)$$

Here, N denotes $N_{\rm H\,I}$, and we define the H I photoelectric optical depth as $\tau(\lambda_o) = N\sigma\,(\lambda_0)$ at a typical *observed* far-UV wavelength, $\lambda_o \equiv \lambda_{\rm LL}\,(1+z_o)$. The Lyman continuum cross section is approximated as $\sigma(\lambda_o) \approx \sigma_0\ (\lambda_o/\lambda_{\rm LL})^3$ where $\sigma_0 = 6.30 \times 10^{-18}\ {\rm cm}^2$. We adopt a fiducial far-UV wavelength $\lambda_o = 1130$ Å where the COS/G130M coverage begins. By construction, $\lambda_o < \lambda_{\rm LL}\,(1+z)$ and $z_o < z$ in order for λ_o to lie in the LyC of the absorber.

We now compute the cumulative optical depth, $\tau_{\rm eff}\,(z_o,z)$, due to a population of H I absorbers at redshift z. For absorbers with $\tau_{\rm LL} < 1$ ($N < 1.59 \times 10^{17}\ {\rm cm}^{-2}$), we approximate $[1 - \exp(-\tau)] \approx \tau$. We express the H I column density distribution as separable power laws in column density and redshift,

$$f(N, z) \equiv \frac{d^2\mathcal{N}_{\rm abs}}{dz\ dN} = C_0 N^{-\beta}\,(1+z)^{\gamma}, \qquad (6)$$

for column densities N measured in cm^{-2}. In our pLLS survey, a maximum-likelihood fit finds $\beta_{\rm pLLS} = 1.48 \pm 0.05$, $\gamma_{\rm pLLS} = 1.14^{+0.88}_{-0.89}$, and $C_0 = 4 \times 10^7$ over the higher range in column density ($15 \leqslant \log N \leqslant 20$). The redshift gradient of LyC optical depth at observed wavelength λ_o depends on an integral over the column-density distribution:

$$\begin{aligned}\frac{d\tau_{\rm eff}(z_o, z)}{dz} &= C_0\ \sigma_0 \left[\frac{1+z_0}{1+z}\right]^3 (1+z)^{\gamma} \int_{N_1}^{N_2} N^{(-\beta+1)}\ dN \\ &= \frac{C_0\ \sigma_0\ (1+z)^{\gamma}}{(2-\beta)} \left[\frac{1+z_0}{1+z}\right]^3 [N_2^{(2-\beta)} - N_1^{(2-\beta)}].\end{aligned} \qquad (7)$$

For $\beta_{\rm pLLS} = 1.48 \pm 0.05$, the H I opacity is weakly dominated by the higher column density absorbers with $\tau_{\rm eff} \propto N_2^{0.52}$. Here, $\sigma(\lambda_o) \approx \sigma_0[(1+z_0)/(1+z)]^3$ is the cross section at wavelength λ_o. From the observed distribution parameters, we derive an opacity gradient $d\tau_{\rm eff}/dz = (0.408)(1+z)^{\gamma}_{\rm pLLS}[(1+z_0)/(1+z)]^3$ for the strong absorbers, $15 \leqslant \log N_{\rm H\,I} \leqslant 17.2$. We then integrate $\tau_{\rm eff}\,(z_o, z)$ from redshift z_o out to higher redshifts:

$$\begin{aligned}\tau_{\rm eff}^{\rm (pLLS)}(z_o, z) &= (0.396) \int_{z_o}^{z} \left[\frac{1+z_o}{1+z}\right]^3 (1+z)^{\gamma}\ dz \\ &= \frac{(0.396)(1+z_o)^{\gamma+1}}{(2-\gamma)} \left[1 - \left(\frac{1+z_o}{1+z}\right)^{(2-\gamma)}\right].\end{aligned} \qquad (8)$$

For our best-fitting index, $\gamma_{\rm pLLS} = 1.14$, the optical depths at $\lambda_o = 1130$ Å ($z_o = 0.24$) are $\tau_{\rm eff}\,(z_o, z) = (0.25, 0.33, 0.39)$ for sources at $z = (1.0, 1.5, 2.0)$. These opacities depend somewhat on the index $\gamma_{\rm pLLS}$. For $\gamma_{\rm pLLS} = 2$, the integral has a logarithmic dependence:

$$\tau_{\rm eff}^{\rm (pLLS)}(z_o, z) = (0.396)(1+z_o)^3 \ln\left[\frac{1+z}{1+z_o}\right]. \qquad (9)$$

Table 8
List of Strong (DLA and Sub-DLA) Absorbers[a]

AGN	z_{abs}	z_{AGN}	log $N_{H\,I}$ (cm^{-2})[b]	Comments
PG 1216+069	0.00635	0.331	19.32 ± 0.03	Sight line to System #37
J155304.92+354826.6	0.0830	0.721814	19.55 ± 0.15	Two other strong absorbers (log N = 15.18, 15.43)
J161916.54+334238.4	0.0963	0.470946	20.55 ± 0.10	Sight line to Systems #15 and #56 (Appendix A)
J100902.06+071343.8	0.1140	0.455631	20.68 ± 0.10	Sight line to System #5 (Appendix A)
J092837.98+602521.0	0.1538	0.29545	19.35 ± 0.15	No other strong absorbers with log N > 15.5
B0120-28	0.185	0.436018	20.50 ± 0.10	No other strong absorbers with log N > 15.5
J143511.53+360437.2	0.2026	0.428593	19.80 ± 0.10	Sight line to System #13 (Appendix A)
J1342-0053	0.22711	0.326	18.5 ± 0.5	Prochaska et al. (2017)
J092554.70+400414.1	0.2477	0.471139	19.45 ± 0.15	System #1 (Appendix A)
J100102.55+594414.3	0.30360	0.746236	19.41 ± 0.12	System #6 (Appendix A)
J161649.42+415416.3	0.3211	0.440417	20.34 ± 0.12	System #73 (Appendix A)
J0020930.7-043826	0.39043	1.131	18.5 ± 0.4	System #2 (Appendix A)

Notes.
[a] Four low-redshift damped Lyα (DLA) and six sub-DLA systems identified in our survey, ordered by absorber redshift (z_{abs}). The first eight absorbers lie below the minimum redshift ($z_{abs} = 0.24$) of our survey and are not included in our statistical analysis. DLA systems have log $N_{H\,I} > 20.3$, and sub-DLAs have 19.0 < log $N_{H\,I} < 20.3$. Two other absorbers have column densities log $N_{H\,I} = 18.5 \pm 0.5$, near the sub-DLA range.
[b] Column densities for several systems in this list were listed in other papers (Meiring et al. 2011; Tejos et al. 2014; Muzahid et al. 2015) with column densities determined by fitting damping wings of Lyα profile. For other absorbers (systems #1, 2, 6, 7, 73 in Appendix A), we use our own fits to Lyα damping wings, the LL decrement, and the CoG for higher Lyman lines.

At $z = (1.0, 1.5, 2.0)$, the corresponding optical depths are $\tau_{eff}(z_o, z) = (0.37, 0.55, 0.69)$. Because several LLS surveys have coverage to higher redshifts, it is possible that γ_{pLLS} could be higher than our assumed value of $\gamma = 1.14$. However, this best-fit index is similar to previous studies. For example, Ribaudo et al. (2011a) found $\gamma = 1.19 \pm 0.56$ for LLSs with $\tau_{LL} \geqslant 1$ over the range $0.25 < z < 2.59$. However, their survey only had three LLSs at $z \leqslant 0.5$ and 17 at $z \leqslant 0.84$.

Weaker lines in the Lyα forest, with log $N < 15$, contribute a smaller optical depth, $d\tau_{eff}/dz = (0.0674)(1+z)^{\gamma_{LF}}$, from which we find

$$\tau_{eff}^{(LF)}(z_o, z) = \frac{(0.0674)(1+z_o)^{\gamma+1}}{(2-\gamma)}\left[1 - \left(\frac{1+z_o}{1+z}\right)^{(2-\gamma)}\right]. \tag{10}$$

For the index, $\gamma_{LF} = 1.24 \pm 0.06$, that fits all absorbers at log $N_{H\,I} > 13.0$ (Danforth et al. 2016), the Lyα-forest optical depths at $\lambda_o = 1130$ Å ($z_o = 0.24$) are $\tau_{eff}(z_o, z) = 0.0453$, 0.0614, and 0.0727 for sources at $z = 1.0$, 1.5, and 2.0. Combining the pLLS and Lyα forest, we find average optical depths of $\tau_{eff}(z_o, z) = 0.29, 0.39, 0.46$ in the far-UV (1130 Å) corresponding to the Lyman edge redshifted to $z_o = 0.24$ and sources at $z = 1.0, 1.5, 2.0$.

4. Summary and Discussion

This *HST*/COS survey is one of the largest sets of 220 strong H I absorbers at low redshift. Our survey spans column densities ($14.0 \leqslant \log N_{H\,I} \leqslant 20.4$) and redshifts ($0.237 \leqslant z \leqslant 0.928$) sampled in bins of width $\Delta z = 0.04$ from $z = 0.24$–0.84 and $\Delta(\log N_{H\,I}) = 0.25$. With sensitivity to multiple lines in the H I Lyman series, our pLLS survey should be nearly complete for the 158 absorbers with log $N_{H\,I} > 15$. The column densities of a few absorbers in two bins (log $N_{H\,I} = 15.0$–15.5) may have shifted to adjoining bins owing to CoG effects of velocity components. We may also have missed some weak absorbers at $z > 0.5$, detected only in higher Lyman-series lines, since Lyα and Lyβ shift out of the COS/G160M window at $z > 0.47$ and $z > 0.75$, respectively. Our survey includes eight true LLSs (log $N_{H\,I} \geqslant 17.2$), one DLA (log $N_{H\,I} = 20.34 \pm 0.12$), and 54 pLLSs ($16.0 \leqslant \log N_{H\,I} < 17.2$). All absorbers were detected with the G130M and G160M gratings at a spectral resolution ($R \approx 17{,}000$ or $\Delta v \approx 18$ km s^{-1}) sufficient to measure multiple lines in the H I Lyman series, along with the Lyman decrement at log $N_{H\,I} \geqslant 16.2$. Our Lyman-comb technique is superior for column-density determinations compared to methods based on low-resolution ($R \approx 1000$) data. By combining the Lyman-series CoG with the Lyman decrement, we obtain reliable values of $N_{H\,I}$ and its bivariate distribution, $f(N_{H\,I}, z)$.

The COS distribution is in fairly good agreement with previous *HST* surveys of LLSs at $0.4 < z < 1.4$, with an absorber frequency per unit redshift parameterized as $d\mathcal{N}/dz = N_0(1+z)^{\gamma}$ and summarized in Table 7. Storrie-Lombardi et al. (1994) found $d\mathcal{N}/dz = (0.27)(1+z)^{1.55\pm0.45}$, and Stengler-Larrea et al. (1995) found $d\mathcal{N}/dz = (0.25)(1+z)^{1.50\pm0.39}$. Each of these FOS studies analyzed the same seven LLSs. From FOS and STIS data, Ribaudo et al. (2011a) fitted an index $\gamma = 1.19 \pm 0.56$ for LLS absorbers in the range $0.25 < z < 2.59$. The eight LLS systems in our COS survey are distinct from those in the FOS study and range from $z_{abs} = 0.2374$ to $z = 0.47379$ with median redshift $z_{abs} = 0.39$. Over total path length $\Delta z = 19.24$ in the range $0.24 < z < 0.48$, we find a mean frequency $\langle d\mathcal{N}/dz\rangle_{LLS} = 0.36^{+0.20}_{-0.13}$. With median redshift $z_{LLS} = 0.39$, this translates to $N(z) = N_0\,(1+z)^{\gamma}$, where $N_0 = 0.25^{+0.13}_{-0.09}$ at $z = 0$. An index $\gamma \approx 1.1$ is what one would expect for nonevolving pLLS absorbers at $z < 1$. For a ΛCDM cosmology with standard (Planck-2016) parameters, the expected redshift evolution for absorbers with constant space density ϕ_0 and cross section σ_0 is

$$\frac{d\mathcal{N}}{dz} = \left(\frac{\phi_0\,\sigma_0\,c}{H_0}\right)\frac{(1+z)^2}{[\Omega_m(1+z)^3 + \Omega_\Lambda]^{1/2}} \equiv \left(\frac{\phi_0\,\sigma_0\,c}{H_0}\right)S(z). \tag{11}$$

Over our sampled range in redshift, $0.24 \leqslant z \leqslant 0.84$, with $\Omega_m \approx 0.3$ and $\Omega_\Lambda \approx 0.7$, the cosmological factor is well fitted by $S(z) = (1.08)(1 + z)^{1.1}$ to 3% accuracy. Thus, our derived maximum-likelihood value $\gamma = 1.14^{+0.88}_{-0.89}$ is consistent with nonevolving absorbers, although the allowed range in γ provides a poor constraint on their low-z evolution. Ultraviolet spectroscopic surveys of pLLSs at $z = 0.7$–1.5, with better statistics and redshift leverage, would narrow the range of $\gamma_{\rm pLLS}$ and help to characterize their redshift evolution.

In the Introduction, we alluded to the relationship between LLS absorbers and the extended regions of galaxies. Using our statistical sample of pLLSs, with observed frequency $d\mathcal{N}/dz = 1.69 \pm 0.33$, Equation (11) implies a cross section, $\sigma_0 = \pi R_0^2$, with effective radius R_0 if we associate the pLLS with an appropriate space density of galaxies. We use the luminosity function of low-redshift ($z = 0.1$) galaxies from the Sloan Digital Sky Survey (Blanton et al. 2003), with normalization $\phi_* = (1.49 \pm 0.04) \times 10^{-2}\ h^3\,{\rm Mpc}^{-3}$ and faint-end slope $\alpha = -1.05 \pm 0.01$, to find

$$R_0 = \left[\frac{d\mathcal{N}dz}{\pi(c/H_0)\,\phi_*\,S(z)(\Delta L/L^*)}\right]^{1/2} \approx (110 \pm 10\ {\rm kpc})\ h^{-1}[S(z)(\Delta L/L^*)]^{-1/2}. \quad (12)$$

The cosmological factor $S(z) \approx 1.57$ at the median absorber redshift ($z = 0.39$). The fractional luminosity bandwidth $(\Delta L/L^*)$ depends on the minimum luminosity and ranges from 0.56 (integrating down to 0.5 L^*) to 1.83 (integrating down to 0.1 L^*). Both scaling factors enter as the square root. Taking $h \approx 0.7$ and recognizing the uncertainty in galactic parameters, we see that both LLS and pLLS have the correct absorber frequencies, $d\mathcal{N}/dz$, to be associated with extended halos of luminous (0.3–3.0 L^*) galaxies. In the COS-Halos Survey, the CGM of star-forming galaxies has been detected in O VI absorption (Tumlinson et al. 2011a, 2011b) out to distances of 100–150 kpc. Tumlinson et al. (2013) detected strong H I absorption averaging $\sim$1 Å in Lyα equivalent width out to 150 kpc, with 100% covering fraction for star-forming galaxies. Radial extents of 100–200 kpc are also consistent with the region of gravitational influence of $10^{12}\,M_\odot$ galaxies, estimated from a proper treatment of the virial radius (Shull 2014):

$$R_{\rm vir}(M_h, z_a) = (206\ {\rm kpc})\ h_{70}^{-2/3}\ M_{12}^{1/3}\left[\frac{\Omega_m(z_a)\,\Delta_{\rm vir}(z_a)}{200}\right]^{-1/3} \times (1 + z_a)^{-1}. \quad (13)$$

This expression differs from often-used formulae by the scaling with overdensity $\Delta_{\rm vir}$ and by the factor $(1 + z_{\rm a})^{-1}$. This factor reflects the fact that most galaxies underwent virialization in the past, when the IGM background density was higher by a factor of $(1 + z_a)^3$. Typical "half-mass assembly" redshifts are $z_a \approx 0.8$–1.2. After initial assembly, their proper size changes gradually because of continued mass infall into the halo. From the statistics of the current pLLS survey, we are unable to ascertain the H I column density at which "strong H I absorbers" are less directly associated with galaxy halos. Based on the steep falloff of the observed differential distribution, $f(N_{\rm H\,I}, z) \propto N_{\rm H\,I}^{-1.65}$, it likely occurs below $N_{\rm H\,I} = 10^{15}\ {\rm cm}^{-2}$. This prediction is consistent with observations (Figure 5 in Stocke et al. 2013) which find that virtually no absorbers with log $N_{\rm H\,I} \leqslant 14.5$ are within one virial radius of a galaxy of any luminosity. The issue of H I "covering factor" is difficult to constrain in our sample, since we have not undertaken a program to identify the associated galaxies. Many of them are at $z > 0.3$, and detecting them would be difficult.

The degree of pLLS/LLS evolution out to $z \approx 2$ is important for assessing the far-UV opacity to intermediate-redshift AGNs (Section 3.5). The scarcity of strong absorbers (log $N_{\rm H\,I} > 16.5$) results in large fluctuations about these mean optical depths. Far-UV absorption from pLLSs could decrease F_λ and flatten the spectral energy distribution in the far-UV. Selection bias may affect the intermediate-redshift quasars ($1.0 < z < 2.2$) used to construct rest-frame LyC composite spectra (Telfer et al. 2002; Shull et al. 2012b; Stevans et al. 2014; Tilton et al. 2016). These AGNs need to have detectable fluxes in the *GALEX* far-UV channel covering 1344–1786 Å (Morrissey et al. 2005). Thus, the observed AGN sight lines generally avoided encountering LLSs at $z_{\rm LLS} \approx 0.5$–1.0 with log $N_{\rm H\,I} > 17.5$ that block the far-UV absorption. How strongly this selection bias affects the intrinsic AGN composite spectrum is not yet understood.

We would benefit from larger FUV/NUV surveys of pLLS/LLS absorbers toward QSOs with $z_{\rm AGN} = 1$–2, with attention to biases introduced by target selection. This project will be difficult, since FUV-bright QSOs are needed to extend the absorber distribution, $f(N, z)$, to higher redshifts, and targeting via the presence or absence of strong Mg II absorbers will bias the LLS survey. The current COS survey provides reliable data at low redshift ($z < 0.5$), but connecting line frequency, $d\mathcal{N}/dz$, continuously to values at $z > 1.5$ (O'Meara et al. 2013) is critical for IGM radiative transfer models that rely on FUV opacities.

We now summarize the main results of our survey:

1. Over redshifts $0.24 \leqslant z \leqslant 0.84$, the average frequency for strong H I absorbers (log $N_{\rm H\,I} \geqslant 15.0$) is $\langle d\mathcal{N}/dz\rangle \approx 4.95 \pm 0.39$. We parameterize the bivariate distribution of H I absorbers as $f(N, z) = C_0 N_{\rm H\,I}^{-\beta}(1 + z)^\gamma$, where a maximum-likelihood fit over the ranges $0.24 \leqslant z \leqslant 0.84$ and $15 \leqslant \log N_{\rm H\,I} \leqslant 20$ gives $\beta \approx 1.48 \pm 0.05$, $\gamma \approx 1.14^{+0.88}_{-0.89}$, and $C_0 = 4 \times 10^7$ for column densities $N_{\rm H\,I}$ in cm^{-2}. This distribution is poorly determined at log $N_{\rm H\,I} > 17.5$. The redshift evolution ($\gamma \approx 1.1$) is consistent with absorbers of constant space density and cross section.
2. Based on seven true LLSs with log $N_{\rm H\,I} \geqslant 17.2$ in the range $0.24 < z < 0.48$, we derive an LLS frequency of $(d\mathcal{N}/dz)_{\rm LLS} = (0.25^{+0.13}_{-0.09})(1 + z)^\gamma$, assuming the best-fitting index $\gamma = 1.14$ derived from MCMC simulations of all strong absorbers. The frequency for pLLS is $(d\mathcal{N}/dz)_{\rm pLLS} = (1.69 \pm 0.33)(1 + z)^\gamma$. If these absorbers are associated with halos of luminous (0.3–3.0 L^*) galaxies, the pLLS frequency implies circumgalactic gas cross sections of 100–150 kpc radial extent.
3. Over the range ($0.01 < z < 0.48$) of the COS survey of 159 AGNs sensitive to DLAs, we found four DLAs over path length $\Delta z \approx 48$. From this, we estimate an absorber frequency, $(d\mathcal{N}/dz)_{\rm DLA} = 0.083^{+0.066}_{-0.040}$. Although uncertain, this frequency is lower than the previous (COS-studied) value, $0.25^{+0.24}_{-0.14}$ (Meiring et al. 2011), which was based on three DLAs over $\Delta z = 11.94$, but larger than the values $d\mathcal{N}/dz \approx 0.027$–0.036 (Neeleman et al. 2016;

Rao et al. 2017). All of these surveys suffer from small-number statistics.

4. Combining the data from low-redshift COS surveys of pLLS and Lyα forest absorbers, we estimate the H I photoelectric opacity gradient, $d\,\tau_{\rm eff}/dz$, for mean optical depth in the far-UV continuum (1130 Å). For indices $\gamma_{\rm pLLS} = 1.14$ and $\gamma_{\rm LF} = 1.24$, with considerable stochasticity, we estimate mean far-UV optical depths $\tau_{\rm eff}$ $(z_{\rm o}, z) = 0.29$, 0.39, and 0.46 for sources at $z = 1.0$, 1.5, and 2.0.
5. The observed distributions of strong H I absorbers are expected to have considerable variations among sight lines. Above $N_{\rm H\,I} = (10^{17}\ {\rm cm}^{-2})\ N_{17}$, the fitted cumulative frequency is small, $d\mathcal{N}(>N_{\rm H\,I})/dz = (0.577)\ N_{17}^{-0.48}$ $(1+z)^{\gamma}$. Our estimates of far-UV continuum opacity suggest that surveys of intermediate-redshift AGNs may have a selection bias toward sight lines with low optical depths, lacking strong LLS absorbers.

This survey was based on observations made with the NASA/ESA *Hubble Space Telescope*, obtained from the data archive at the Space Telescope Science Institute. STScI is operated by the Association of Universities for Research in Astronomy, Inc. under NASA contract NAS5-26555. The project originated from individual and survey observations of AGNs taken with the Cosmic Origins Spectrograph on the *Hubble Space Telescope*. We appreciate helpful discussions with Todd Tripp and David Turnshek. In early stages, this research was supported by grants HST-GO-13301.01.A and HST-GO-13302.01.A from the Space Telescope Science Institute to the University of Colorado Boulder. More recent work was carried out through academic support from the University of Colorado.

Appendix A
Notes on LLS and pLLS Absorbers

In this appendix, we discuss the column-density determinations for 73 strong H I absorbers ($\log N_{\rm H\,I} > 15.75$) at $z_{\rm abs} \geqslant 0.24$. In an approximate analysis used in our construction of an AGN composite spectrum (Stevans et al. 2014), the H I column densities of these systems were estimated and used to correct the underlying continuum. These estimates were based on automated CoG fitting, which becomes uncertain when the Lyman lines reach saturation (Table 2) and in the presence of multiple velocity components. In the current survey, we carefully examined each of these systems, combining multicomponent CoG fits with an analysis of the flux decrement at the Lyman limit. In fitting the continuum above and below the LL, we looked for contamination by broad AGN emission lines using the template shown in Figure 1. The underlying continuum lies below these emission lines. Systems labeled #1 through #26 (Table 6) had initial estimates $\log N_{\rm H\,I} \geqslant 16.5$, for which we expect a clear Lyman limit with optical depth $\tau_{\rm LL} \geqslant 0.2$. Systems #27 to #72 had estimated column densities $15.75 \leqslant \log N_{\rm H\,I} \leqslant 16.49$. System #73 is a DLA with $\log N_{\rm H\,I} = 20.34 \pm 0.12$ at $z_{\rm abs} = 0.3211$ not tabulated in Stevans et al. (2014). Some of these systems were discussed in previous papers (Ribaudo et al. 2011b; Tripp et al. 2011; Tumlinson et al. 2011b; Fox et al. 2013; Lehner et al. 2013; Tilton et al. 2016).

For the LLS and pLLS absorbers, our strategy of combining the CoG with LL flux decrements, when detected, provided confirmation of the column density and its uncertainty. In a number of cases involving multiple velocity components, we used the spectral resolution of G130M and G160M gratings to fit multicomponent CoGs. When the component separations were less than 100 km s^{-1}, we combined them into a single system. In a few instances with clearly separated components ($\Delta v > 150$–200 km s^{-1}), we kept separate track of the individual column densities and split them into separate absorbers, denoted systems #24abc, #47abc, #59ab, and #60ab. At the COS spectral resolution, the LL flux decrements and optical depths, $\tau_{\rm LL}$, typically arise from all components within 100–400 km s^{-1}. With good S/N in the higher-order Lyman lines, we are able to identify absorption systems with $\Delta v \geqslant$ 100 km s^{-1}. In comparing our column densities with prior work, we usually found good agreement ($\Delta \log N_{\rm H\,I} \leqslant 0.1$), but deviations are noted in the narratives and in the final column of Table 6. In our statistical analysis (Section 3 and Appendix B), we use our revised column densities and error bars.

#1: SDSS J092554.70+400414.1, $z_{\rm AGN} = 0.471139$, $z_{\rm abs} =$ 0.24770. See Figure 9. Because the COS observations for this sight line only covered wavelengths $\lambda > 1164$ Å, higher-order Lyman lines (above Lyϵ) and the Lyman edge are not accessible. However, Lyα shows a sub-DLA with damping wings that we fit with $\log N_{\rm H\,I} = 19.45 \pm 0.05$, a value slightly smaller than that ($\log N = 19.55 \pm 0.15$) quoted by Battisti et al. (2012), Meiring et al. (2013), and Lehner et al. (2013). Although our CoG solution for Lyα–Lyϵ gives a lower value ($\log N = 19.33 \pm 0.03$, $b = 37 \pm 5$ km s^{-1}), we adopt $\log N_{\rm H\,I} = 19.45 \pm 0.10$ and $b = 35 \pm 5$ km s^{-1} because the lower column density from the CoG does not reproduce the observed Lyα damping wings.

#2: FIRST J020930.7−043826, $z_{\rm AGN} = 1.13194$, $z_{\rm abs} =$ 0.39043. See Figure 9. The flux at $\lambda < 1270$ Å is consistent with zero (<1%) transmission in the Lyman continuum (optical depth $\tau_{\rm LL} > 4.6$ and $\log N_{\rm H\,I} > 17.86$). Lines above Ly12 suffer from crowding and are difficult to measure accurately. The CoG fit to Lyα–Ly12 constrains $\log N_{\rm H\,I}$ to the range 18.1–18.9 with $b = 45 \pm 5$ km s^{-1}, in agreement with the observed line profiles. In their Appendix A, Tejos et al. (2014) quoted $\log N_{\rm H\,I} = 18.87 \pm 0.03$ with $b = 34 \pm 1$ km s^{-1}. However, this error bar seems far too small, and we adopt $\log N_{\rm H\,I} = 18.5 \pm 0.4$.

#3: SDSS J151428.64+361957.9, $z_{\rm AGN} = 0.694596$, $z_{\rm abs} =$ 0.41065. See Figure 9. Low-quality data (S/N ~ 6 per resolution element) limit the accuracy of the Ly decrement method. The continuum has undulations (1300–1340 Å) arising from AGN emission lines of Ne VIII and O IV. From transmission shortward of the Ly edge, we find $\log N_{\rm H\,I} =$ 17.89 ± 0.06. The Lyman lines show a single component, with a CoG fit to Lyα–Ly12 giving $\log N_{\rm H\,I} = 18.04 \pm 0.20$ and $b = 43 \pm 2$ km s^{-1}. Two absorption components are seen in Si III in this system, not apparent in the H I lines. We adopt the decrement measurement, $\log N_{\rm H\,I} = 17.89 \pm 0.06$, and find that $b = 45 \pm 5$ km s^{-1} reproduces the observed line profiles.

#4: SDSS J113327.78+032719.1, $z_{\rm AGN} = 0.525073$, $z_{\rm abs} =$ 0.23740. See Figure 9. The initial redshift measurement of this system at $z = 0.2466$ (Stevans et al. 2014) placed it within our first redshift bin ($z_{\rm abs} = 0.24$–0.28). The higher Lyman lines ($n > 11$) lie blueward of the edge of the COS spectra, and no Ly decrement measurement is possible. A more careful examination of the data shows two absorbers at redshifts slightly below $z = 0.24$, and thus outside bin 1. Our CoG fits to

the red and blue components are inconsistent with the higher-order Lyman line profiles, suggesting the presence of additional components. We find qualitative agreement with the line profiles for Lyα–Ly10 using a three-component model: component 1 ($z_1 = 0.2374$) with log $N_1 = 17.2 \pm 0.1$, $b_1 = 35 \pm 5$ km s^{-1}; component 2 ($z_2 = 0.2378$) with log $N_2 = 15.8 \pm 0.1$, $b_2 = 25 \pm 5$ km s^{-1}; and component 3 ($z_3 = 0.2383$) with log $N_3 = 16.5 \pm 0.1$, $b_3 = 25 \pm 5$ km s^{-1}. The velocity separations are $\Delta v_{12} = 97$ km s^{-1} and $\Delta v_{23} = 121$ km s^{-1}. We adopt the summed total column density log $N_{\rm H\,I} = 17.29 \pm 0.11$.

#5: SDSS J100902.06+071343.8, $z_{\rm AGN} = 0.455631$, $z_{\rm abs} = 0.35586$. See Figure 9. The initial estimate of this system, log $N = 17.41 \pm 0.04$ (Stevans et al. 2014), underpredicts the Ly decrement significantly. The continuum at $\lambda < 1240$ Å is consistent with zero flux ($\tau_{\rm LL} > 5$, log $N > 17.9$), and the lower-order Lyman lines (Lyα–Ly6) are contaminated with other absorption. We adopt a CoG fit to Ly7–Ly12 with log $N_{\rm H\,I} = 18.3 \pm 0.2$ and $b = 37 \pm 2$ km s^{-1}, consistent with the decrement and providing a good match to the line profiles. This column is similar to the range (18.0–18.8) quoted by Tumlinson et al. (2011b) and the value (log $N_{\rm H\,I} = 18.4 \pm 0.2$) in Lehner et al. (2013). This sight line also contains a DLA (Meiring et al. 2011) at $z_{\rm abs} = 0.1140$ with log $N_{\rm H\,I} = 20.68 \pm 0.10$ (see Table 8).

#6: SDSS J100102.55+594414.3 (SBS 0957+599), $z_{\rm AGN} = 0.746236$, $z_{\rm abs} = 0.30355$. See Figure 9. The Stevans et al. (2014) CoG measurement of this system (log $N_{\rm H\,I} = 17.27 \pm 0.04$) significantly underpredicts the observed Lyman decrement. The continuum at $\lambda < 1194$ Å is consistent with zero flux ($\tau_{\rm LL} > 5$, log $N_{\rm H\,I} > 17.9$), and significant damping wings in the Lyα profile imply an even higher column density. Battisti et al. (2012) found log $N_{\rm H\,I} = 19.32 \pm 0.10$ by fitting the Lyα profile wings. We use a CoG fit to Lyα–Ly11, constrained by the requirement that log $N_{\rm H\,I} > 18$, to find log $N_{\rm H\,I} = 19.41 \pm 0.12$ and $b = 45 \pm 1$ km s^{-1}, consistent with both the line profiles and the Ly decrement.

#7: SDSS J154553.48+093620.5, $z_{\rm AGN} = 0.665$, $z_{\rm abs} = 0.47379$. See Figure 8. This absorber exhibits a strong Lyman decrement ($\tau_{\rm LL} > 5$), implying log $N_{\rm H\,I} > 17.9$. The transmitted flux shows no recovery from the LL ($\lambda_{\rm obs} = 1344$ Å) shortward to the end of the COS/G130M data ($\lambda_{\rm obs} \approx 1155$ Å), which requires log $N_{\rm H\,I} \geqslant 18.1$. A CoG fit to Ly$\beta$–Ly12 gives log $N = 17.67 \pm 0.15$, inconsistent with the Ly decrement. The Lyα absorption line lies redward of the end of the COS/FUV data, and we cannot use its damping wings as a measurement of column density. The redward wing of Lyβ limits log $N < 19.0$, but the CoG suggests log $N_{\rm H\,I} < 18.5$. The dominant absorption in metal lines (C II, Si II, and O VI) occurs at $z_1 = 0.4738$, with additional absorption 150 km s^{-1} redward ($z_2 = 0.4743$) seen in C II and O VI. However, this second component cannot explain the redward wing of Lyβ. We adopt a range 18.1 < log $N_{\rm H\,I} \leqslant 18.5$, treated statistically as log $N_{\rm H\,I} = 18.3 \pm 0.2$, and find that $b = 25$–35 km s^{-1} matches the line profiles.

#8: SDSS J091029.75+101413.6, $z_{\rm AGN} = 0.463194$, $z_{\rm abs} = 0.41924$. This AGN sight line also contains system #14 (see below). The low-S/N G130M data make line measurements somewhat uncertain. The UV continuum is contaminated by prominent AGN emission lines: O I (1355–1370 Å observed), C III λ977 (1430–1450 Å observed), and O VI λ1035 (1490–1520 Å observed). Fitting a continuum through line-free regions at 1390–1410 Å, 1460–1480 Å, and 1490–1520 Å, we find a Lyman decrement with $\tau_{\rm LL} = 0.49^{+0.05}_{-0.11}$ (log $N = 16.89^{+0.04}_{-0.11}$). A CoG fit gives log $N_{\rm H\,I} = 16.51 \pm 0.09$ with $b = 38 \pm 8$ km s^{-1}, inconsistent with the Ly decrement. We adopt the decrement value, with its asymmetric error bars, of log $N_{\rm H\,I} = 16.89^{+0.04}_{-0.11}$.

#9: SBS 1108+560, $z_{\rm AGN} = 0.766619$, $z_{\rm abs} = 0.46334$. See Figure 5. The CoG solution to this system (log $N \sim 17.1$) significantly underpredicts the flux in the Lyman continuum. The spectrum has high S/N, allowing us to estimate the Ly decrement to great precision. The transmitted continuum shortward of the Lyman edge lies *above* the interstellar absorption line of C II λ 1334.53; we also see Si II absorption lines at 1190 Å and 1193 Å. The transmitted flux in the Lyman continuum is $1.2 \pm 0.2\%$, implying optical depth $\tau_{\rm LL} = 4.42 \pm 0.15$ and our adopted value, log $N_{\rm H\,I} = 17.85 \pm 0.02$. With this column density, we find that $b = 18 \pm 2$ km s^{-1} provides a good match to the relatively narrow Lyman line profiles. A second, blue component visible in Lyϵ–Ly13 is fitted with a CoG having log $N_{\rm H\,I} = 15.9 \pm 0.05$ and $b = 20 \pm 5$ km s^{-1}. The combination of these two components, the weaker of which makes little contribution to the Ly decrement, fits the line profiles well.

#10: PG 1206+459, $z_{\rm AGN} = 1.16254$, $z_{\rm abs} = 0.92772$. See Figure 9. This high-redshift absorption system is observable by COS only in the higher Lyman lines (Ly6 and above). However, the high quality of the data and the Ly decrement allow accurate measurements for this pLLS (Tripp et al. 2011). Two components appear in the $n \geqslant 9$ Lyman lines. The optical depth, $\tau_{\rm LL} = 0.86 \pm 0.02$, implies a total column density log $N_{\rm tot} = 17.15 \pm 0.05$, but the allocation to the two components remains uncertain. Two components fit the profiles well ($\Delta v = 156$ km s^{-1}): component 1 (at $z_1 = 0.9270$) with log $N_1 = 16.95 \pm 0.05$, $b_1 = 28 \pm 5$ km s^{-1}; and component 2 (at $z_2 = 0.9280$) with log $N_2 = 16.3 \pm 0.1$, $b_2 = 25 \pm 5$ km s^{-1}. Their column densities sum to log $N_{\rm tot} = 17.04 \pm 0.06$ and account for the Ly decrement. In their study of this absorber, Tripp et al. (2011) fitted three clusters of nine velocity components, which they labeled Group A (log $N_{\rm A} = 15.74$), Group B (log $N_{\rm B} = 16.99$), and Group C (log $N_{\rm A} = 15.98$). Their summed column density (log $N_{\rm tot} = 17.05 \pm 0.11$) is 0.05 dex less than our adopted value, log $N_{\rm H\,I} = 17.10 \pm 0.10$, which is intermediate between our CoG and LL measurements.

#11: PG 1630+377, $z_{\rm AGN} = 1.47607$, $z_{\rm abs} = 0.27395$. See Figure 9. Our measurement of the Lyman decrement ($\tau_{\rm LL} = 0.69 \pm 0.04$) requires a total column density log $N = 17.04 \pm 0.05$, comparable to previously reported values of 17.06 ± 0.05 (Ribaudo et al. 2011b), 16.98 ± 0.05 (Lehner et al. 2013), and 16.92 ± 0.04 (Stevans et al. 2014). Higher-order lines (Ly7–Ly13) show two components ($\Delta v = 75$ km s^{-1}): a strong, blue component ($z_1 = 0.27395$, log $N_1 = 16.95 \pm 0.05$, $b_1 = 28 \pm 5$ km s^{-1}) and a weaker, red component ($z_2 = 0.27427$, log $N_2 = 16.3 \pm 0.1$, $b_2 = 25 \pm 5$ km s^{-1}). We adopt log $N_{\rm tot} = 17.04 \pm 0.05$.

#12: SDSS J100535.24+013445.7, $z_{\rm AGN} = 1.0809$, $z_{\rm abs} = 0.83711$. The Ly decrement from this absorber is determined by $N_{\rm H\,I}$ of both system #12 and #52 ($z = 0.83938$) located 370 km s^{-1} to the red. The LL optical depth was fitted to $\tau_{\rm LL} = 0.414 \pm 0.03$ (log $N_{\rm tot} = 16.82 \pm 0.04$). System #12 consists of two closely separated ($\Delta v = 77$ km s^{-1}) velocity components. CoG fits to the Lyman lines, where separable in Ly7–Ly13, give the following: component 1 ($z_1 = 0.83690$) with log $N_1 = 16.53 \pm 0.07$, $b_1 = 25 \pm 3$ km s^{-1}; and component 2 ($z_2 = 0.83737$) with log $N_2 = 16.31 \pm 0.09$,

$b_2 = 20 \pm 3\,\mathrm{km\,s^{-1}}$, summing to our adopted value log $N_{\mathrm{tot}} = 16.73 \pm 0.10$ for system #12. Including the (CoG-fitted) log $N_{\mathrm{H\,I}} = 16.09 \pm 0.05$ for system #52, we find log $N_{\mathrm{tot}} = 16.82 \pm 0.10$, consistent with the Ly decrement. Although system #12 is blended with system #52, we report them separately because they are easily separable ($\Delta v \approx 390\,\mathrm{km\,s^{-1}}$) in their Lyman line absorption.

#13: SDSS J143511.53+360437.2, $z_{\mathrm{AGN}} = 0.428593$, $z_{\mathrm{abs}} = 0.37297$. The AGN continuum appears to have broad O I emission features (1310–1335 Å observed frame). The observed decrement ($\tau_{\mathrm{LL}} = 0.42 \pm 0.05$) implies log $N_{\mathrm{H\,I}} \approx 16.82 \pm 0.05$. The CoG solution to Ly$\alpha$–Ly13, omitting Ly$\gamma$, Ly$\delta$, and Ly11, which are blended, gives a consistent (adopted) solution: log $N_{\mathrm{H\,I}} = 16.84 \pm 0.06$, $b = 19 \pm 1\,\mathrm{km\,s^{-1}}$. This sight line also contains a sub-DLA at $z_{\mathrm{abs}} = 0.2026$ with log $N_{\mathrm{H\,I}} = 19.80 \pm 0.10$ (see Table 7).

#14: SDSS J091029.75+101413.6, $z_{\mathrm{AGN}} = 0.463194$, $z_{\mathrm{abs}} = 0.26340$. See also system #8 above. Low-quality data (S/N ~ 2) and an undulating AGN continuum in the region of the Lyman limit make decrement measurements unreliable. However, the uncertain values, log $N_{\mathrm{H\,I}} = 16.86 \pm 0.5$ (Stevans et al. 2014) and $16.58^{+0.04}_{-0.07}$ (Prochaska et al. 2017), are not supported, as we detect no Ly decrement ($\tau_{\mathrm{LL}} < 0.1$). Our CoG fit to unblended lines of Lyβ, Lyγ, Lyϵ, and Ly6–Ly10 gives log $N_{\mathrm{H\,I}} = 16.21 \pm 0.07$, $b = 21 \pm 2\,\mathrm{km\,s^{-1}}$, consistent with the lack of a measurable Ly decrement.

#15: SDSS J161916.54+334238.4, $z_{\mathrm{AGN}} = 0.470946$, $z_{\mathrm{abs}} = 0.47088$. This absorber is offset by just $146\,\mathrm{km\,s^{-1}}$ blueward of the AGN systemic velocity. The LL lies on the red wing of a damped Lyα absorber profile at 1332.7 Å ($z_{\mathrm{DLA}} = 0.0963$) with log $N_{\mathrm{H\,I}} = 20.55 \pm 0.10$ (see Table 7). However, there is sufficiently recovered continuum in the blue wing of the DLA (1310–1320 Å) to measure an LL decrement with $\tau_{\mathrm{LL}} = 0.43 \pm 0.05$ and log $N_{\mathrm{H\,I}} = 16.83 \pm 0.05$. This solution fits the stronger Lyman lines (Lyα–Ly8) but increasingly overpredicts the higher-order absorption profiles ($n \geqslant 9$). We adopt log $N_{\mathrm{H\,I}} = 16.83 \pm 0.10$ and $b = 32 \pm 5\,\mathrm{km\,s^{-1}}$, noting unresolved structure in the system.

#16: SDSS J155048.29+400144.9, $z_{\mathrm{AGN}} = 0.496843$, $z_{\mathrm{abs}} = 0.31257$. This sight line has two strong absorbers (#16 and #17). The redshift of this absorber places the LL in the complicated region (1200–1220 Å) of the Galactic DLA and geocoronal N I and H I emission lines. The AGN continuum may be contaminated by broad O IV λ 788 emission (observed at 1170–1185 Å). The observed Ly decrement (1190–1197 Å) is uncertain ($\tau_{\mathrm{LL}} = 0.13 \pm 0.03$), implying log $N_{\mathrm{H\,I}} = 16.31 \pm 0.10$, a factor of 2 lower than that (16.62 ± 0.06) found by Stevans et al. (2014) from a CoG fit. Additional absorption is present in some of the higher-order Lyman lines ($n > 8$) that is not accounted for by this lower-N solution. This may have driven the previous CoG solution to a higher column density. We adopt log $N_{\mathrm{H\,I}} = 16.3 \pm 0.1$ and $b = 40 \pm 5\,\mathrm{km\,s^{-1}}$.

#17: SDSS J155048.29+400144.9, $z_{\mathrm{AGN}} = 0.496843$, $z_{\mathrm{abs}} = 0.49200$. The Lyman decrement ($\tau_{\mathrm{LL}} = 0.25 \pm 0.03$, log $N_{\mathrm{H\,I}} = 16.60 \pm 0.05$) is consistent with the Stevans et al. (2014) value, log $N_{\mathrm{H\,I}} = 16.57 \pm 0.05$. We adopt log $N_{\mathrm{H\,I}} = 16.60 \pm 0.05$ with $b = 25 \pm 5\,\mathrm{km\,s^{-1}}$.

#18: PKS 0552−640, $z_{\mathrm{AGN}} = 0.680$, $z_{\mathrm{abs}} = 0.34513$. See Figure 6. This system lies on the red edge of a damped Lyα profile (the Galactic DLA). However, the Lyman edge lies $\sim$10 Å redward of the line center, where the continuum has recovered from DLA absorption. The decrement ($\tau_{\mathrm{LL}} = 0.64 \pm 0.04$) requires log $N_{\mathrm{H\,I}} = 17.01 \pm 0.03$. The data are of very high quality (S/N ~ 25), and we are able to measure a single, narrow absorber in 24 lines (Lyα to Lyω). The highest-order lines ($n \geqslant 16$) are blended and not useful in CoG analysis, as noted in Table 2. A fit to Lyβ–Ly15 gives log $N_{\mathrm{H\,I}} = 17.01 \pm 0.05$, $b = 16 \pm 2\,\mathrm{km\,s^{-1}}$. This column density is above previous values, 16.90 ± 0.08 (Lehner et al. 2013) and 16.71 ± 0.03 (Stevans et al. 2014).

#19: SDSS J124511.25+335610.1, $z_{\mathrm{AGN}} = 0.711698$, $z_{\mathrm{abs}} = 0.5567$. This AGN sight line has three strong absorbers (systems #19, #20, and #46), which we fit simultaneously to set the continuum. The decrement for this system gives $\tau_{\mathrm{LL}} = 0.12 \pm 0.02$, although the local continua may be contaminated by AGN emission lines. The LL-inferred column density, log $N_{\mathrm{H\,I}} = 16.28 \pm 0.07$, is much smaller than the CoG fit, log $N_{\mathrm{H\,I}} = 16.63 \pm 0.09$, but additional absorption appears in the higher ($n > 8$) Lyman lines. We adopt log $N_{\mathrm{H\,I}} = 16.28 \pm 0.10$ based on the Ly decrement, with an increased error.

#20: SDSS J124511.25+335610.1, $z_{\mathrm{AGN}} = 0.711698$, $z_{\mathrm{abs}} = 0.68927$. As noted for system #19, we use a multi-component fit to set the continuum. The Lyman decrement ($\tau_{\mathrm{LL}} = 0.37 \pm 0.03$) implies log $N_{\mathrm{H\,I}} = 16.77 \pm 0.03$, somewhat larger than the value (16.68 ± 0.2) from Stevans et al. (2014). The local continua may be contaminated by AGN emission lines. A two-component profile is seen in the $n > 6$ lines. Our CoG fits two closely separated ($\Delta z = 75\,\mathrm{km\,s^{-1}}$) individual components in Ly6–Ly11: component 1 ($z_1 = 0.68894$) with log $N_1 = 16.57 \pm 0.10$, $b_1 = 22 \pm 3\,\mathrm{km\,s^{-1}}$; and component 2 ($z_2 = 0.68936$) with log $N_2 = 16.10 \pm 0.1$, $b_2 = 35 \pm 5\,\mathrm{km\,s^{-1}}$, summing to our adopted column density, log $N_{\mathrm{tot}} = 16.70 \pm 0.11$, similar to the observed decrement.

#21: SDSS J100102.55+594414.3 (SBS 0957+599), $z_{\mathrm{AGN}} = 0.746236$, $z_{\mathrm{abs}} = 0.41595$. The AGN continuum is contaminated by the prominent emission lines of Ne VIII (λ 770, 780) and O IV (λ 788) observed at 1320–1380 Å. Shortward of the Lyman edge, the flux level is contaminated by the prominent 700 Å lines of O III and N III (1220–1250 Å observed frame). The Ly decrement is somewhat uncertain because of this line emission and the continuum placement. Choosing continua redward and blueward of the LL to avoid these emission lines, our best fit gives $\tau_{\mathrm{LL}} = 0.29 \pm 0.04$ and log $N_{\mathrm{H\,I}} = 16.66 \pm 0.06$. Two closely separated ($\Delta v = 95\,\mathrm{km\,s^{-1}}$) components are apparent in Lyδ–Ly12 (geocoronal airglow is blended with Ly8–Ly10). The redder component is the stronger and dominates the LL decrement. We adopt $z_2 = 0.41560$, log $N_1 = 15.9 \pm 0.05$, $b_1 = 24 \pm 5\,\mathrm{km\,s^{-1}}$, and $z_2 = 0.41605$, log $N_2 = 16.45 \pm 0.05$, $b_2 = 35 \pm 5\,\mathrm{km\,s^{-1}}$, summing to log $N_{\mathrm{tot}} = 16.56 \pm 0.05$. Because of CoG uncertainties, we adopt the Ly decrement value with an increased error, log $N_{\mathrm{H\,I}} = 16.66 \pm 0.08$.

#22: HB89 0107−025-NED05, $z_{\mathrm{AGN}} = 0.956$, $z_{\mathrm{abs}} = 0.39909$. The continuum is well defined above the edge, despite a few AGN emission features (the 700 Å feature from O III and N III observed near 1370 Å). Our fit to the Lyman decrement ($\tau_{\mathrm{LL}} = 0.50 \pm 0.02$) implies log $N_{\mathrm{H\,I}} = 16.89 \pm 0.03$. A CoG fit to the system (Lyγ–Ly15) gives log $N_{\mathrm{H\,I}} = 16.77 \pm 0.06$ and $b = 25 \pm 2\,\mathrm{km\,s^{-1}}$. We adopt the Ly decrement solution with a wider error range, log $N_{\mathrm{H\,I}} = 16.89 \pm 0.06$.

#23: SDSS J084349.49+411741.6, $z_{\mathrm{AGN}} = 0.989986$, $z_{\mathrm{abs}} = 0.53255$. The LL optical depth, $\tau_{\mathrm{LL}} = 0.45 \pm 0.02$, implies log

$N_{\rm H\,I} = 16.85 \pm 0.02$. However, the decrement is determined by column densities of both systems #23 and #51 ($z = 0.53356$), located $198\ {\rm km\ s^{-1}}$ to the red. A two-component CoG to system #23 reproduces the line profiles well with log $N_{\rm H\,I} \approx 16.67 \pm 0.08$. Including log $N_{\rm H\,I} = 16.11 \pm 0.05$ for system #51 gives a total column density log $N_{\rm tot} = 16.78 \pm 0.07$. We adopt the Ly decrement value, but widen the error range to log $N_{\rm H\,I} = 16.85 \pm 0.04$.

#24: SDSS J100535.24+013445.7, $z_{\rm AGN} = 1.0809$, $z_{\rm abs} = 0.41865$. Three velocity components (denoted #24abc) contribute to the Ly decrement, with optical depth as $\tau_{\rm LL} = 0.58 \pm 0.04$ (log $N_{\rm H\,I} = 16.96 \pm 0.03$). Because the component splittings are easily separable, $\Delta v_{12} = 216\ {\rm km\ s^{-1}}$ and $\Delta v_{23} = 243\ {\rm km\ s^{-1}}$, we treat these as distinct absorbers, where we adopt component 1 ($z_1 = 0.41755$) with log $N_1 = 14.88 \pm 0.06$, $b_1 = 25 \pm 2\ {\rm km\ s^{-1}}$; component 2 ($z_2 = 0.41851$) with log $N_2 = 16.69 \pm 0.04$, $b_2 = 30 \pm 2\ {\rm km\ s^{-1}}$; and component 3 ($z_3 = 0.41966$) with log $N_3 = 15.91 \pm 0.08$, $b_3 = 22 \pm 2\ {\rm km\ s^{-1}}$, summing to log $N_{\rm tot} = 16.76 \pm 0.05$. The LL optical depth is reasonably consistent with this three-component CoG sum.

#25: PG 1522+101, $z_{\rm AGN} = 1.32785$, $z_{\rm abs} = 0.72865$. The decrement ($\tau_{\rm LL} = 0.26 \pm 0.03$) implies log $N_{\rm H\,I} = 16.62 \pm 0.05$, comparable to values ($16.66 \pm 0.05$ and 16.60 ± 0.04) reported by Lehner et al. (2013) and Stevans et al. (2014). Combined with our CoG fit to the higher Lyman lines, we adopt log $N_{\rm H\,I} = 16.62 \pm 0.05$ and $b = 29 \pm 5\ {\rm km\ s^{-1}}$.

#26: Q0232−042, $z_{\rm AGN} = 1.43737$, $z_{\rm abs} = 0.73888$. Our fit to the Ly decrement implies log $N_{\rm H\,I} = 16.77 \pm 0.02$, slightly stronger than the Stevans et al. (2014) CoG solution of 16.64 ± 0.08 and the value 16.72 ± 0.03 from Lehner et al. (2013). Including our CoG fit to the higher Lyman lines, we adopt log $N_{\rm H\,I} = 16.76 \pm 0.05$ and $b = 30 \pm 5\ {\rm km\ s^{-1}}$.

#27: PG 1522+101, $z_{\rm AGN} = 1.32785$, $z_{\rm abs} = 0.51839$. This is also known as PHL 1377. The AGN continuum appears contaminated by broad emission lines (O IV $\lambda608$ and O V λ 630). A weak Ly decrement is visible (log $N_{\rm H\,I} = 16.1$–16.3) with uncertain depth owing to AGN line emission. We performed CoG fits to two closely separated components ($\Delta v = 99\ {\rm km\ s^{-1}}$): component 1 ($z_1 = 0.5180$, log $N_1 = 15.64 \pm 0.04$, $b_1 = 15 \pm 1\ {\rm km\ s^{-1}}$) and component 2 ($z_2 = 0.5185$, log $N_2 = 16.17 \pm 0.04$, $b_2 = 17 \pm 1\ {\rm km\ s^{-1}}$), summing to log $N_{\rm tot} = 16.28 \pm 0.05$. This column density is somewhat larger than that (16.22 ± 0.02) quoted by Lehner et al. (2013) but is comparable to that (16.32 ± 0.2) in Stevans et al. (2014). We adopt our summed two-component CoG solution, log $N_{\rm tot} = 16.28 \pm 0.05$, with the error based on combining the CoG with the Ly decrement constraint.

#28: PG 1338+416, $z_{\rm AGN} = 1.21422$, $z_{\rm abs} = 0.68610$. This AGN sight line has three strong absorbers in our survey (#28, #29, and #53). The continuum is likely contaminated by an AGN broad emission feature of O III and N III near 700 Å (observed near 1550 Å). The fitted Ly decrement ($\tau_{\rm LL} = 0.188 \pm 0.030$) implies log $N_{\rm H\,I} = 16.47 \pm 0.07$, with the error bar arising from the uncertain placement of the continuum shortward of the LL. From CoG fitting, we adopt log $N_{\rm H\,I} = 16.49 \pm 0.05$ with $b = 20 \pm 5\ {\rm km\ s^{-1}}$, comparable to previous values of 16.45 ± 0.05 (Lehner et al. 2013), 16.49 ± 0.04 (Stevans et al. 2014), and 16.49 ± 0.04 (Tilton et al. 2016).

#29: PG 1338+416, $z_{\rm AGN} = 1.21422$, $z_{\rm abs} = 0.34885$. As noted for system #28, the AGN continuum is likely contaminated by AGN broad emission lines, in this case from O IV $\lambda554$ and Ne V $\lambda570$ observed at 1240–1260 Å. The Ly decrement ($\tau_{\rm LL} = 0.147 \pm 0.052$) implies log $N_{\rm H\,I} = 16.37 \pm 0.19$. The higher error arises from uncertain placement of the continuum shortward of the LL. We performed CoG fits to two components separated by $\Delta v = 76\ {\rm km\ s^{-1}}$: component 1 ($z_1 = 0.34855$, log $N_1 = 16.28 \pm 0.02$, $b_1 = 32 \pm 1\ {\rm km\ s^{-1}}$) and component 2 ($z_2 = 0.34889$, log $N_2 = 15.44 \pm 0.18$, $b_2 = 18 \pm 3\ {\rm km\ s^{-1}}$), summing to log $N_{\rm tot} = 16.34 \pm 0.05$. We adopt log $N_{\rm H\,I} = 16.34 \pm 0.10$, comparable to previous values of 16.30 ± 0.13 (Lehner et al. 2013) and 16.37 ± 0.06 (Stevans et al. 2014).

#30: PKS 0637−752, $z_{\rm AGN} = 0.653$, $z_{\rm abs} = 0.46850$. The fit to the Ly decrement implies log $N_{\rm H\,I} = 16.48 \pm 0.02$, but the placement of the continuum shortward of the LL is somewhat uncertain. Using CoG fitting of Lyβ–Ly17, we find log $N_{\rm H\,I} = 16.43 \pm 0.05$ and $b = 18 \pm 5\ {\rm km\ s^{-1}}$, a column density similar to the value of 16.48 ± 0.04 (Lehner et al. 2013) but higher than 16.08 ± 0.03 (Stevans et al. 2014). We adopt the Ly decrement value with a wider error, log $N_{\rm H\,I} = 16.48 \pm 0.05$.

#31: SDSS J141910.20+420746.9, $z_{\rm AGN} = 0.873501$, $z_{\rm abs} = 0.28895$. This AGN sight line has four strong absorbers in our survey (#31, #32, #33, and #50). The AGN continuum is contaminated by the 700 Å emission lines (O III and N III) observed at 1300–1320 Å. The Ly decrement is below the detectable level ($\tau_{\rm H\,I} < 0.1$, log $N_{\rm H\,I} < 16.20$). Using CoG fitting, we adopt log $N_{\rm H\,I} = 16.17 \pm 0.05$ with $b = 25 \pm 5\ {\rm km\ s^{-1}}$. This column is the same as quoted by Stevans et al. (2014) but below that (16.40 ± 0.07) quoted in Lehner et al. (2013), which would produce a larger Lyman decrement than observed.

#32: SDSS J141910.20+420746.9, $z_{\rm AGN} = 0.873501$, $z_{\rm abs} = 0.42555$. The continuum near the LL (1300 Å observed frame) is not flat, with no obvious decrement ($\tau_{\rm LL} < 0.15$ and log $N_{\rm H\,I} < 16.38$). This edge is contaminated by the 700 Å broad emission feature of O III and N III (observed at 1300–1315 Å). Using CoG fitting, we adopt log $N_{\rm H\,I} = 16.24 \pm 0.10$ and $b = 23 \pm 3\ {\rm km\ s^{-1}}$. This column density is slightly above previous values of 16.17 ± 0.06 (Lehner et al. 2013) and 16.02 ± 0.02 (Stevans et al. 2014).

#33: SDSS J141910.20+420746.9, $z_{\rm AGN} = 0.873501$, $z_{\rm abs} = 0.53460$. The continuum is contaminated by AGN emission lines of Ne VIII and O IV observed at 1445–1475 Å. We see no obvious Ly decrement ($\tau_{\rm LL} < 0.1$, log $N_{\rm H\,I} < 16.20$). Using CoG fitting, we adopt log $N_{\rm H\,I} = 16.15 \pm 0.10$ and $b = 16 \pm 2\ {\rm km\ s^{-1}}$, a column intermediate between values of 16.34(+0.23, −0.12) (Lehner et al. 2013) and 16.06 ± 0.07 (Stevans et al. 2014).

#34: SDSS J143511.53+360437.2, $z_{\rm AGN} = 0.428593$, $z_{\rm abs} = 0.38766$. We see a Ly decrement ($\tau_{\rm LL} = 0.10 \pm 0.03$, log $N_{\rm H\,I} = 16.20 \pm 0.12$) based on a small flux decrement at 1258–1265 Å. Prochaska et al. (2017) quote log $N_{\rm H\,I} < 16.65$ from low-resolution (COS/G140L) data. Using CoG fitting, we adopt log $N_{\rm H\,I} = 16.17 \pm 0.05$ and $b = 32 \pm 5\ {\rm km\ s^{-1}}$. This column density is similar to values of 16.18 ± 0.05 (Lehner et al. 2013) and 16.15 ± 0.02 (Stevans et al. 2014).

#35: SDSS J094331.61+053134.4, $z_{\rm AGN} = 0.564336$, $z_{\rm abs} = 0.35455$. Because of continuum undulations (1220–1240 Å), we cannot measure a reliable Ly decrement. CoG fitting gives values identical to those of Lehner et al. (2013) and

Stevans et al. (2014). We adopt log $N_{\rm H\,I} = 16.12 \pm 0.05$ with $b = 25 \pm 5$ km s^{-1} from CoG fitting.

#36: PG 1407+265, $z_{\rm AGN} = 0.946$, $z_{\rm abs} = 0.68270$. Based on high-quality data, we measure a Ly decrement, $\tau_{\rm LL} = 0.153 \pm 0.012$, implying log $N_{\rm H\,I} = 16.38 \pm 0.03$, comparable to previous values of 16.38 ± 0.02 (Lehner et al. 2013) and 16.39 ± 0.03 (Stevans et al. 2014). Including CoG fitting, we adopt log $N_{\rm H\,I} = 16.38 \pm 0.05$ with $b = 32 \pm 5$ km s^{-1}.

#37: PG 1216+069, $z_{\rm AGN} = 0.3313$, $z_{\rm abs} = 0.28231$. See Figure 7. Based on high-quality data, we measure a Ly decrement, $\tau_{\rm LL} = 0.16 \pm 0.02$, implying log $N_{\rm H\,I} = 16.40 \pm 0.06$. CoG fitting to Lye–Ly14 gives log $N_{\rm H\,I} = 16.41 \pm 0.03$ and $b = 25 \pm 2$ km s^{-1}, comparable to 16.40 ± 0.05 (Lehner et al. 2013).

#38: SDSS J161916.54+334238.4, $z_{\rm AGN} = 0.470946$, $z_{\rm abs} = 0.26938$. We see no obvious Ly decrement, but the wavelength calibration near the Lyman edge (1150–1165 Å) is uncertain. Using CoG fitting, we adopt log $N_{\rm H\,I} = 16.40 \pm 0.08$ and $b = 29 \pm 2$ km s^{-1}. This column density is similar to previous values 16.48 ± 0.05 (Lehner et al. 2013) and 16.40 ± 0.03 (Stevans et al. 2014).

#39: SBS 1122+594, $z_{\rm AGN} = 0.8514$, $z_{\rm abs} = 0.55810$. The AGN continuum near the Ly edge is uncertain, owing to broad emission lines of Ne VIII and O IV observed at 1440–1470 Å. Fitting a continuum below those emission features, we estimate a Ly decrement of $\tau_{\rm LL} = 0.18 \pm 0.04$ and log $N_{\rm H\,I} = 16.46 \pm 0.08$. We also fit a CoG with three velocity components separated by $\Delta v_{12} = 129$ km s^{-1} and $\Delta v_{23} = 58$ km s^{-1}: component 1 ($z_1 = 0.55748$) with log $N_1 = 15.79 \pm 0.05$, $b_1 = 27 \pm 3$ km s^{-1}; component 2 ($z_2 = 0.55815$) with log $N_2 = 16.13 \pm 0.05$, $b_2 = 21 \pm 2$ km s^{-1}; and component 3 ($z_3 = 0.55845$) with log $N_3 = 15.94 \pm 0.05$, $b_3 = 21 \pm 3$ km s^{-1}, summing to our adopted value, log $N_{\rm tot} = 16.45 \pm 0.06$ with $b = 29 \pm 2$ km s^{-1}. This column density is comparable to the value 16.42 ± 0.02 (Stevans et al. 2014) but above the value 16.24 ± 0.02 of Lehner et al. (2013). The Ly decrement is consistent with our higher value.

#40: HE 0439−5254, $z_{\rm AGN} = 1.053$, $z_{\rm abs} = 0.61512$. The AGN continuum below the LL is contaminated by the broad 700 Å emission lines of O III and N III observed at 1445–1455 Å. The continuum below the Ly edge ($\lambda < 1473$ Å) is therefore somewhat uncertain. From the Ly decrement, we estimate $\tau_{\rm LL} = 0.15 \pm 0.03$, implying log $N_{\rm H\,I} = 16.38 \pm 0.08$. We fit a CoG with three velocity components, separated by $\Delta v_{12} = 46$ km s^{-1} and $\Delta v_{23} = 89$ km s^{-1}: component 1 ($z_1 = 0.61495$) with log $N_1 = 16.2 \pm 0.1$, $b_1 = 18 \pm 2$ km s^{-1}; component 2 ($z_2 = 0.61520$) with log $N_2 = 15.8 \pm 0.1$, $b_2 = 60 \pm 10$ km s^{-1}; and component 3 ($z_3 = 0.61568$) with log $N_3 = 15.59 \pm 0.15$, $b_3 = 16 \pm 5$ km s^{-1}. Our adopted summed total, log $N_{\rm tot} = 16.42 \pm 0.10$, is higher than previous values of 16.28 ± 0.04 (Lehner et al. 2013) and 16.25 ± 0.04 (Stevans et al. 2014). We believe our three-component fitting is more accurate, with a summed column density consistent with the (less certain) Ly decrement.

#41: B0117−2837, $z_{\rm AGN} = 0.348858$, $z_{\rm abs} = 0.348330$. The AGN continuum is contaminated by broad emission features of O I (observed at 1265–1275 Å) and C III (observed at 1310–1320 Å) and by an absorption dip (1290–1300 Å). The flux shortward of the LL is complicated by the redward damping wing of Galactic Lyα absorption (1227–1232 Å). The Ly decrement is uncertain, $\tau_{\rm LL} = 0.16$–0.20 or log $N_{\rm H\,I} = 16.40$–16.50, and we place more weight on CoG fitting. We fit two closely separated ($\Delta v = 73$ km s^{-1}) absorbers at $z_1 = 0.34833$ (log $N_1 = 15.66 \pm 0.03$) and $z_2 = 0.34866$ (log $N_2 = 16.00 \pm 0.04$), summing to log $N_{\rm tot} = 16.14 \pm 0.04$, well below the estimated Ly decrement. Because of the continuum uncertainty with the Ly decrement, we adopt the summed CoG value, log $N_{\rm tot} = 16.16 \pm 0.10$, with an expanded error bar owing to contaminating AGN line emission.

#42: Ton 576 (SDSS J111754.31+263416.6), $z_{\rm AGN} = 0.420466$, $z_{\rm abs} = 0.35194$. This AGN has a well-defined continuum longward of the LL ($\lambda > 1232.6$ Å), but the flux recovery shortward of the Ly edge is complicated by damped Galactic Lyα absorption. Our fit to the redward wing of the Galactic DLA suggests $\tau_{\rm LL} = 0.14 \pm 0.03$ (log $N_{\rm H\,I} = 16.35 \pm 0.08$) for a flat continuum, but a downward-sloping continuum to shorter wavelengths gives log $N_{\rm H\,I} = 16.22 \pm 0.08$. The CoG from Stevans et al. (2014) gave 16.14 ± 0.02. Our new two-component ($\Delta v = 69$ km s^{-1}) CoG fit to Lyδ–Ly9 gives values of $z_1 = 0.35194$, log $N_1 = 15.89 \pm 0.09$ and $z_2 = 0.35225$, log $N_2 = 15.70 \pm 0.06$, summing to log $N_{\rm tot} = 16.11 \pm 0.10$. We adopt the summed CoG value, with a slightly larger error bar, log $N_{\rm H\,I} = 16.11 \pm 0.12$, reflecting the Ly decrement.

#43: SDSS J080908.13+461925.6, $z_{\rm AGN} = 0.656338$, $z_{\rm abs} = 0.61917$. The continuum is not well defined, owing to likely contamination by O I emission (1560–1570 Å observed frame). A weak Ly decrement suggests $\tau_{\rm LL} = 0.089 \pm 0.015$ or log $N_{\rm H\,I} = 16.15 \pm 0.07$. However, the continuum below the LL is uncertain. We adopt the value from CoG fitting: log $N_{\rm H\,I} = 16.18 \pm 0.07$ with $b = 36 \pm 2$ km s^{-1}.

#44: 3C 57, $z_{\rm AGN} = 0.670527$, $z_{\rm abs} = 0.32332$. Three velocity components are evident at $z_1 = 0.32257$, $z_2 = 0.32303$, and $z_3 = 0.32342$, with separations $\Delta v_{12} = 104$ km s^{-1} and $\Delta v_{23} = 88$ km s^{-1}. The Ly decrement falls in the Galactic DLA and is unobservable. Our new three-component CoG fit finds log $N_1 = 15.61 \pm 0.03$, log $N_2 = 15.45 \pm 0.03$, and log $N_3 = 16.12 \pm 0.09$, summing to log $N_{\rm tot} = 16.30 \pm 0.12$ and similar to the value 16.29 ± 0.01 (Stevans et al. 2014). We adopt a column density, log $N_{\rm H\,I} = 16.30 \pm 0.05$, consistent with both the CoG and Ly decrement.

#45: SDSS J113457.62+255527.9, $z_{\rm AGN} = 0.710078$, $z_{\rm abs} = 0.43233$. A new CoG fit gives log $N_{\rm H\,I} = 16.47 \pm 0.06$, whereas Stevans et al. (2014) quoted 16.40 ± 0.03. The continuum is fairly well defined, but portions may be contaminated by broad emission lines of Ne VIII and O IV observed at 1320–1350 Å. The Ly decrement implies $\tau_{\rm LL} = 0.19 \pm 0.020$ and log $N_{\rm H\,I} = 16.48 \pm 0.05$. With the CoG information, we adopt log $N_{\rm H\,I} = 16.48 \pm 0.06$.

#46: SDSS J124511.25+335610.1, $z_{\rm AGN} = 0.711698$, $z_{\rm abs} = 0.71297$. There are three strong absorbers in this sight line, including systems #19 and #20. Absorbers #20 and #46 have a complex flux recovery at 1540–1560 Å, as the envelope of higher Lyman lines from system #46 ($z = 0.71297$) merges with the LL of system #20 ($z = 0.68918$). Our fit to the Ly decrement gives log $N_{\rm H\,I} = 16.52 \pm 0.05$.

#47: SDSS J143726.14+504558.8, $z_{\rm AGN} = 0.783319$, $z_{\rm abs} = 0.77248$. The data quality is poor, and the continuum has likely contamination from AGN emission lines of O I observed at 1670–1690 Å and C III λ977 observed at 1740 Å. No Ly decrement is evident to a limit log $N_{\rm H\,I} < 16.6$. Because the component splittings are easily separable,

$\Delta v_{12} = 390$ km s^{-1} and $\Delta v_{23} = 230$ km s^{-1}, we treat these as distinct absorbers, denoted #47abc, where $z_1 = 0.76890$ (log $N_1 = 16.15 \pm 0.07$), $z_2 = 0.77120$ (log $N_2 = 15.4 \pm 0.2$), and $z_3 = 0.77255$ (log $N_3 = 16.26 \pm 0.10$). The middle component is poorly constrained, with a CoG based on only Lyγ, Lyδ, and Lyϵ. The summed CoG fit gives log $N_{\rm tot} = 16.26 \pm 0.11$ with $b = 40 \pm 6$ km s^{-1}.

#48: SDSS J234500.43−005936.0, $z_{\rm AGN} = 0.789429$, $z_{\rm abs} = 0.253900$. Because no data were taken at $\lambda < 1164$ Å, we cannot measure the Ly decrement (at 1143 Å). We rely on a two-component CoG solution, which gives log $N_1 = 15.85 \pm 0.10$ and $b_1 = 25 \pm 3$ km s^{-1} (blue component with Lyϵ and Lyζ) and log $N_2 = 15.77 \pm 0.16$, $b_1 = 41 \pm 12$ km s^{-1} (red component with Lyβ to Lyζ). These column densities sum to log $N_{\rm tot} = 16.11 \pm 0.13$.

#49: SDSS J101622.60+470643.3, $z_{\rm AGN} = 0.821527$, $z_{\rm abs} = 0.72766$. No clear Ly decrement is seen (log $N_{\rm H\,I} < 16.34$). The continuum is uncertain longward of the LL because of AGN emission lines. Our CoG fit uses Lyβ to Ly10 to find log $N_{\rm H\,I} = 16.16 \pm 0.09$ with $b = 19 \pm 2$ km s^{-1}.

#50: SDSS J141910.20+420746.9, $z_{\rm AGN} = 0.873501$, $z_{\rm abs} = 0.84523$. A weak Ly decrement may be present with log $N_{\rm H\,I} = 16.23 \pm 0.15$, with an uncertain continuum redward of the edge owing to O I emission lines observed at 1770–1790 Å. We fit a CoG to Lyδ up to Ly10, with our adopted value log $N_{\rm H\,I} = 16.23 \pm 0.05$ and $b = 29 \pm 2$ km s^{-1}.

#51: SDSS J084349.49+411741.6, $z_{\rm AGN} = 0.989986$, $z_{\rm abs} = 0.53556$. The source has a well-defined continuum, with a Ly decrement suggesting $\tau_{\rm LL} = 0.41 \pm 0.02$ or log $N_{\rm H\,I} = 16.81 \pm 0.02$ for a flat continuum. This decrement includes both systems #23 and #51. However, system #23 at $z = 0.53255$ is easily separable in the Lyman lines, lying 178 km s^{-1} blueward. These absorbers are visible in blended Lyman lines (Lyγ, Lyδ, Lyϵ) at redshifts $z_1 = 0.53255$ for system #23 (log $N_1 = 16.67 \pm 0.05$) and $z_2 = 0.5355$ for system #51 (log $N_2 = 16.11 \pm 0.05$). Their column densities sum to log $N_{\rm H\,I} = 16.78 \pm 0.05$, consistent with the decrement. In our statistics, we treat systems #23 and #51 as distinct absorbers, since they are easily separable in the Lyman absorption lines.

#52: SDSS J100535.24+013445.7, $z_{\rm AGN} = 1.0809$, $z_{\rm abs} = 0.83938$. The source has a well-defined continuum, with LL optical depth $\tau_{\rm LL} = 0.41 \pm 0.03$ (log $N_{\rm tot} = 16.82 \pm 0.04$) produced by absorption from system #12 at $z_1 = 0.83711$ and system #52 at $z_2 = 0.83938$. These two systems are easily distinguished, separated by $\Delta v \approx 390$ km s^{-1} in the Lyman lines (Lyγ, Lyδ, Lyϵ). Our CoG gives log $N_{\rm H\,I} = 16.09 \pm 0.05$ for system #52. The combined column densities of #12 and #52 are consistent with the Ly decrement.

#53: PG 1338+416, $z_{\rm AGN} = 1.21422$, $z_{\rm abs} = 0.62075$. This AGN sight line has three absorbers with Lyman edges near 1537 Å (system #28), 1478 Å (system #53), and 1225 Å (system #29). The continuum at 1540–1580 Å is contaminated by broad emission lines of O II and O III (rest frame 833–834 Å). For this system, the weak Ly decrement at 1478 Å is poorly determined. CoG fitting gives log $N_{\rm H\,I} = 16.17 \pm 0.06$ for #53, consistent with that found by Tilton et al. (2016).

#54: Q 0232−042, $z_{\rm AGN} = 1.43747$, $z_{\rm abs} = 0.322450$. This AGN is also known as PHL 1377 (see also system #26). No Lyman decrement is evident. Our CoG fit gives log $N_{\rm H\,I} = 16.14 \pm 0.04$ with $b = 34 \pm 2$ km s^{-1}.

#55: PG 0003+158, $z_{\rm AGN} = 0.4509$, $z_{\rm abs} = 0.3478$. The data have high S/N, and a Lyman series is evident up to Ly12 with higher lines intruding on the red wing of the Galactic DLA. We use the excellent CoG fit with log $N_{\rm H\,I} = 16.10 \pm 0.03$ with $b = 17 \pm 1$ km s^{-1}, consistent with a weak LL flux decrement.

#56: SDSS J161916.54+334238.4, $z_{\rm AGN} = 0.470946$, $z_{\rm abs} = 0.44231$. This AGN also contains system #15 (Lyman edge at 1341 Å) and a DLA at 1333 Å ($z_{\rm abs} = 0.0963$; see Table 7). This DLA blocks the LL of system #56 as well as lines of Ly7–Ly9. A good CoG fit using Lyα to Ly6 plus Ly10 and Ly11 yields log $N_{\rm H\,I} = 15.90 \pm 0.06$ with $b = 26 \pm 2$ km s^{-1}.

#57: PG 0637−752, $z_{\rm AGN} = 0.653$, $z_{\rm abs} = 0.24326$. The LL at 1133.5 Å falls just below the COS/G130M data range, and a blueward continuum is not visible. However, a CoG fit to Lyγ, Lyϵ, Ly8, and Ly10 gives log $N_{\rm H\,I} = 15.81 \pm 0.05$ with $b = 22 \pm 2$ km s^{-1}.

#58: PKS 0552−640, $z_{\rm AGN} = 0.68$, $z_{\rm abs} = 0.446$. A CoG fit to Lyβ through Ly14 gives a very good fit with log $N_{\rm H\,I} = 15.96 \pm 0.02$ and $b = 28 \pm 1$ km s^{-1}. This column density is consistent with a weak LL decrement visible in very good data.

#59: SDSS J124511.25+335610.1, $z_{\rm AGN} = 0.717$, $z_{\rm abs} = 0.63215$. The data quality is poor, with no obvious Ly decrement. A double-component structure is seen in Lyβ through Ly8, easily separable as components denoted #59ab. A two-component CoG gives a reasonable fit, with $z_1 = 0.63190$ (log $N_1 = 15.83 \pm 0.10$, $b_1 = 17 \pm 1$ km s^{-1}) and $z_2 = 0.63245$ (log $N_2 = 15.80 \pm 0.06$, $b_2 = 36 \pm 2$ km s^{-1}), summing to log $N_{\rm H\,I} = 16.12 \pm 0.10$.

#60: SBS 1108+560, $z_{\rm AGN} = 0.766619$, $z_{\rm abs} = 0.28646$. This sight line has a very strong LLS (system #9) to the red of absorber #60. In the low-flux region blueward of #9, we see two strong velocity components (separation $\Delta v = 233$ km s^{-1}) in Lyα through Ly9, with considerable blending from other absorption. Because the components are easily separable, we treat these as distinct absorbers, denoted #60ab. Individual CoG fits to these features give $z_1 = 0.2855$ (log $N_1 = 16.12 \pm 0.09$, $b_1 = 34 \pm 2$ km s^{-1}) and $z_2 = 0.2865$ (log $N_2 = 16.14 \pm 0.07$, $b_2 = 57 \pm 3$ km s^{-1}), summing to log $N_{\rm H\,I} = 16.43 \pm 0.08$. The implied $\tau_{\rm LL} = 0.17$ is difficult to confirm, given the poor data at 1173 Å and the likely presence of AGN broad emission lines of O III and N III (1150–1170 Å observed frame).

#61: SDSS J143726.14+504555.8, $z_{\rm AGN} = 0.783319$, $z_{\rm abs} = 0.250650$. The LL at 1140 Å is barely within the COS/G130M data range. The data are quite noisy, and several Lyman lines are blocked (Lyγ) or contaminated by other absorption (Ly7). A CoG fit with log $N_{\rm H\,I} = 16.27 \pm 0.08$ and $b = 24 \pm 2$ km s^{-1} implies a Ly decrement with $\tau_{\rm LL} = 0.12$ that is hard to confirm. However, this column density overpredicts the line profiles of Ly8, Ly9, and Ly10. We widen the error and adopt log $N_{\rm H\,I} = 16.27 \pm 0.12$.

#62: SDSS J234500.43−005936.0, $z_{\rm AGN} = 0.789429$, $z_{\rm abs} = 0.54818$. The data quality is quite good, with no LL decrement visible at 1411.6 Å. We see hints of two velocity components ($\Delta v \approx 40$ km s^{-1}) with extra absorption in asymmetric red wings of Lyϵ through Ly10. A two-component CoG gives log $N_1 = 15.63 \pm 0.07$ and log $N_2 = 16.10 \pm 0.17$, summing to 16.23. We adopt a single-component CoG to Lyβ through Ly12, which gives log $N_{\rm H\,I} = 16.16 \pm 0.06$ and $b = 26 \pm 2$ km s^{-1}.

#63: SDSS J101622.60+470643.3, $z_{\rm AGN} = 0.821527$, $z_{\rm abs} = 0.66475$. This sight line includes system #49 ($z_{\rm abs} = 0.727$). The continuum longward of the LL (1520–1540 Å) may be contaminated by AGN emission lines (O II and O III at

833–834 Å rest frame). A CoG fit to Lyβ through Ly9 gives log $N_{\rm H\,I} = 15.99 \pm 0.03$ with $b = 28 \pm 1$ km s^{-1}.

#64: SBS 1122+594, $z_{\rm AGN} = 0.8514$, $z_{\rm abs} = 0.67835$. This sight line also includes system #39 ($z_{\rm abs} = 0.5581$). The data quality is high, with a well-constrained CoG fit: log $N_{\rm H\,I} = 16.06 \pm 0.04$ and $b = 19 \pm 1$ km s^{-1}. The observed weak Ly decrement is consistent with this column density.

#65: SDSS J141910.20+420746.0, $z_{\rm AGN} = 0.873501$, $z_{\rm abs} = 0.52221$. This sight line also includes systems #31, #32, #33, #50, and #66. Systems #31 and #32 are at much lower redshifts, and system #50 is at a much higher redshift ($z = 0.84523$). System #33 has a somewhat higher redshift ($z = 0.53460$) but is widely separated ($\Delta v = 2440$ km s^{-1}). The data quality is not good, and no Ly decrement is apparent. A CoG fit to Lyβ, Lyγ, Lyδ, Lyϵ, and Ly7 gives log $N_{\rm H\,I} = 15.87 \pm 0.07$ with $b = 37 \pm 2$ km s^{-1}.

#66: SDSS J141910.20+420746.0, $z_{\rm AGN} = 0.873501$, $z_{\rm abs} = 0.80463$. This sight line also includes systems #31, #32, #33, #50, and #66. Systems #31 and #32 are at much lower redshifts, and system #50 is at somewhat higher redshift ($z = 0.84523$), although it produces no visible Ly decrement at the location of system #66 (1645.4 Å). The Lyγ line is strong, and lines of Lyδ to Lyζ show two velocity components ($\Delta v = 66$ km s^{-1}), which we fit with CoGs to find $z_1 = 0.8044$ (log $N_1 = 15.71 \pm 0.22$, $b_1 = 16 \pm 3$ km s^{-1}) and $z_2 = 0.8047$ (log $N_2 = 15.75 \pm 0.06$, $b_2 = 19 \pm 2$ km s^{-1}), summing to log $N_{\rm H\,I} = 16.03 \pm 0.15$.

#67: FBQS J0751+2919, $z_{\rm AGN} = 0.915$, $z_{\rm abs} = 0.82902$. The data are of very high quality with a weak Ly decrement. A CoG fit to Lyδ through Ly12 gives log $N_{\rm H\,I} = 16.06 \pm 0.02$ with $b = 34 \pm 2$ km s^{-1}.

#68: PG 1407+265, $z_{\rm AGN} = 0.946$, $z_{\rm abs} = 0.59964$. The data are of very high quality, but no Ly decrement is visible. A CoG fit to Lyγ through Ly12 gives log $N_{\rm H\,I} = 16.08 \pm 0.04$ with $b = 14 \pm 1$ km s^{-1}.

#69: LBQS 0107−0235, $z_{\rm AGN} = 0.957039$, $z_{\rm abs} = 0.536$. The data are of very high quality, but no Ly decrement is visible. Two broad, well-separated absorption components ($\Delta v = 142$ km s^{-1}) are seen in Lyβ through Lyϵ, with the stronger (redder) component visible up to Ly10. A two-component CoG fit finds $z_1 = 0.53572$ (log $N_1 = 15.42 \pm 0.05$, $b_1 = 40 \pm 9$ km s^{-1}) and $z_2 = 0.53645$ (log $N_2 = 15.66 \pm 0.05$, $b_2 = 40 \pm 7$ km s^{-1}), summing to log $N_{\rm H\,I} = 15.86 \pm 0.05$.

#70: LBQS 0107−0235, $z_{\rm AGN} = 0.957039$, $z_{\rm abs} = 0.87636$. A very weak Ly decrement may be present, consistent with log $N_{\rm H\,I} < 16.1$. A CoG fit to Lyδ through Ly12 gives log $N_{\rm H\,I} = 15.96 \pm 0.04$ with $b = 30 \pm 5$ km s^{-1}.

#71: PG 1522+101, $z_{\rm AGN} = 1.32785$, $z_{\rm abs} = 0.67518$. This sight line also includes system #25 ($z = 0.72865$), which produces a Ly decrement at 1576 Å redward of systems #71 and #27 ($z = 0.51839$). System #71 consists of two absorption components, separated by $\Delta v \approx 72$ km s^{-1}, which we fit with $z_1 = 0.6748$ (log $N_1 = 15.39 \pm 0.05$, $b_1 = 27 \pm 2$ km s^{-1}) and $z_2 = 0.6752$ (log $N_2 = 15.71 \pm 0.04$, $b_2 = 42 \pm 4$ km s^{-1}), summing to log $N_{\rm H\,I} = 15.88 \pm 0.05$.

#72: PG 1630+377, $z_{\rm AGN} = 1.47607$, $z_{\rm abs} = 0.91449$. Owing to its high redshift (for this survey), the COS spectra show absorption in Lyϵ through Ly10, but no Ly decrement is visible. There appear to be two velocity components ($\Delta v = 66$ km s^{-1}) with a stronger blue component ($z_1 = 0.9143$, log $N_{\rm H\,I} = 15.67 \pm 0.04$), but a poorly constrained Doppler parameter, $b = 99 \pm 49$ km s^{-1}. A weaker red component at $z_2 = 0.9148$ is only reliably detected in Lyϵ through Ly7, with a poorly constrained column density, log $N_{\rm H\,I} = 15.4 \pm 0.2$. The total system has log $N_{\rm H\,I} = 15.86 \pm 0.10$,

#73: SDSS 161649.42+415416.3, $z_{\rm AGN} = 0.440417$, $z_{\rm abs} = 0.3211$. This DLA did not appear in the Stevans et al. (2014) list, but we found it in our new examination through its Lyman edge at 1204.5 Å. Meiring et al. (2011) and Battisti et al. (2012) quote log $N_{\rm H\,I} = 20.60 \pm 0.20$ from fitting the Lyα damping wings. Our CoG fit to Lyβ and Lyδ–Ly8 yields a somewhat smaller column density, log $N_{\rm H\,I} = 20.34 \pm 0.12$ with $b = 49 \pm 2$ km s^{-1}. Stevans et al. (2014) listed no other strong H I absorbers in this sight line with log $N_{\rm H\,I} > 15.5$.

Appendix B
Maximum-likelihood Fitting of the pLLS Distribution

Following the convention in studies of quasar absorption lines (Weymann et al. 1998; Kim et al. 2002, among many others), we express the column density distribution as separable power laws in column density, N, and redshift, z:

$$f(N, z) \equiv \frac{d^2\mathcal{N}_{\rm abs}}{dz\, dN} = C_0 N^{-\beta}\, (1+z)^{\gamma}. \quad (14)$$

As presented in Tables 3–4, the pLLS and LLS absorbers are allocated to bins in z and log N, with the survey sensitivity expressed through the effective redshift, $\Delta z_{\rm eff}$, covered by QSOs in our sample. Many studies (e.g., Janknecht et al. 2006; O'Meara et al. 2013), including our previous work (e.g., Danforth et al. 2016, and references therein), have employed variants of least-squares fitting of $f(N, z)$ to binned histograms in order to determine β and γ. This approach has several benefits, most notably its illustrative value in plots or tables and its computational simplicity in the presence of measurement errors and search path lengths that may vary as functions of N and z. In the limit of small bins of zero uncertainty, it tends toward the maximum-likelihood results. However, in the presence of finite binned data, this least-squares approach does not generally yield the maximum-likelihood estimates of the parameters for power-law distributions (Newman 2005; Clauset et al. 2009), and it introduces systematic biases in the fit parameters and their confidence intervals.[5] Because of the prevalence of binned fits in the literature, it is worth explaining in detail the maximum-likelihood approach to obtaining these parameters, as implemented in the present study.

From Equation (14), the likelihood function for a data set of $\mathcal{N}$ absorbers given the parameters β and γ is

$$\mathcal{L}(\boldsymbol{P}(N, z)|\beta, \gamma) = \prod_{i=1}^{\mathcal{N}} \left(\int_{\rm out} P_i(N, z) dN dz \right. \\ \left. + C_0 \int_{z_{\rm min}}^{z_{\rm max}} \int_{N_{\rm min}}^{N_{\rm max}} P_i(N, z) N^{-\beta}\, (1+z)^{\gamma} \times w(N, z) dN dz \right). \quad (15)$$

Here, $P_i(N, z)$ is the normalized probability density distribution for measurements of N and z for absorber i, and $w(N, z)$ is a weight function that accounts for the surveyed path length in z.

[5] Discussions of these effects are given in published papers (Goldstein et al. 2004; Newman 2005; Clauset et al. 2009) and subsequent online revisions, found in https://arxiv.org/abs/cond-mat/0412004 and http://arxiv.org/abs/0706.1062.

The first term in Equation (15) represents the total probability that absorber i is outside the range in z or N over which we wish to fit the free parameters.

The normalized distribution $_{Pi}(N, z)$ characterizes the data-derived uncertainties and correlations in the measurements, which will depend on factors such as data quality and line-fitting techniques, and it introduces the need to evaluate the double integral in Equation (15). In moderate-resolution spectra, such as the COS G130M and G160M data used in this study, the uncertainty in redshift determination is quite small, and we neglect it. We assume that $_{Pi}(N, z) \approx {_{Pi}}(N)\delta(z - z_i)$, where z_i is the measured redshift of the absorber, although this assumption is not valid for all data sets used in IGM studies. The column density measurements, on the other hand, can be subject to substantial and widely varying uncertainty that can potentially affect the derived parameters. Following Stevans et al. (2014), we assume that $P(N)$ is a log-normal distribution defined by the measured column density parameters from Table 2 in Stevans et al. (2014) with modifications listed in Table 6 of the present paper. The one exception is the absorber at $z = 0.47379$ in the SDSS J154553.48+093620.5 sight line, for which we have only upper and lower limits ($17.9 < \log N < 19.0$) and treat as a uniform distribution over that interval.

The function $w(N, z)$ gives the number of observed targets over which an absorber of column density N and redshift z could have been observed. Put another way, the integral of this function is the aforementioned effective path length over a given redshift and column density interval, $\Delta z_{\rm eff} = \int\int w(N, z)dNdz$. In general, such a function depends on properties of the observations, including but not limited to the observed wavelengths, the redshifts of the background AGNs, and the wavelength-dependent signal-to-noise ratios of the spectra. Often, this function must be evaluated numerically, but in some cases simplifying assumptions can be made. Because the present study is concerned only with relatively strong H I absorbers in well-resolved data with high signal-to-noise ratio, we assume that w is a function only of z and can be expressed as

$$w(N, z) \approx w(z) \approx \sum_{j=1}^{\mathcal{N}_{\rm AGN}} [H(z - z_{\rm min,j}) - H(z - z_{\rm max,j})], \tag{16}$$

where $H(x)$ is the Heaviside step function and $z_{\rm min,j}$ and $z_{\rm max,j}$ are the minimum and maximum redshifts at which an absorber could be detected in sight line j, respectively.

Note that if all of the measured column densities and redshifts had no measurement errors and the path length was independent of N and z, the likelihood function would remain a pure power law. If upper integration limits are further allowed to go to infinity, it becomes straightforward to derive analytical formulae for a maximum-likelihood power-law exponent and its uncertainty, as shown in Newman (2005), Clauset et al. (2009), and references therein. Several authors have used these formulae to calculate β and/or γ (e.g., Tytler 1987a, 1987b; Storrie-Lombardi et al. 1994; Stengler-Larrea et al. 1995 Songalia and Cowie 2010; Ribaudo et al. 2011a; Rudie et al. 2013). However, typical IGM surveys have a completeness function that varies strongly with N and z, as well as large uncertainties in N that span a wide range of magnitudes depending on z and their location on the CoG. Thus, these surveys may not sufficiently approximate the assumptions of such analytical formulae. In general, the approach of using these formulae introduces a systematic bias in the derived power-law exponents. Although the simplifications chosen for the present study maintain the separability of the likelihood function and thus the independence of the two fit parameters, this is not necessarily true for all possible forms of $w(N, z)$ and $P(N, z)$, which could introduce correlations between β and γ. In such a case, each term in Equation (15) must be explicitly evaluated as a two-dimensional integral at each step in the optimization process. These calculations are not computationally prohibitive, even if they must be performed numerically in the absence of an analytical solution.

The normalization C_0 is fixed by β and γ under the requirement that each observed absorber's existence has unity probability within the data set. It can be evaluated as

$$C_0 = \mathcal{N}'\left[\int_{z_{\rm min}}^{z_{\rm max}} \int_{N_{\rm min}}^{N_{\rm max}} N^{-\beta}\,(1 + z)^{\gamma}\, w(N, z)dNdz\right]^{-1}, \tag{17}$$

where the limits of integration are the search ranges of the survey, and the single power-law approximation remains valid. In our standard fits, we set $(N_{\rm min}, N_{\rm max}) = (10^{15}\,{\rm cm}^{-2}, 10^{20}\,{\rm cm}^{-2})$ and $(z_{\rm min}, z_{\rm max}) = (0.24, 0.84)$, as discussed in Section 3.1. In Equation (17), we introduced the variable $\mathcal{N}'$ (in contrast to the unprimed $\mathcal{N}$). This distinction is necessary to maintain definitional consistency of C_0 while accounting for the effects of the finite limits of integration in the second term of Equation (15), which may allow a fraction of $P(N, z)$ to fall outside the region of integration, into the first term of Equation (15). Therefore, $\mathcal{N}'$ is the noninteger number of (fractional) absorbers contributing to the likelihood function

$$\mathcal{N}' = \sum_{i=1}^{\mathcal{N}} \mathcal{N}'_i = \sum_{i=1}^{\mathcal{N}} \int_{z_{\rm min}}^{z_{\rm max}} \int_{N_{\rm min}}^{N_{\rm max}} P_i(N, z)dNdz, \tag{18}$$

where $\mathcal{N}'_i$ is the individual fractional contribution of an absorber i.

Using each of our assumptions with Equation (15) and taking the logarithm for computational convenience, we obtain the log-likelihood function that we use for optimization of β and γ in the present study:

$$\ln \mathcal{L}(\boldsymbol{P}(N), \boldsymbol{z}\;|\beta, \gamma) = \sum_{i=1}^{\mathcal{N}} \ln\Bigg(\int_{-\infty}^{N_{\rm min}} P_i(N)dN + \int_{N_{\rm max}}^{\infty} P_i(N)dN + C_0(1 + z_i)^{\gamma} w(z_i) \int_{N_{\rm min}}^{N_{\rm max}} P_i(N)N^{-\beta}dN\Bigg). \tag{19}$$

For our data set, the second term within the logarithm in Equation (19) is negligibly small and therefore not evaluated. Because this likelihood function contains multiple numerical integrals that must be evaluated for each absorber, it can be computationally expensive to evaluate for some choices of $P(N)$ and $(N_{\rm min}, N_{\rm max})$. For this reason, we optimize the likelihood function and determine β and γ by sampling the posterior probability distribution with version 2.1.0 of emcee (Foreman-Mackey et al. 2013), which implements the affine-invariant Markov chain Monte Carlo (MCMC) ensemble sampler from Goodman & Weare (2010). We adopt uniform priors over $-5 < \gamma < 10$ and $0 < \beta < 10$. We initialize 250 walkers randomly over the domain, allowing each to take 250 steps, the first 75 of which are discarded as a burn-in period.

This MCMC procedure yields median values of $\beta = 1.48 \pm 0.05$ and $\gamma = 1.14^{+0.88}_{-0.89}$, and $C_0 = 2.07 \times 10^7$ (for N in cm^{-2}). The error bars indicate the 1σ quantiles around the median in the highly Gaussian, marginalized posterior probability distributions. Figures 12 and 13 show the fits and differential distributions.

ORCID iDs

J. Michael Shull https://orcid.org/0000-0002-4594-9936
Charles W. Danforth https://orcid.org/0000-0003-4738-6601

References

Bahcall, J. N., Bergeron, J., Boksenberg, A., et al. 1993, ApJS, 87, 1
Battisti, A. J., Meiring, J. D., Tripp, T. M., et al. 2012, ApJ, 744, 93
Blanton, M. R., Hogg, D. W., Bahcall, N. A., et al. 2003, ApJ, 592, 819
Bordoloi, R., Tumlinson, J., Werk, J. K., et al. 2014, ApJ, 796, 136
Clauset, A., Shalizi, C. R., & Newman, M. E. J. 2009, SIAMR, 51, 661
Cooksey, K. L., Prochaska, J. X., Chen, H.-W., et al. 2008, ApJ, 676, 262
Crighton, N. H. M., Morris, S. L., Bechtold, J., et al. 2010, MNRAS, 402, 1273
Danforth, C. W., Keeney, B. A., Tilton, E. M., et al. 2016, ApJ, 817, 111
Danforth, C. W., & Shull, J. M. 2008, ApJ, 679, 194
Fardal, M. A., Giroux, M. L., & Shull, J. M. 1998, AJ, 115, 2206
Foreman-Mackey, D., Hogg, D. W., Lang, D., & Goodman, J. 2013, PASP, 125, 306
Fox, A. J., Lehner, N., Tumlinson, J., et al. 2013, ApJ, 778, 187
Gehrels, N. 1986, ApJ, 303, 336
Goldstein, M. L., Morris, S. A., & Yen, G. G. 2004, EPJB, 41, 255
Goodman, J., & Weare, J. 2010, Commun Appl Math Comput Sci., 5, 65
Green, J. C., Froning, C. S., Osterman, S., et al. 2012, ApJ, 744, 60
Haardt, F., & Madau, P. 2012, ApJ, 746, 125
Hussain, T., Muzahid, S., Narayanan, A., et al. 2015, MNRAS, 446, 2444
Janknecht, E., Reimers, D., Lopez, S., & Tytler, D. 2006, A&A, 458, 427
Jenkins, E. B., Bowen, D. V., Tripp, T. M., & Sembach, K. R. 2005, ApJ, 623, 767
Keeney, B. A., Stocke, J. T., Rosenberg, J. L., Tumlinson, J., & York, D. G. 2006, AJ, 132, 2496
Kim, T.-S., Carswell, R. F., Cristiani, S., D'Odorico, S., & Giallongo, E. 2002, MNRAS, 335, 555
Lehner, N., Howk, J. C., Tripp, T. M., et al. 2013, ApJ, 770, 138
Lehner, N., Prochaska, J. X., Kobulnicky, H. A., et al. 2009, ApJ, 694, 734
Markwardt, C. B. 2009, in ASP Conf. Ser. 411, Astronomical Data Analysis Software and Systems XVIII, ed. D. A. Bohlender, D. Durand, & P. Dowler (San Francisco, CA: ASP), 251
Meiring, J. D., Tripp, T. M., Prochaska, J. X., et al. 2011, ApJ, 732, 35
Meiring, J. D., Tripp, T. M., Werk, J. K., et al. 2013, ApJ, 767, 49
Miralda-Escudé, J. 2003, ApJ, 596, 66
Morrissey, P., Schiminovich, D., Barlow, T., et al. 2005, ApJL, 619, L7
Morton, D. C. 2003, ApJS, 149, 205
Muzahid, S., Srianand, R., & Charlton, J. 2015, MNRAS, 448, 2840
Narayanan, A., Savage, B. D., Wakker, B. P., et al. 2011, ApJ, 730, 15
Neeleman, M., Prochaska, J. X., Ribaudo, J., et al. 2016, ApJ, 818, 113
Newman, M. E. C. 2005, ConPh, 46, 323
O'Meara, J. M., Prochaska, J. X., Worseck, G., Chen, H.-W., & Madau, P. 2013, ApJ, 765, 137
Paresce, F., McKee, C. F., & Bowyer, S. 1984, ApJ, 240, 387
Penton, S. V., Stocke, J. T., & Shull, J. M. 2004, ApJS, 152, 29
Prochaska, J. X., Werk, J. K., Worseck, G., et al. 2017, ApJ, 837, 169
Rao, S. M., Turnshek, D. A., & Nestor, D. B. 2006, ApJ, 636, 610
Rao, S. M., Turnshek, D. A., Sardane, G. M., & Monier, E. M. 2017, MNRAS, 471, 3428
Ribaudo, J., Lehner, N., & Howk, J. C. 2011a, ApJ, 736, 42
Ribaudo, J., Lehner, N., Howk, J. C., et al. 2011b, ApJ, 743, 207
Rudie, G. C., Steidel, C. C., Shapley, A. E., & Pettini, M. 2013, ApJ, 769, 146
Sargent, W. L. W., Steidel, C. C., & Boksenberg, A. 1989, ApJS, 69, 703
Savage, B. D., Lehner, N., Narayanan, A., et al. 2011, ApJ, 743, 180
Shull, J. M. 2014, ApJ, 784, 142
Shull, J. M., Giroux, M. L., Penton, S. V., et al. 2000, ApJL, 538, L13
Shull, J. M., Jones, J. R., Danforth, C. W., & Collins, J. A. 2009, ApJ, 699, 754
Shull, J. M., Roberts, D., Giroux, M. L., et al. 1999, AJ, 118, 1450
Shull, J. M., Smith, B. D., & Danforth, C. W. 2012a, ApJ, 759, 23
Shull, J. M., Stevans, M. L., & Danforth, C. W. 2012b, ApJ, 752, 162
Simcoe, R. A., Sargent, W. L. W., Rauch, M., & Becker, G. 2006, ApJ, 637, 648
Steidel, C. C. 1990, ApJS, 74, 37
Stengler-Larrea, E. A., Boksenberg, A., Steidel, C. C., et al. 1995, ApJ, 444, 64
Stevans, M. L., Shull, J. M., Danforth, C. W., & Tilton, E. M. 2014, ApJ, 794, 75
Stocke, J. T., Keeney, B. A., Danforth, C. W., et al. 2013, ApJ, 763, 148
Stocke, J. T., Keeney, B. A., Danforth, C. W., et al. 2014, ApJ, 791, 128
Storrie-Lombardi, L. J., McMahon, R. G., Irwin, M. J., & Hazard, C. 1994, ApJL, 427, L13
Tejos, N., Morris, S. L., Finn, C. W., et al. 2014, MNRAS, 437, 2017
Telfer, R., Zheng, W., Kriss, G. A., & Davidsen, A. F. 2002, ApJ, 656 773
Tilton, E. M., Stevans, M. L., Shull, J. M., & Danforth, C. W. 2016, ApJ, 817, 56
Tripp, T., Bechtold, J., & Green, R. F. 1994, ApJ, 433, 533
Tripp, T., Meiring, J. D., Prochaska, J. X., et al. 2011, Sci, 334, 952
Tumlinson, J., Thom, C., Werk, J. K., et al. 2011a, Sci, 334, 948
Tumlinson, J., Thom, C., Werk, J. K., et al. 2013, ApJ, 777, 59
Tumlinson, J., Werk, J. K., Thom, C., et al. 2011b, ApJ, 733, 111
Turnshek, D. A., Monier, E. M., Rao, S. M., et al. 2015, MNRAS, 449, 1536
Tytler, D. 1987a, ApJ, 321, 49
Tytler, D. 1987b, ApJ, 321, 69
Weymann, R. J., Jannuzi, B. T., Lu, L., et al. 1998, ApJ, 506, 1
Wolfe, A. M., Gawiser, E., & Prochaska, J. X. 2005, ARA&A, 43, 861